Master of Science degree in Mechanical Engineering

Department of Mechanical and Aerospace Engineering

Master thesis

PRELIMINARY DESIGN OF THE ELECTRONICALLY CONTROLLED INTELLIGENT SCALABLE SUSPENSION

Advisor:
Prof. Eugenio BRUSA
Host university supervisor
FH-Prof. DI Dr. Christian Kollmitzer
University of Applied Sciences
Technikum Wien

Candidate:
Bakhtiyor Ismailov

October 2018

Disclaimer

The research has a conceptual and innovative character. This thesis represents the opinions of the author, and it is the product of professional research. The findings in this document are not to be construed as final results, since it is the preliminary design of the electronically controlled intelligent scalable suspension, and most of the results were based on the finite elements method calculation. The backgrounds used in this thesis have only an informative and cognitive purpose, and the source of information can be found in the reference list.

Summary

This thesis is about a new alternative design of the electronically controlled intelligent scalable suspension for passenger cars. The thesis is divided into three main parts.

In the first part, the main sources of excitation were investigated and the probabilistic analysis was applied to obtain a random road profile based on the road roughness classification of the ISO 8608.

The second part refers to rheological fluid dampers, where electro-rheological shock absorber was studied and simulated by the finite element method. After numerical simulation of ER fluids, results were implemented for a new ER shock absorber design.

The final part of the thesis is devoted to energy regenerative systems and relevant electric circuits. In order to design the power circuit, the model of the mechanical system with a semi-active damper was created by SIMULINK, and after the simulation, a test bench was used, controlled by the Matlab code. Afterward, the output voltage was studied to design the electric circuit.

The first result is a random road profile based on ISO 8608, which was created by the special codes. It is required for the dynamic analysis of the mechanical system. Consequently, various mechanical systems were modelled in order to obtain output results with characteristics required to design regenerative suspension system.

The second result is related to ER fluid damper, where the properties of the ER material were investigated, later the results were used to design a new type of electrorheological shock absorber.

Finally, the results based on the last part are electrical circuits that can be used for the power regenerative systems. The major elements of the circuits are capacitors and MOSFETs. Simulation of the electric circuit showed that the voltage of the buffer capacitor has an influence on the electric motor, by controlling the voltage of the corresponding capacitor, it is possible to achieve both mechanical manipulation and power generation.

The research based on the topic allows to understand how new materials can improve conventional mechanisms, and the tendency of the scientific researches shows that in the future it will be possible to create composite materials with a special nano-structure that can be used as a suspension spring and a shock absorber in one structure.

"Hier bin ich mensch hier darf ich's sein"

Johann Wolfgang von Goethe

Abstract –

The current automotive market has basically two trends: the first digitalization of the car system or autonomous technology, the second meet the requirements of the fuel economy regulations with environmental requirements.

The autonomous technology will help to drivers and passengers to use their time during vehicle mobility for personal activities, and by using intelligent suspension system, we can spend our transit time for leisure activities.

Meanwhile, consumers today prefer more multifunctional and "all-purpose" vehicles, no matter if commuting to work or taking the family to the nature. In this case, they want more options in order to choose the best solution for a specific purpose, and the active and semi-active suspension systems play one of the main role to solve this issue for any kind of road by keeping reliability and comfort.

The most automakers should meet stricter fuel economy standards through a combination of improved aerodynamics, better performance using turbo engines, and lighter manufacturing materials, among other tactics. The traditional vehicle suspension dissipates the mechanical energy into heat, which wastes energy. The regenerative suspensions have attracted much attention in recent years for the improvement of vibration performance as well as the reduction of energy loss. The regenerative suspension system can improve energy performance of the car.

List of Figures

Fig. 3.1. Road Surface Classification (ISO 8608). 9
Fig. 3.2. Road Surface Classification. 14
Fig. 3.3. Random Road Simulink Model. 15
Fig. 3.4. Random Road Simulation. 17
Fig. 3.5. PSD of the random road. 17
Fig. 4.1. Two-degrees of freedom (a) and single-degree of freedom (b) models for oil damper mounted in parallel with compression helical spring. 18
Fig. 4.2. Two-degrees of freedom (a) and one-degree of freedom (b) models for colloidal damper without compression helical spring mounted in parallel. 19
Fig. 4.3. Two-degrees of freedom (a) and one-degree of freedom (b) models for colloidal damper mounted in parallel with compression helical spring. 19
Figure 4.4 Illustrates a McPherson strut mechanism and its equivalent vibrating system 21
Fig. 4.5 Typical single degree of freedom system subject to base excitation 22
Fig 4.6. The effects of changing the excitation frequency. 25
Fig 4.7. The effects of changing the excitation amplitude 26
Fig 4.8. The effects of changing the damping ratio. 27
Fig 4.9. Response for the delayed-impulse input 28
Fig 4.10. Non generic input function 29
Fig 4.11. The quarter car system hits the bump 30
Fig 4.12. The function of the bump in MATLAB 32
Fig 4.13. The response of the sprung mass. 32
Fig.4.14. Quarter-car model 32
Fig. 4.15. Simulink model of the suspension system passive mode. 34
Fig. 5.1. Tubular permanent magnet actuator in parallel with a passive spring 36
Fig. 5.2 Intelligent (smart) materials 37
Fig 5.3 The relationship of Newtonian and non-Newtonian fluids between shear stress and shear rate 38
Fig. 7.1 Electro polarization 40
Fig. 7.2 Stress-shear strain rate relationship of two different types 41
Fig. 7.4 Three basic flow modes 42
Fig. 7.5 The flow in y-z direction 43
Fig. 8.1 - Dimension of the geometric modeling 45
Fig. 8.2 - Illustration of FEM boundary conditions 46
Fig.8.3 - Three different regions of the Bingham material 47
Fig. 8.4 - The boundary conditions of simple shear mode 48
Fig. 8.5 - External velocity profile 48
Fig. 8.6 - Boundary conditions in the pressure mode 48
Fig 8.7 - y-displacement profile at 8mm/s: 49
Fig 8.8 - z-displacement profile at 8mm/s, z-displacement is over the tolerance of ADINA. 49
Fig 8.9 - The pressure difference is uniform throughout the region 49
Fig 8.10 - Shear stress gradient 50
Fig 8.11 - Shear stress gradient for long distance 50
Fig 8.12 - YY stress gradient 51
Fig. 8.13 Stress distribution and reaction forces. 51
Fig 8.14- y-velocity profile from zero to 8 seconds with the increasing velocity up to 8mm/s. 51
Fig 8.15- Pressure distribution with the increasing velocity 52
Fig 8.16 - y-velocity profile 52
Fig 8.17 - Shear stress 53
Fig. 8.18 The shear stress distribution 53
Fig 8.19 - The pressure and YY-stress of the solid region of Bingham plastic fluid 54
Fig 8.19. 3D simulation of pressure mode. 54
Fig 8.21. Multi-duct 55
Fig 8.22 Yield stress versus electric field of some ER fluids. Dots: TiO_2 nano-particles with $(NH_2)_2CO$ contained; Circles: Ca-Ti-O nano-particles with C=O, O-H groups contained; Triangles: TiO_2 nano-particles with C=O, O-H groups contained. 56
Fig 8.22. – Electro rheological shock absorber with multiple ducts 57

Fig 8.23. The electrodes with 0.5mm distance between electrodes 57
Fig 8.24. Suspension system with section cut 58
Fig 8.25. The bottom part of the shock absorber 58
Fig. 9.1 - 2DOF Quarter-Car Model. 59
Fig. 9.2 - The skyhook damper model 60
Fig. 9.3 - Ground hook Formulation for the 2DOF System. 61
Fig. 9.4. Hybrid Control. 62
Fig. 9.5 SIMULINK Code for the Hybrid Controller. 63
Fig. 9.6 - SIMULINK Code for the quarter car model with hybrid controller. 63
Fig. 9.7 The suspension system under control of hybrid controller. 64
Fig. 9.8. The suspension system with and without the controller 64
Fig. 9.9 The response of the suspended mass to the random road excitation 64
Fig. 9.10 - Velocities of suspended, non-suspended masses and control force. 65
Fig 9.11 - Suspension travel 65
Fig. 10.1 - Electromechanical rotary shock absorber 66
Fig.10.3 - Actuator for combat vehicle suspension ECASS 67
Fig.10.4 – Gearbox 67
Fig.10.5 - PM electric motor 68
Fig. 10.6: (a) Field strength as a function of distance x through the center of the pole pieces. b) Magnetic flux through a square plate as a function of the position of the plate x. 69
Fig.10.7 – Geometric parameters of the PM electric motor 71
Fig.10.8 – PM electric motor capabilities by speed and torque 72
Fig. 11.1. DC electric motors (left generator, right motor) 73
Fig. 11.2. Output signal from the sound card. 74
Fig. 11.3. Output voltage from the generator. 76
Fig. 11.4. Output voltage from the generator collected in the Matlab code. 77
Fig. 12.1 Simulation of the electric circuit 78
Fig. 12.2 Electric circuit with voltage gain. 79
Fig. 12.3. Output voltage from the generator collected in the Matlab code. 79
Fig. 12.4 Circuit with controller 80
Fig. 12.5 Circuit with two capacitors 80
Fig. 12.6 Voltage of two capacitors 81
Fig. 12.7-Advanced circuit with two capacitors 81
Fig. 13.1. Stress analysis of the torsion bar. 84
Fig. 13.2. Stress distribution in PIN-PMN-PT ferroelectric ceramics. 85
Fig. 13.3. Stress analysis of the ferroelectric ceramic PIN-PMN-PT. 86
Fig. 13.4. Voltage analysis of the ferroelectric ceramic. 86
Fig. 13.5. Voltage distribution along the y-axis is linear. 86
Fig. 13.6. The electric field of the ferroelectric ceramic along the y-axis. 87

List of Tables

Table 2.1 Comfort reactions to vibration environment 6
Table 3.1. ISO Road Roughness Classification 8
Table 3.2. ISO Road Roughness Classification 9
Table 4.1. The suspension system parameters 33
Table 5.1 Comparisons between various vehicle suspensions 35
Table 7.1 ER fluid types 41
Table 8.1 Characteristics of two types of ER fluids 45
Table 8.2 Property parameters of ERM under different electric field intensities 47
Table 8.3. Electro-mechanical parameters of the ER fluid. 55
Table 10.1 - Technical data of the gearbox 68
Table 10.2 - Technical data of the electric motor 71
Table. 13.1. Physical properties of the ferroelectric materials. 85

Contents

List of Figures 1
List of Tables 3
1. Introduction 5
2. Vibration evaluation 6
   2.1. Evaluation of human exposure to vibration 7
3. Random road profile 8
   3.1. ISO Road Roughness Classification 8
   3.2. Probabilistic analysis 10
   3.3. Random road profile simulation 12
4. Passive Mechanical System 18
   4.1. Background of the dynamic models of the conventional vehicle suspensions 18
   4.2. Quarter car system with single degree of freedom 22
   4.3. Quarter car system with non-harmonic excitations 28
   4.4. Quarter car system simulation with convolutional integral 30
   4.5. A quarter-car model with double degree of freedom 32
5. Active And Semi-active Mechanical System 35
   5.1. Configuration of active suspension system 35
   5.2. Active suspension system with electromagnetic linear actuators 36
   5.3. Semi-active suspension system 36
   5.4. Bingham plastic fluid and Newtonian fluid 38
6. Magneto rheological fluids 39
7. Electro rheological fluids 40
   7.1. Three basic motions of ER fluid applications 42
8. FEM simulations 45
   8.1. FEM modeling 45
   8.2. Simulation of the Bingham plastic fluid 46
   8.3. Simple or direct shear mode 48
   8.4. Simple shear mode with increasing velocity 51
   8.5. Pressure mode between two plates 52
   8.6. Implementation of the results in a new design 54
9. Semi-active control methods 59
10. Electro-mechanical system 66
   10.1. GEARBOX 66
   10.2. Electric motor 68
11. A test bench and the output voltage of the PM electric motor 72
12. Electric circuit 78
13. Alternative energy harvesting system 82
14. Conclusion 88
References 89

1. Introduction

Conventional dampers dissipate road excitation energy into thermal energy in order to keep stabilization. Meanwhile, the regenerative suspension will transform the kinetic energy into electricity that can be stored and later can be used to control the damping force of the damper to improve the suspension performance.
Conventional vehicles use only 10-20% the fuel energy for vehicle mobility. The dissipated energy by suspension dampers is related with vehicle speed, road roughness, suspension stiff and damping coefficient. The energy dissipation of vehicle suspension can't be ignored.
However, how much energy we are able to harvest from vehicle suspension? The energy from the regeneration process is enough to meet the energy requirement in consumption process for electromagnetic active suspension, which means the suspension is self-powered. Some scientists [1] estimated the average regenerative power of each suspension on the highway at 16 m/s reached 100W accounting for about 5% of driving power. Theoretical results show a maximum of 10% fuel efficiency can be recovered from regenerative shock absorbers.

Major sources of excitations in motor vehicles are the engine, transmission system, air-conditioning system, road and aerodynamic excitations. Thus, major excitation sources and their frequency ranges are:

1. Rigid body vibrations of pitching and rolling on suspension system and wheels (0.5–2 Hz).
2. Vibrations due to the engine (11–17 Hz),
3. Bending and torsional vibration of the body as a whole (25–40 Hz),

Although resonances connected to suspension systems and wheels are in the domain of 0.5–2 Hz, structural resonances of various systems in motor vehicles are going up to 100 Hz. Road excitation frequency increases with the vehicle speed and decreases with the wavelength of the road roughness. In order to assess vibration we should know not only response of the mechanical system but also behavior of the source of excitation forces [2].

2. Vibration evaluation

The vibration assessment method in accordance with ISO 2631 should always include measurements of the acceleration in the form of the weighted root-mean-square (R.M.S.).

The weighted R.M.S. acceleration is expressed in meters per second squared (m/s^2) for translation vibration and in radians per second squared (rad/s^2) for rotational vibration. The weighted R.M.S. acceleration is calculated according to the following equation or its equivalents in the frequency domain

$$a_w = \left[\frac{1}{T}\int_0^T a_w^2(t)dt\right]^{\frac{1}{2}} \qquad (2.1)$$

Where

$a_w(r)$ is the weighted acceleration (translational or rotational) as a function of time (time history), in meters per second squared (m/s^2) or radians per second squared (rad/s^2), respectively;

T is the duration of the measurement, in seconds.

The permissible vibration values for comfort depend on many factors, which vary depending on each application. The following values give approximate signs of probable reactions to different values of the total common values of vibration in public transport.

Less than 0,315 m/s^2:	not uncomfortable
0,315 m/s^2 to 0,63 m/s^2:	a little uncomfortable
0,5 m/s^2 to 1 m/s^2:	fairly uncomfortable
0,8 m/s^2 to 1,6 m/s^2:	uncomfortable
1,25 rn/s^2 to 2,5m/s^2:	very uncomfortable
Greater than 2 m/s^2:	extremely uncomfortable

Table 2.1 Comfort reactions to vibration environment

However, as mentioned earlier, reactions of different sizes depend on the expectations of passengers regarding the duration of the trip and the type of activities that passengers expect (for example, reading, eating, writing, etc.). Moreover, many other factors (acoustic noise, temperature, etc.) [3].

2.1. Evaluation of human exposure to vibration.

Biodynamic research as well as epidemiological studies have given evidence for an elevated risk of health impairment due to long-term exposure with high-intensity whole-body vibration. Mainly the lumbar spine and the connected nervous system may be affected. Metabolic and other factors originating from within may have an additional effect on the degeneration. It is sometimes assumed that environmental factors such as body posture, low temperature, and draught can contribute to muscle pain [3].

The strength of the impact of vibration on the body ***depends on the amount of absorbed energy****,* the most adequate expression of which is the vibration velocity. The derivative of the vibration velocity in time is vibroacceleration (m/s^2). Vibration with a frequency of 8-16 Hz refers to low frequency, 31.5 and 63 Hz - to medium frequency, 125 to 1000 Hz - to high frequency. The greatest danger of the development of vibration sickness in vibration with a frequency of 16-200 Hz. Increased duration (within the working day or daily over years) and increased vibration intensity mean increased vibration dose and it can cause vibration disease.The disease manifests itself as a violation of the nervous, cardiovascular systems and the musculoskeletal system. Local and general vibration disturbs the mechanisms of neuro-reflex and neurohumoral systems. Vibration is a strong stimulus which affects the receptor apparatus of the skin, nerves, nerve trunks, leading to an increase in the secretion of noradrenaline in the synaptic nerve terminals. Since noradrenaline cannot completely capture them and accumulate in them as under normal conditions, a significant part of it enters the bloodstream and causes an increase in the tone of the vessels, which leads to increased blood pressure and angiospasm.

In persons affected by vibration, destructive phenomena occur in the Vatera-Pacini bodies, nerve fibers, spinal cord neurons, reticular stem formation, ganglion of intervertebral and vertebral columns. In objective research, there is a decrease in afferent innervation, in particular, perception of vibration sensitivity, and in the future, the emergence of other symptoms of prolapse and pain syndrome.

With the development of pathological changes in the autonomic apparatus, dystrophic changes occur in the skin, muscles, and the bone system. Especially often receptors of large joints of the shoulder girdle are affected, which causes their soreness.

Angiopoleyneuropathic syndrome (disturbance of vibration sensitivity, paresthesia) is combined with the development of the neurasthenic syndrome - hypersthenic form. Asthenia proceeds with a sharp weakening of inhibitory processes. The main complaints are headaches, dizziness, hypersensitivity, irritability, aching pain in the legs, numbness, paresthesia. In later periods are constant, vegetative crises (a feeling of faintness, tachycardia, lack of air, fear of death, thermoregulation disorders) join in. Accompanied by a weakening of memory, crying, sleep disturbance. Often there are attacks with pale toes of the feet, diffuse perspiration. First, disinhibition, and then suppression of tendon reflexes, trophic disorders (thinning of the skin on the toes, hypotonia of the muscles), moderate increase in blood pressure, its asymmetry develops. Electroencephalography centers of epileptiform activity are detected.

3. Random road profile

3.1. ISO Road Roughness Classification

The real suspension system of the vehicle also has uncertainties. Uncertainties include the uncertainty of the parameters and the uncertainty of the model. The mass of vehicle body is not constant because of passengers or load on the vehicle. The road disturbance may be determined randomly.

The road profile can be represented by the PSD function. The spectral power density of roads shows a characteristic decrease of the magnitude with the wavenumber. In order to determine the spectral power density function or PSD, it is necessary to measure the surface profile with respect to the reference plane. Random road profiles can be represented by a PSD in the form of

$$\Phi(\Omega) = \Phi(\Omega_0)\left(\frac{\Omega}{\Omega_0}\right)^{-\omega} \quad or\ \Phi(\mathrm{n}) = \Phi(\mathrm{n}_0)\left(\frac{\mathrm{n}}{\mathrm{n}_0}\right)^{-\omega} \qquad (3.1)$$

$\Omega = \frac{2\pi}{L}$ In rad/m denotes the angular spatial frequency, L is the wavelength, $\Phi(\Omega_0)$ in m2/ (rad/m) describes the values of the psd at the reference wave number $\Omega_0 = 1\mathrm{rad/m}$, $\mathrm{n} = \frac{\Omega}{2\pi}$ is the spatial frequency, n0 = 0.1cycle/m, ω is the waviness, for most of the road surface, $\omega = 2$ [4].

For a rough and quick estimation of the roughness quality, the following guidance is given:

1) New roadway layers, such as, for example, asphalt or concrete layers, can be assumed to have a good or even a very good roughness quality;
2) Old roadway layers which are not maintained may be classified as having a medium roughness;
3) Roadway layers consisting of cobblestones or similar material may be classified as medium (“average”) or bad (“poor”, “very poor”).

	Degree of roughness $\Phi(\mathrm{n0})(\mathrm{e}-6[\frac{\mathrm{m2}}{\frac{\mathrm{cycle}}{\mathrm{m}}}])$, where n0 = 0.1cycle/m		
Road class	Lower limit	Geometric mean	Upper limit
A (very good)	-	16	32
B (good)	32	64	128
C (average)	128	256	512
D (poor)	512	1024	2048
E (very poor)	2048	4096	8192

Table 3.1. ISO Road Roughness Classification

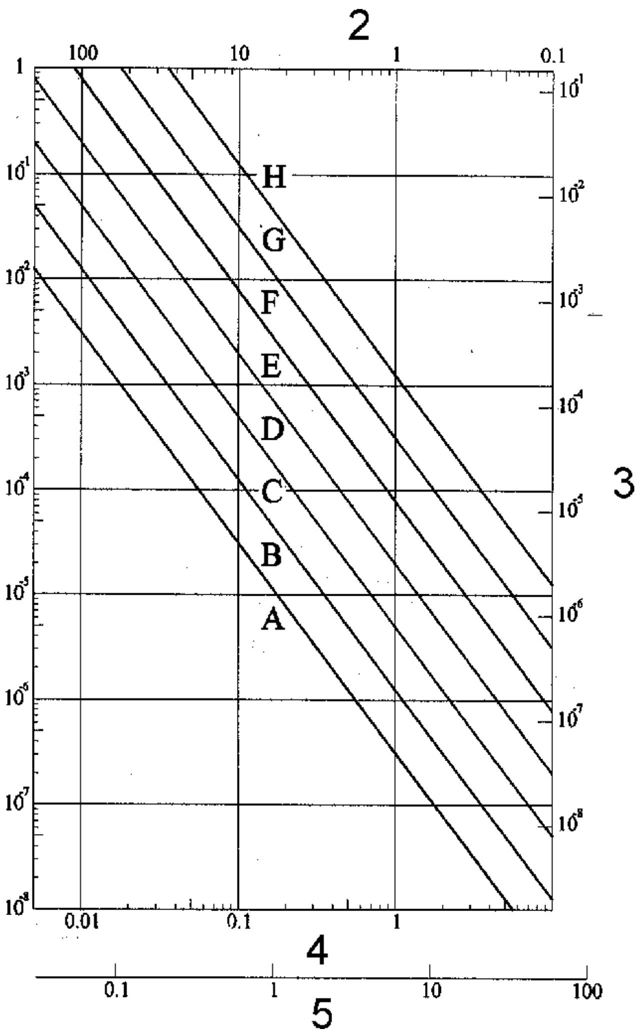

Fig. 3.1. Road Surface Classification (ISO 8608).

The axes surrounding the frame are defined as 1: displacement PSD, $\Phi(n)$ [m3], 2: wavelength, λ [m], and 3: displacement psd, $\Phi(\Omega)$[m3], 4: spatial frequency, n [cycle/m], 5: angular spatial frequency, Ω [rad/m]

	degree of roughness $\Phi(\Omega_0)(e-6[m3])$ where $\Omega_0 = 1 rad/m$		
Road class	Lower limit	Geometric mean	Upper limit
A (very good)	-	1	2
B (good)	2	4	8
C (average)	8	16	32
D (poor)	32	64	128
E (very poor)	128	256	512

Table 3.2. ISO Road Roughness Classification

3.2. Probabilistic analysis

If x is a normal random variable, then the probability distribution of x is defined as follows. The normal distribution is

$$f(x) = \frac{1}{\sigma\sqrt{2\pi}} e^{-\frac{1}{2}\left(\frac{x-\mu}{\sigma}\right)^2} \quad (-\infty < x < +\infty) \quad (3.2)$$

The mean of the normal distribution is $\mu(-\infty < \mu < +\infty)$ and the variance is $(\sigma)^2 > 0$. The mean and the variance of X are

$$\mathrm{E(X)} = \int_{-\infty}^{+\infty} x f(x) dx = \mu \quad (3.3)$$

$$D^2(X) = \sigma^2 \int_{-\infty}^{+\infty} x^2 f(x) dx = \sigma^2 \quad (3.4)$$

A correlation function is a function that gives the statistical correlation between random variables, contingent on the spatial or temporal distance between those variables [5]. A correlation function R(τ) of random process is a shifted second order moment:

$$\mathrm{R}(\tau) = E[H(t)H(t+\tau)] \qquad (3.5)$$

When $\tau = 0$ the function is positive and equals dispersion or the standard deviation of the variable:

$$\mathrm{R}(0) = E[H(t)]^2 = D[H(t)] > 0 \quad (3.6)$$

For comparative analysis, it is more convenient to use dimensionless quantities, as is customary in almost all technical device As such a dimensionless parameter in the correlation theory, we use the normalized correlation function $\rho(\tau)$, which in the probability theory[6] is called the coefficient of correlations:

$$\rho(\tau) = \frac{\mathrm{R}(\tau)}{\mathrm{R}(0)} = \frac{E[H(t)H(t+\tau)]}{E[H(t)]^2} \qquad (3.7)$$

$$\mathrm{R}(\tau) = \mathrm{R}(0)\,\rho(\tau) \qquad (3.8)$$

Approximation of the correlation function of the road. The correlation function of the random process can be assumed as a nonrandom function, and it can be approximated:

$$\rho(\tau) = e^{-\alpha|\tau|} cos\beta\tau \qquad (3.9)$$

α *and* β – parameters of correlation function for every part of the road, which has a difference from other parts.

Consider that T is the sample time and $x_A(t)$ is random excitation due to the roughness of the road,

$$\overline{x_A} = \frac{1}{T}\int_0^T x_A(t)dt \qquad (3.10)$$

$$x_{A\,rms} = \frac{1}{T}\int_0^T x_A^2(t)dt \qquad (3.11)$$

The standard deviation (variance):

$$\sigma = \frac{1}{T}\int_0^T [x_A(t) - \overline{x_A}]^2 dt \qquad (3.12)$$

The self-correlation function:

$$R(\tau) = \lim_{T\to\infty}\frac{1}{T}\int_0^T x_A(t).x_A(t+\tau)dt \qquad (3.13)$$

The power spectral density SPD:

$$S_{xA}(\omega) = \int_{-\infty}^{\infty} R(\tau)e^{-i\omega\tau}d\tau \qquad (3.14)$$

and conversely

$$R(\tau) = \frac{1}{2\pi}\int_{-\infty}^{\infty} S_{xA}(\omega)e^{i\omega\tau}d\,\omega \qquad (3.15)$$

If X(t) is real, then the auto-correlation function $R(\tau)$is real and even, that is, $R(\tau) = R(-\tau)$, it follows that

$$S_{xA}(\Omega) = 2\int_0^{\infty} R(\tau)\cos(\Omega\tau)d\tau \qquad (3.16),$$

And

$$R(\tau) = \frac{1}{2\pi}\int_{-\infty}^{\infty} S_{xA}(\omega)\cos(\omega\tau)\,d\,\omega \qquad (3.17)$$

to avoid negative wave number, usually a one-sided PSD is defined with

$$\Psi(\omega) = \begin{cases} 2S(\omega), & for\ \omega \geq 0 \\ 0, & for\ \omega < 0 \end{cases} \quad (3.18)$$

Therefore, we obtain

$$R(\tau) = \frac{1}{\pi}\int_{-\infty}^{\infty} \Psi(\omega)\cos(\omega\tau)\, d\,\omega \quad (3.19)$$

If we use correlation function of the random road

$$R(\tau) = R(0)\, e^{-\alpha|\tau|} cos\beta\tau \qquad (3.20)$$

$$\Psi(\omega) = 2\int_{0}^{\infty} R(\tau)\cos(\omega\tau) d\tau \qquad (3.21)$$

After using $R(\tau)$ in our equation we will get:

$$\Psi(\omega) = R(0)\frac{2\alpha(\alpha^2+\beta^2+\omega^2)}{\omega^4+2(\alpha^2-\beta^2)\omega^2+(\alpha^2+\beta^2)^2} \qquad (3.22)$$

where $\alpha = \alpha 1 * V$ and $\beta = \beta 1 * V$ [6].

3.3. Random road profile simulation.

When a vehicle is moving along the road with velocity V, the excitation frequency of the road input ω (rad/sec) becomes $\omega = \Omega V$. The mean squared value of road surface roughness, that is the total area of the power spectral density function, does not change with the velocity of a vehicle. Let $\Psi(\omega)$ represents the power spectral density of road input with respect to displacement excitation frequency. Therefore we have the following relation:

$$\Psi(\omega) d\omega = \Phi(\Omega) d\Omega \qquad (3.23)$$

And $\Phi(\Omega)$ is given by ISO :

$$\Phi(\Omega) = \Phi(\Omega_0)\left(\frac{\Omega}{\Omega_0}\right)^{-\omega} \ or\ \Phi(n) = \Phi(n_0)\left(\frac{n}{n_0}\right)^{-\omega} \qquad (3.24)$$

Which in turn yields the relationship between $\Psi(\omega)$ and $\Phi(\Omega)$

$$\Psi(\omega) = \frac{\Phi(\Omega)}{V} = \Phi(\Omega_0)\frac{\left(\frac{\Omega}{\Omega_0}\right)^{-\omega}}{V} = \frac{\Phi(\Omega_0)(\Omega_0)^2 V}{(\omega)^2} \quad (3.25)$$

$$\Psi(\omega) = R(0)\frac{2\alpha(\alpha^2+\beta^2+\omega^2)}{\omega^4+2(\alpha^2-\beta^2)\omega^2+(\alpha^2+\beta^2)^2} = \frac{\Phi(\Omega_0)(\Omega_0)^2 V}{(\omega)^2} \quad (3.26)$$

In order to prove this relation I used Matlab,

```
close all
clear all
v=10; % vehicle speed [km/h]
vms=v/3.6; %divided  by 3.6 to get [m/s]
class=2*[ 16 64 256 1024 4069]*1e-6;% road classification
V=vms;
ca=0.012; %
cb=0;%
a=ca*V;%
b=cb*V;%
k=2;%
for i=1:5
%% frequency range
step=10000;% stepsize
fr=logspace(-1,2,step); % frequency range  [Hz]
%% ISO 8606
n0=0.1; %cycle/m
n=fr/V; %n=om/2pi om=w/V w=f*2pi => om=f*2pi/V =>n=f/V
Pxx=class(i)*(n/n0).^-k; %
%% From calculations
w=fr;
Ro=class(i);
PSD=0.405*Ro*2*a*(a^2+b^2+w.^2)./(w.^4+2*(a^2-
b^2).*w.^2+(a^2+b^2)^2); % m^2s/cycle
PSx=PSD*V;
% ploting the results
figure(1)
loglog(n,PSx,'--');
hold on;
loglog(n,Pxx);
xlabel('frequency [cycle/m]');
ylabel('magnitude [m^3/cycle]');
title('PSD comparison ISO 8606');
grid on
end
```

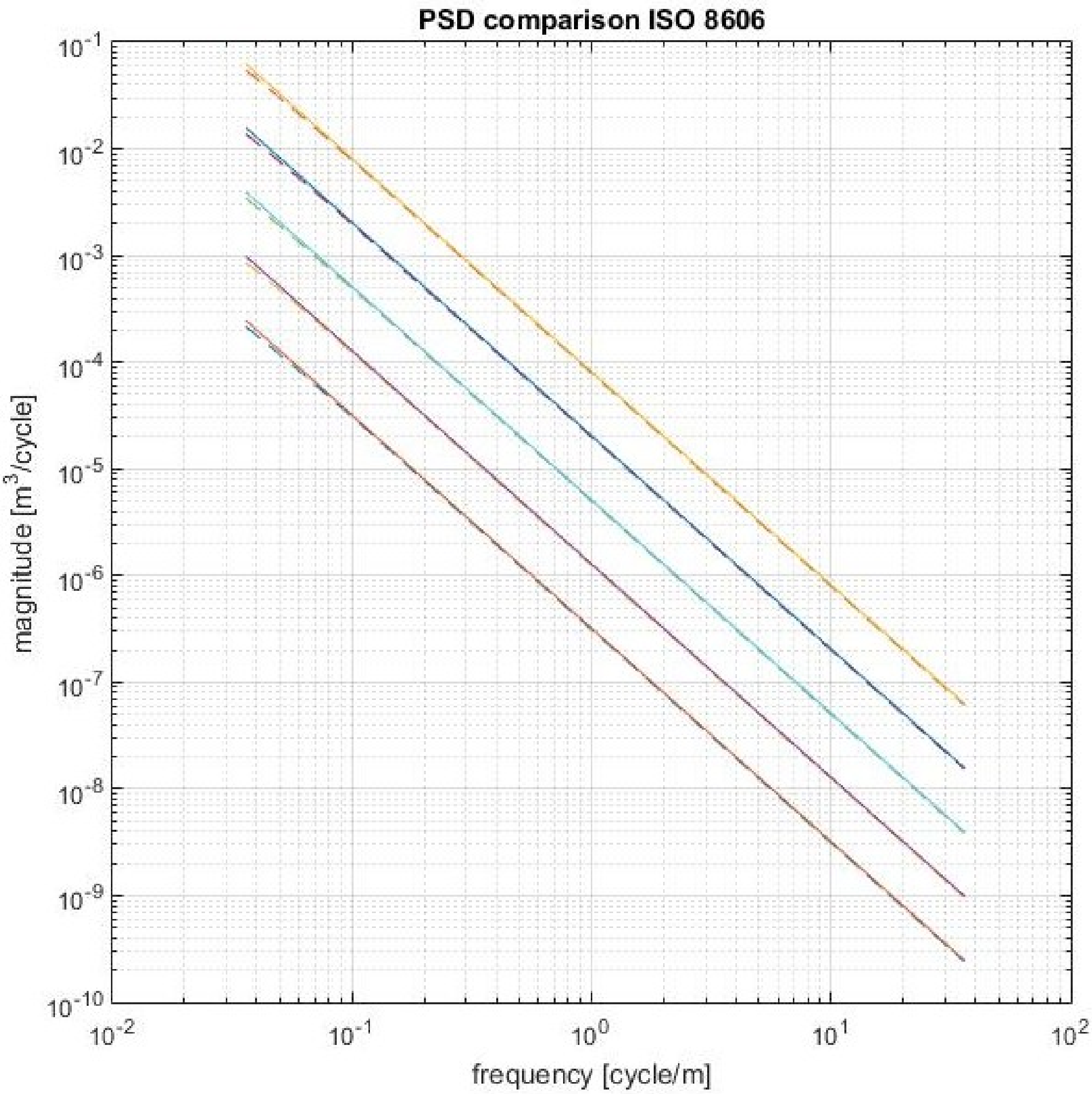

Fig. 3.2. Road Surface Classification.

Alpha and beta are correlation coefficients, but we can simplify left hand-side function for better fit, β =0. From the observation.
Now the new PSD function is :

$$\Psi(\omega) = COR * R(0)\frac{2\alpha(\alpha^2 + \omega^2)}{\omega^4 + 2\alpha^2\omega^2 + \alpha^4} = \frac{\Phi(\Omega_0)(\Omega_0)^2 V}{(\omega)^2} \quad (3.27)$$

It can be even more simples

$$\Psi(\omega) = COR * R(0)\frac{2\alpha}{(\alpha^2 + \omega^2)} = \frac{\Phi(\Omega_0)(\Omega_0)^2 V}{(\omega)^2} \quad (3.28)$$

This indicates that the road profile can be obtained from integrating a white noise (i.e. a random walk) in time domain. While to prevent standard deviation from going up with time as the integration period is increased. In the road roughness PSD distribution is modified as

$$\Psi(\omega) = COR * R(0)\frac{2\alpha}{(\alpha^2+\omega^2)} = \frac{2\alpha 1V\sigma^2}{(\alpha 1^2V^2+\omega^2)} \qquad (3.29)$$

Where

$\sigma^2 = COR * R(0) = COR * \Phi(\Omega_0)$ denotes the road roughness variance and
V the vehicle speed, whereas
$\alpha 1$ depends on the type of road surface.

Since the spectral density of the road profile can be factored as

$$\Psi(\omega) = \frac{2\alpha 1V\sigma^2}{(\alpha 1V + j\omega)(\alpha 1V - j\omega)} = H(\omega)\Psi_w H(-\omega)^T \qquad (3.30)$$

Where $H(\omega)$ is the frequency response function of the shaping filter, $\Psi_w = 2\alpha 1V\sigma^2$ is the spectral density of a white noise process[4].

Hence, if the vehicle runs with constant velocity V, then the road profile signal, Xr(t), whose PSD is given by ISO, may be obtained as the output of a linear filter expressed by the differential equation

$$\frac{dXr(t)}{dt} = -\alpha 1VXr(t) + w(t) \qquad (3.31)$$

where w(t) is a white noise process with the spectral density $\Psi_w = 2\alpha 1V\sigma^2$.

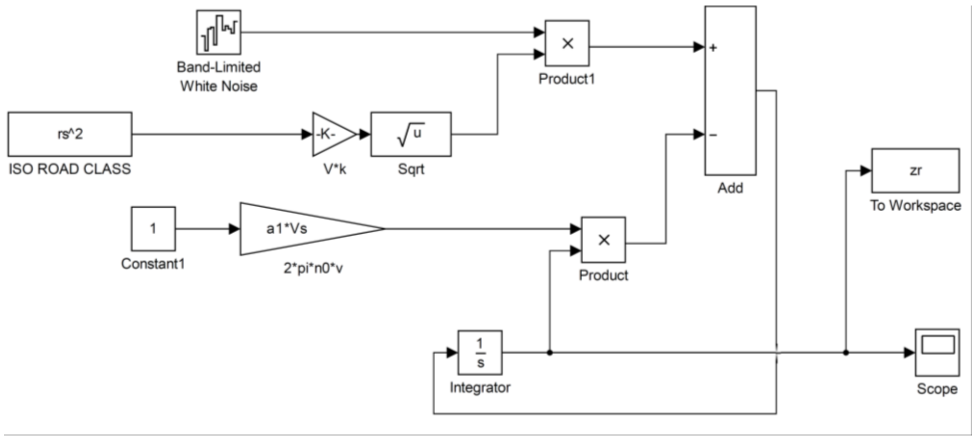

Fig. 3.3. Random Road Simulink Model.

```
% Shaping filter
close all
clc
class=[16 64 256 1024 4069]*1e-6;
i=3; % road classification index
rs=class(i);
xt=zr.data; % datas from simulink
time=zr.time; %
sigma=0.004;
```

```
a=0.127;
ww=0:0.01:50;
om0=1; % ref wave number rad/m
k=2; % waveness
Tsamp=time(6)-time(5);
V=20;
%% Road
figure(1);
plot(time*V,100*xt);
xlabel('road length[m]');
ylabel('amplitude [cm]');
title('Random road class C')
grid on
%% Calculate an 8-times averaged spectrum with pwelch
nx = length(xt);
na = 20;
w = blackmanharris(floor(nx/na)); % blackmanharris (good)
[Pxx,f] = pwelch(xt,w,0,[],1/Tsamp);
% Plot and mark the above
figure(2)
loglog(f/V,Pxx*V); % blackmanharris PSD
hold on
w = hanning(floor(nx/na)); % blackmanharris (good)
[Pxx,f] = pwelch(xt,w,0,[],1/Tsamp);
loglog(f/V,Pxx*V);
xlabel('Frequency [cycle/m]');
ylabel('Power Density [m^3/cycle]');
wmax=max(log(f/V));
%% ISO
n=f/V;
n0=0.1;
PSD=class(i)*(n/n0).^-k;
loglog(n,PSD);
hold on
%%
Ro=class(i);
ca=0.0127;
cb=0;
a=ca*V;
b=cb*V;
w=f;
PSD=0.405*Ro*2*a*(a^2+b^2+w.^2)./(w.^4+2*(a^2-
b^2).*w.^2+(a^2+b^2)^2); % page 47
om0=1;
loglog(n,PSD*V,'--');
hold on;
grid on
```

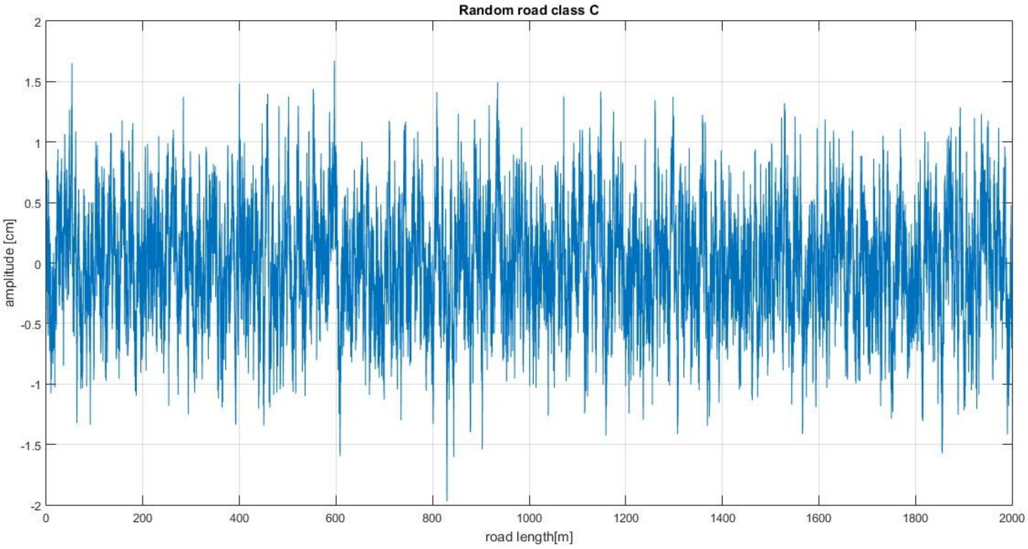

Fig. 3.4. Random Road Simulation.

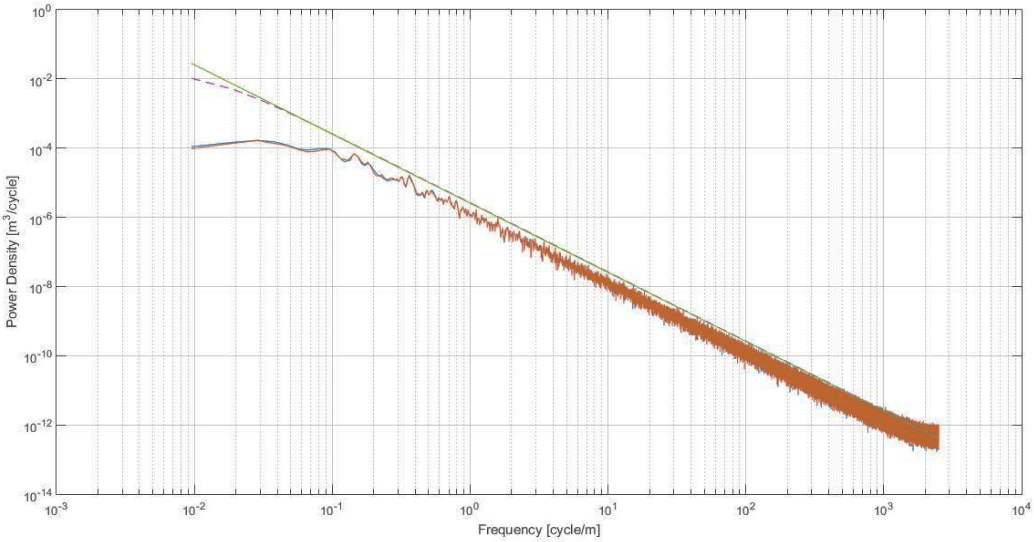

Fig. 3.5. PSD of the random road.

The result from the random road simulation is very close to ISO standards. Range of the road disturbance is equal to 4 cm and the distance of the simulation enough long to use it for simulations related to dynamical, electromechanical systems in order to design electrical circuit.

4. Passive Mechanical System

4.1. Background of the dynamic models of the conventional vehicle suspensions

Basic elements of the passenger car suspension are a spring (a coil spring, an air spring or leaf spring) and a shock absorber. The spring and damping coefficients are selected according to the requirements of comfort, road surface and processing. However, conventional suspension systems tradeoff between ride comfort and road holding since their spring and damping factors cannot be matched to the driving forces and road conditions. They can provide good comfort when traveling and keeping the road only in accordance with the developed conditions.

The first step is to model a precise dynamic model of vehicle suspension, and the second is to develop and select a suitable control strategy that has a significant impact on the compromise between ride comfort and road holding. In general, the vehicle dynamics model of a real vehicle is approximate. Approach is a challenging problem. In terms of control design, a relatively simple vehicle model makes sense.

The dynamic models of conventional vehicle suspensions have three combinations. An oil damper, a colloidal damper without compression spring (Fig. 4.2) and a colloidal damper mounted parallel to the compression coil spring (Fig. 4.3) are mounted parallel to the compression coil spring (Fig. 4.1). In (a), parts of Figs. 1-3, models with two degrees of freedom are considered based on the following assumptions. To simplify the problem, the driving speed is constant; there is no forward / backward and / or axial rolling of the vehicle body. The contact between tire and road is linear. Finally, suspension and tires have linear characteristics [2].

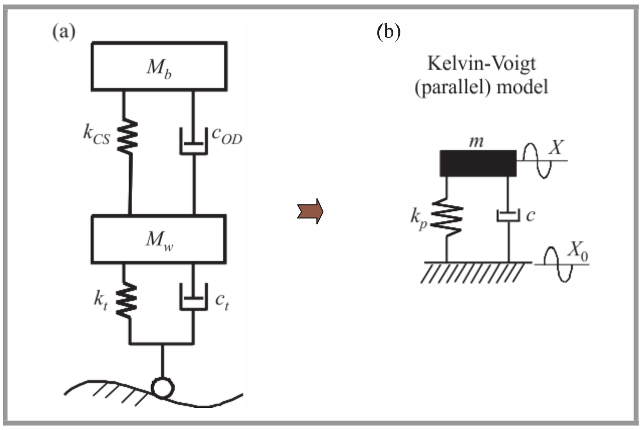

Fig. 4.1. Two-degrees of freedom (a) and single-degree of freedom (b) models for oil damper mounted in parallel with compression helical spring [2].

On the Figs. 4.1–4.3, illustrated three different types of the suspension system, Where,

M_b - the body (sprung) mass
M_W - the wheel (unsprung) mass
k_t - the tire spring constant
k_{CS} - the compression spring's constant
k_{CD} - spring of constant
ct - the tire damping coefficient
c_{OD} - the damping coefficient of the oil damper
c_{CD} - the damping coefficient of the colloidal damper.

In conventional suspension (Figure 4.1), the compression spring provides the necessary restoring force to bring the suspension back to its original position after a compression-expansion cycle [2].

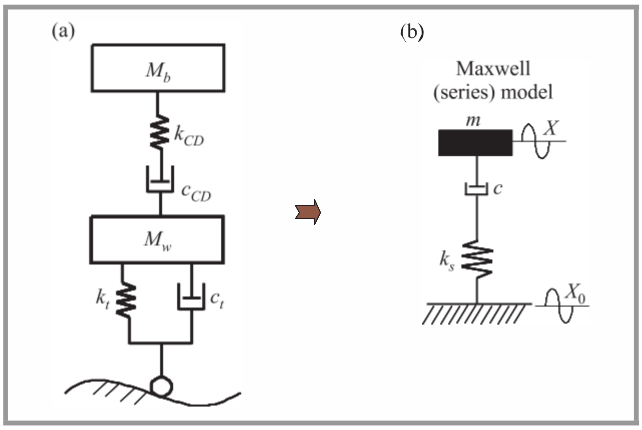

Fig. 4.2. Two-degrees of freedom (a) and one-degree of freedom (b) models for colloidal damper without compression helical spring mounted in parallel [2].

The spring stores the energy of shocks and vibrations during the compression phase and is then transmitted and dissipated by the oil damper during extension. On the other hand, the colloidal damper can deliver the restoring force [2] and the spring can be omitted (Fig. 4.2). Thus, the colloidal damper is a machine element with a dual function, an absorber and a constant K_{CD} spring.

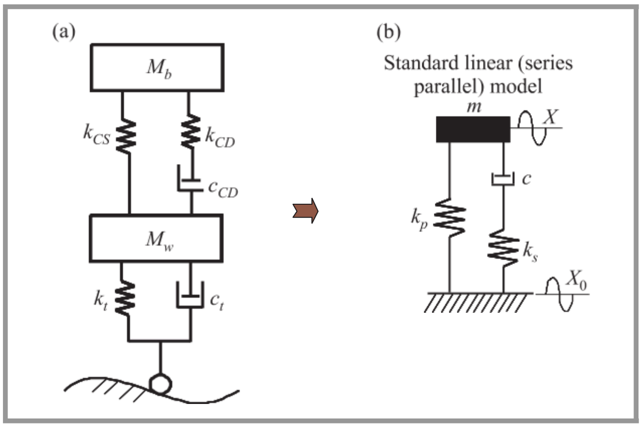

Fig. 4.3. Two-degrees of freedom (a) and one-degree of freedom (b) models for colloidal damper mounted in parallel with compression helical spring [2].

In addition, the colloid damper is able to dissipate impact energy when it is compressed, thereby reducing the delay between excitation and reaction, since it has a higher response speed to the excitement, it is expected that the comfort of riding a vehicle can be greatly improved.

For the model shown in Figure 4.1, two peaks were observed, a first resonant peak with a lower frequency f_n approximately equal to the body mass of the vehicle (sprung) and a second resonant peak at a higher frequency f_t approximately equal to the wheel (unsprung) mass[2]:

$$f_n = \frac{\omega_n}{2\pi} = \frac{1}{2\pi}\sqrt{\frac{k_{CS}}{M_b}}, \quad f_t = \frac{\omega_t}{2\pi} = \frac{1}{2\pi}\sqrt{\frac{k_t}{M_w}} \qquad (4.1).$$

In general, when designing the actual suspension of a vehicle (oil damper installed parallel to the spring) two opposite requirements are met: to reduce the first resonance peak, it is desirable to use a low damping at a low frequency f_n, but on the other hand, low damping of c_{OD} is required at a higher frequency f_t to reduce the second resonant peak. From equation (4.1) in order to improve the comfort of driving a car, the suspension designer has the only alternative from a technical point of view: minimizing the transfer function of vibrations from a rough road to the car body in the entire frequency range (0.1-100 Hz).

One way to passively reduce damping at higher frequencies is to use a "relaxation damper" in which the c_{OD} flap is replaced by a Maxwell block consisting of a flap, for example. c_{CD} and k_{CD} a spring installed in series. The model with two degrees of freedom can be further simplified to a fourth-degree vehicle with one degree of freedom by determining the vehicle equivalent mass, the equivalent constant springs of parallel k_p and k_s spring coefficients and an equivalent damping coefficients c of shock absorbers as follows:

$$\begin{cases} m = M_b + M_w \\ \dfrac{1}{k_p} = \dfrac{1}{k_t} + \dfrac{1}{k_{cs}}\dfrac{M_b}{M_w} \\ k_s = k_{CD} \\ c = c_{OD} + c_t \ or \ c = c_{CD} + c_t \end{cases} \qquad (4.2)$$

Thus, the considered suspensions can be modeled as follows:

- A Kelvin-Voigt model, consisted of a dashpot and an elastic element connected in parallel, can describe oil damper placed in parallel with a compression spring (Fig. 4.1).
- A Maxwell model, consisted of a dashpot and an elastic element connected in series (Fig. 4.2), can describe colloidal damper without attached compression spring.
- Colloidal damper mounted in parallel with a compression helical spring, can be described by a standard linear model, consisted of a Maxwell unit connected in parallel with an elastic element (Fig. 4.3) [2].

However, before choosing optimal damping and spring coefficients for the suspension design. One must consider many factors when packaging the damper into the suspension system. These include required wheel travel, jounce bumper travel, desired wheel rates, strength requirements and packaging constraints. Probably the most important is motion ratio. The ratio of the wheel displacement to spring or damping displacement gives us a better overview of the performance of the suspension system.

For a McPherson suspension, these motion ratios are equal to$cos\alpha$. From this point, we have two type damping and spring coefficients for the shock absorber. In order to find an equivalent spring and damper parameters of the McPherson suspension, we use m equal to quarter of the vehicle body mass. The spring k and damper c make an angle α with the direction of wheel motion. They are also displaced (b – a) from the wheel center.

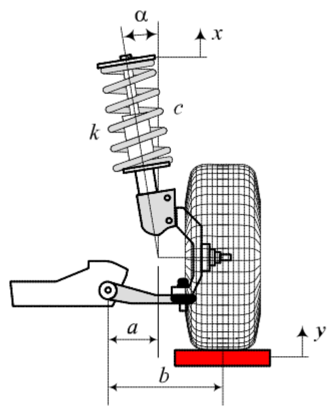

Figure 4.4 Illustrates a McPherson strut mechanism.

Laterally, the equivalent spring k_e and damper c_e are

$$k_e = k\left(\frac{a}{b}cos\alpha\right)^2 \quad (4.3)$$

$$c_e = c\left(\frac{a}{b}cos\alpha\right)^2 \quad (4.4)$$

As an application assume that we have determined the following stiffness and damping because of an optimization algorithm:

k_e= 9869.6 N/m
c_e= 87.965 Ns/m

The actual k and c for a McPherson suspension with

a = 19 cm b = 32 cm α = 27 deg

would be

k = 35264 N/m c = 314.3 Ns/m

The inclined position of the vehicle suspension gives us more spring and damper movement that improves energy dissipation also it has better structural and compact design.

4.2. Quarter car system with single degree of freedom

The base excitation problem as a simplified model of the quarter car system was studied in order to learn its mechanical behavior for low frequencies. Base motion is y(t)=Y sin(ωbt) which can be mentioned as road disturbance, and the body response is x(t).

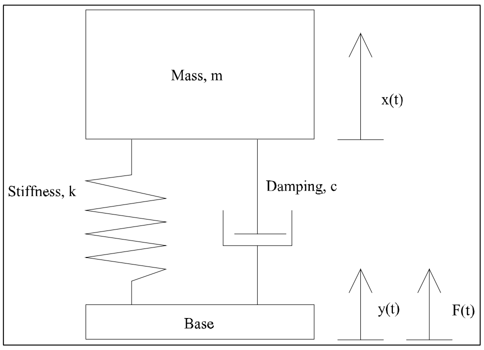

Fig. 4.5. Typical single degree of freedom system subject to base excitation.

The equation of motion for this system is:

$$m\ddot{x} + c(\dot{x} - \dot{y}) + k(x - y) = 0. \quad (4.5)$$

Using the assumed form for the motion, we can substitute for y and its derivative, resulting in:

$$m\ddot{x} + c\dot{x} + kx = \mathrm{c}Y\,\omega_b \cos\omega_b t + \mathrm{k}Y \sin\omega_b t, \quad (4.6)$$

which when divided through by the mass, yields

$$\ddot{x} + 2\zeta\omega\dot{x} + \omega^2 x = 2\zeta\omega\omega_b\, cos\omega_b t + \omega^2 Y\, sin\omega_b t. \quad (4.7)$$

The homogeneous solution is of the form:

$$xh = Ae{-}\zeta\omega t \sin(\omega_d t + \theta) \quad (4.8)$$

The expression for each part of the solution is similar to the expression for the entire sinusoidal forced function. The expression for each part of the solution is similar to the expression for the total sinusoidal forced function. A sinusoidal term gives a sinusoidal solution, and the cosine term forms a cosine solution. If we find these solutions and combine their sum into a sinusoid:

:

$$x_p = A_o \cos(\omega_b t - \varphi 1 - \varphi 2) \quad (4.9)$$

where

$$A_o = \omega Y\sqrt{\frac{\omega^2 + (2\zeta\omega_b)^2}{(\omega^2 - \omega_b^2)^2 + (2\zeta\omega\omega_b)^2}},\ \phi_1 = \tan^{-1}\frac{2\zeta\omega\omega_b}{\omega^2 - \omega_b^2},\ \phi_2 = \tan^{-1}\frac{\omega}{2\zeta\omega_b} \quad (4.10)$$

Thus, the complete solution is the sum of the homogeneous and particular solutions, or:

$$x(t) = Ae{-}\zeta\omega t \sin(\omega_d t + \theta) + Ao \cos(\omega_b t - \varphi_1 - \varphi_2) \quad (4.11).$$

This equation tells us about the movement of the mass. First, the special solution is the stationary response and the homogeneous solution is the transient response. This applies to the following excitement programs

```
clear all
close all
clc
y0=input('Enter the base excitation magnitude.[m] ');
zeta=input('Enter the damping ratio (zeta). ');
if (zeta<0|zeta>=1) % The usual test on damping ratio.
error('Damping ratio not in acceptable range!')
end
ks=input('Enter the spring stiffness [N/m]');
mass=input('Enter the mass [kg]');
wn=sqrt(ks/mass);
tf=10;
t=0:tf/1000:tf;
for k=1:3
wb(k)=input('Enter a base excitation frequency.[rad/sec] ' );
end
for m=1:3
%
wd=wn*sqrt(1-zeta^2);
phi1=atan2(2*zeta*wn*wb(m),(wn^2-wb(m)^2));
phi2=atan2(wn,2*zeta*wb(m));
xi=phi1+phi2;
Z1=(-zeta*wn-wb(m)*tan(xi)+sqrt((zeta*wn)^2+2*zeta* ...
wn*wb(m)*tan(xi)+(wb(m)*tan(xi))^2+wd^2))/wd;
Z2=(-zeta*wn-wb(m)*tan(xi)-sqrt((zeta*wn)^2+2*zeta* ...
wn*wb(m)*tan(xi)+(wb(m)*tan(xi))^2+wd^2))/wd;
Anum=sqrt((wn^2+(2*zeta*wb(m))^2)/((wn^2-wb(m)^2)^2+(2* ...
zeta*wb(m)*wn)^2))*wn*y0;
Bnum1=(-wd*cos(xi)+Z1*zeta*wn*cos(xi)+Z1*wb(m)*sin(xi));
Bnum2=(-wd*cos(xi)+Z2*zeta*wn*cos(xi)+Z2*wb(m)*sin(xi));
Aden1=wd*Z1;
Aden2=wd*Z2;
A1=Anum*Bnum1/Aden1;
A2=Anum*Bnum2/Aden2;
th1=2*atan(Z1);
th2=2*atan(Z2);
y1(m,:)=A1*exp(-zeta*wn*t).*sin(wd*t+th1);
y2(m,:)=A2*exp(-zeta*wn*t).*sin(wd*t+th2);

end
for j=1:3
A=sqrt((wn^2+(2*zeta*wb(j))^2)/((wn^2-wb(j)^2)^2+(2*zeta* ...
wn*wb(j))^2));
phi1=atan2(2*zeta*wn*wb(j),(wn^2-wb(j)^2));
phi2=atan2(wn,(2*zeta*wb(j)));
xp(j,:)=wn*y0*A*cos(wb(j)*t-phi1-phi2);
end
if (xp(1,1)+y1(1,1)==xp(2,1)+y1(2,1)==xp(3,1)+y1(3,1)==0)
x=xp+y1;
else
x=xp+y2;
end
figure(1)
for i=1:3
subplot(3,1,i)
```

```
plot(t,x(i,:))
ylabel('Response x');
title(['Base Excitation with wb=',num2str(wb(i)), ...
'and wn=',num2str(wn)]);
grid
end
figure(2)
for i=1:3
subplot(3,1,i)
plot(t,y0*sin(wb(i)*t));
ylabel('Response y');
title(['Base Excitation with wb=',num2str(wb(i)), ...
'and wn=',num2str(wn)]);
grid
end
figure(3)
for i=1:3
subplot(3,1,i)
plot(t,x(i,:));
hold on;
plot(t,y0*sin(wb(i)*t),'r');
ylabel('Response x vs y');
title(['Base Excitation with wb=',num2str(wb(i)), ...
'and wn=',num2str(wn)]);
grid
end
xlabel('Time, seconds')
```

In Fig. 4.5 demonstrates the effects of changing the excitation frequency while retaining all other parameters. In a steady state, about three seconds in advance, note that the oscillation frequency increases with the fundamental frequency. This is to be expected, since the main part of the excitation dominates in the stationary state. The lower graph with $\omega_b = 5$ should be especially noted. In the transition part, the answer has the form of a sum of two sinusoids; these are, of course, temporary and stationary functions. Since excitation of the earth has such a high frequency, this graph best shows what happens between transient and stable responses. The average point of vibration caused by a stable response exponentially approaches with an increase in the zero moment with a decrease in the transient response.

The base excitation magnitude.[m]	0.1
The damping ratio (zeta).	0.3
The spring stiffness [n/m]	30e3
The mass [kg]	500
A base excitation frequency.[rad/sec]	4
A base excitation frequency.[rad/sec]	5
A base excitation frequency.[rad/sec]	10

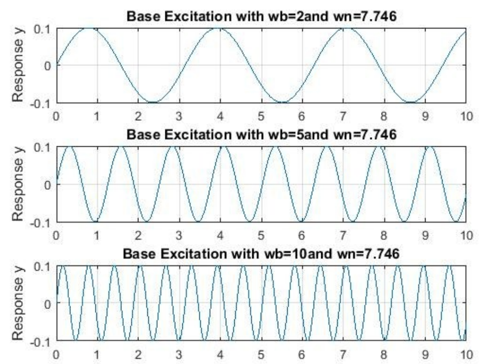

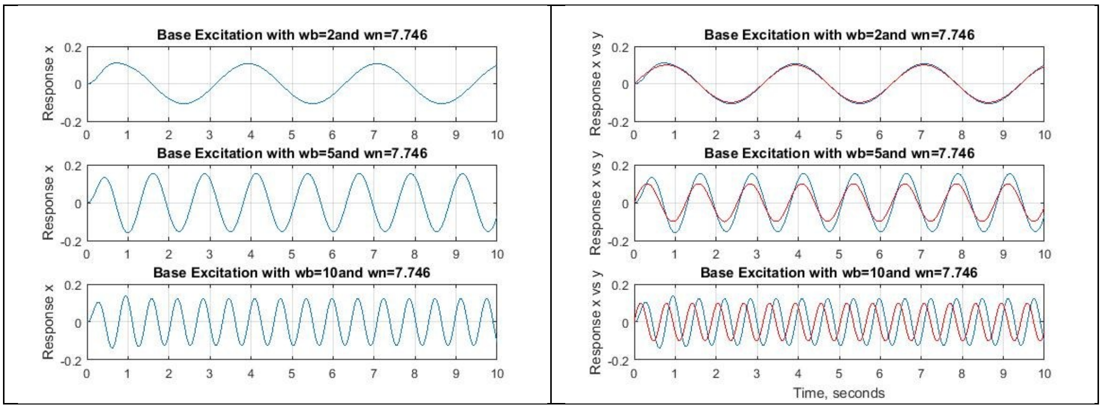

Fig 4.6. The effects of changing the excitation frequency.

Figure 4.6 shows the graphs for three different vibration amplitudes. The differences caused by the change in amplitude are what one would expect; The maximum amplitude of the total vibration and steady-state response increases with increasing input amplitude.

```
clear all
close all
clc
wb=input('Enter the base excitation frequency. ');
zeta=input('Enter the damping ratio (zeta). ');
if (zeta<0|zeta>=1) % The usual test on damping ratio.
error('Damping ratio not in acceptable range!')
end
wn=4;
tf=10;
t=0:tf/1000:tf;
for k=1:3
y0(k)=input('Enter a base excitation magnitude. ');
end
for m=1:3
wd=wn*sqrt(1-zeta^2);
phi1=atan2(2*zeta*wn*wb,(wn^2-wb^2));
phi2=atan2(wn,2*zeta*wb);
xi=phi1+phi2;
Z1=(-zeta*wn-wb*tan(xi)+sqrt((zeta*wn)^2+2*zeta* ...
wn*wb*tan(xi)+(wb*tan(xi))^2+wd^2))/wd;
Z2=(-zeta*wn-wb*tan(xi)-sqrt((zeta*wn)^2+2*zeta* ...
wn*wb*tan(xi)+(wb*tan(xi))^2+wd^2))/wd;
Anum=sqrt((wn^2+(2*zeta*wb)^2)/((wn^2-wb^2)^2+(2* ...
zeta*wb*wn)^2))*wn*y0(m);
Bnum1=(-wd*cos(xi)+Z1*zeta*wn*cos(xi)+Z1*wb*sin(xi));
Bnum2=(-wd*cos(xi)+Z2*zeta*wn*cos(xi)+Z2*wb*sin(xi));
Aden1=wd*Z1; Aden2=wd*Z2;
A1=Anum*Bnum1/Aden1;
A2=Anum*Bnum2/Aden2;
th1=2*atan(Z1);
th2=2*atan(Z2);
y1(m,:)=A1*exp(-zeta*wn*t).*sin(wd*t+th1);
y2(m,:)=A2*exp(-zeta*wn*t).*sin(wd*t+th2);
end
for j=1:3
A=sqrt((wn^2+(2*zeta*wb)^2)/((wn^2-wb^2)^2+(2*zeta* ...
wn*wb)^2));
phi1=atan2(2*zeta*wn*wb,(wn^2-wb^2));
phi2=atan2(wn,(2*zeta*wb));
xp(j,:)=wn*y0(j)*A*cos(wb*t-phi1-phi2);
```

```
end
if (xp(1,1)+y1(1,1)==xp(2,1)+y1(2,1)==xp(3,1)+y1(3,1)==0)
x=xp+y1;
else
x=xp+y2;
end
for i=1:3
subplot(3,1,i)
plot(t,x(i,:))
ylabel('Response x');
title(['Base Excitation with wb=',num2str(wb), ...
', wn=',num2str(wn),', and y0=',num2str(y0(i))]);
grid
end
xlabel('Time, seconds')
```

The base excitation frequency. 7.746
The damping ratio (zeta). 0.3
A base excitation magnitude. 0.1
A base excitation magnitude. 0.05
A base excitation magnitude. 0.025

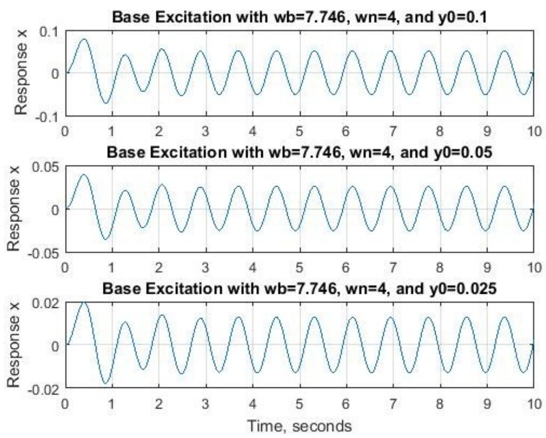

Fig 4.7. The effects of changing the excitation amplitude.

The plot in Figure 4.7 for different damping ratios show two effects of changing the damping ratio. First, the change in the damping ratio causes the length of the transition period to vary; an increase of ζ causes the transition period to decrease, as the diagrams show. In addition, the change in the attenuation ratio causes a change in the frequency of the transient oscillation. Here, too, an increase in ζ leads to a decrease in the dampened natural frequency, although the decline is not fully apparent when considering only the plots. This is because the diagrams also include the base excitation states (stationary states) whose frequency has not changed.

```
y0=input('Enter the base excitation magnitude. ');
wb=input('Enter the base excitation frequency. ');
wn=4;
tf=10;
t=0:tf/1000:tf;
for k=1:3
zeta(k)=input('Enter a damping ratio (zeta). ');
if (zeta(k)<0|zeta(k)>=1) % The usual test on damping ratio.
error('Damping ratio not in acceptable range!')
end
end
for m=1:3
wd=wn*sqrt(1-zeta(m)^2);
phi1=atan2(2*zeta(m)*wn*wb,(wn^2-wb^2));
phi2=atan2(wn,2*zeta(m)*wb);
xi=phi1+phi2;
```

```
Z1=(-zeta(m)*wn-wb*tan(xi)+sqrt((zeta(m)*wn)^2+2*zeta(m)* ...
wn*wb*tan(xi)+(wb*tan(xi))^2+wd^2))/wd;
Z2=(-zeta(m)*wn-wb*tan(xi)-sqrt((zeta(m)*wn)^2+2*zeta(m)* ...
wn*wb*tan(xi)+(wb*tan(xi))^2+wd^2))/wd;
Anum=sqrt((wn^2+(2*zeta(m)*wb)^2)/((wn^2-wb^2)^2+(2* ...
zeta(m)*wb*wn)^2))*wn*y0;
Bnum1=(-wd*cos(xi)+Z1*zeta(m)*wn*cos(xi)+Z1*wb*sin(xi));
Bnum2=(-wd*cos(xi)+Z2*zeta(m)*wn*cos(xi)+Z2*wb*sin(xi));
Aden1=wd*Z1;
Aden2=wd*Z2;
A1=Anum*Bnum1/Aden1;
A2=Anum*Bnum2/Aden2;
th1=2*atan(Z1);
th2=2*atan(Z2);
y1(m,:)=A1*exp(-zeta(m)*wn*t).*sin(wd*t+th1);
y2(m,:)=A2*exp(-zeta(m)*wn*t).*sin(wd*t+th2);
end
for j=1:3
A=sqrt((wn^2+(2*zeta(j)*wb)^2)/((wn^2-wb^2)^2+(2*zeta(j)* ...
wn*wb)^2));
phi1=atan2(2*zeta(j)*wn*wb,(wn^2-wb^2));
phi2=atan2(wn,(2*zeta(j)*wb));
xp(j,:)=wn*y0*A*cos(wb*t-phi1-phi2);
end
if (xp(1,1)+y1(1,1)==xp(2,1)+y1(2,1)==xp(3,1)+y1(3,1)==0)
x=xp+y1;
else
x=xp+y2;
end
for i=1:3
subplot(3,1,i)
plot(t,x(i,:))
ylabel('Response x');
title(['Base Excitation with wb=',num2str(wb), ...
'and zeta=',num2str(zeta(i))]);
grid
end
xlabel('Time, seconds')
```

The base excitation magnitude. 0.1
The base excitation frequency. 7.746
A damping ratio (zeta). 0.3
A damping ratio (zeta). 0.2
A damping ratio (zeta). 0.1

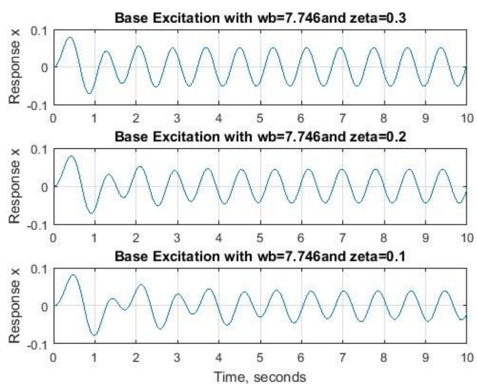

Fig 4.8. The effects of changing the damping ratio.

With this approach, the relative displacement of the two parts of the structure becomes an important factor instead of displacement of the structure relative to the road.

4.3. Quarter car system with non-harmonic excitations.

The output of the system to any input can be expressed by the impulse response function. This is the essence of the impulse response approach for determining the forced response of a dynamic system. Without limiting the generality, we assume that the input of the system u (t) starts with t = 0; that is [8]

$$u(t) = 0 \; for \; t < 0 \quad (4.12)$$

For physically realizable systems, the current response is independent of future input values. Consequently,

$$y(t) = 0 \; for \; t < 0 \quad (4.13)$$

and

$$h(t) = 0 \; for \; t < 0 \quad (4.14)$$

where y (t) is the response of the system to the general excitation u (t). In addition, if the system is a system with constant parameters, the response is independent of the time source used for input. This is expressed mathematically as follows: if the answer to the input u (t) satisfying equation (4.10) is y (t), satisfies equation (4.11), then the answer to the input $u(t-\tau)$

$$u(t-\tau) = 0 \; for \; t < \tau \quad (4.15)$$

is $y(t-\tau)$, and it satisfies

$$y(t-\tau) = 0 \; for \; t < \tau \quad (4.16)$$

This situation is illustrated in Fig. 4.8. It follows that the delayed-impulse input $\delta(t-\tau)$, having time delay τ, produces the delayed response $h(t-\tau)$.

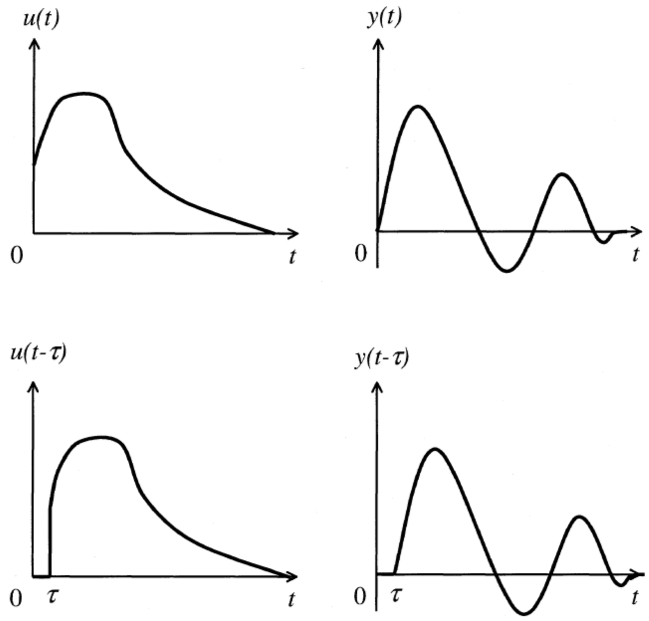

Fig 4.9. Response for the delayed-impulse input

A given input $u(t)$ can be divided approximately into a series of pulses of width $\Delta\tau$ and magnitude $u(\tau)\Delta\tau$. In Figure 4.9 [8], for $\Delta\tau \to 0$, the pulse shown by the shaded area becomes an impulse acting at $t = \tau$, having the magnitude $u(\tau)d\tau$.

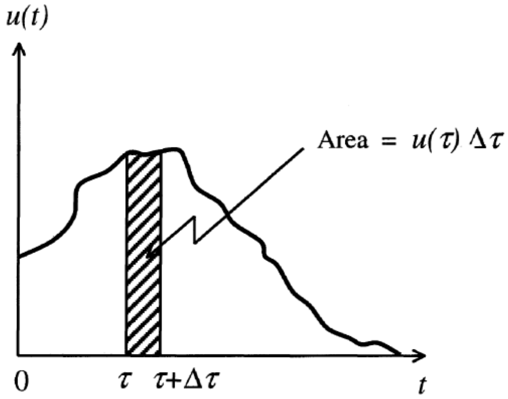

Fig 4.10. Non generic input function

This impulse is given by $\delta(t - \tau)u(\tau)d\tau$. In a linear, constant-parameter system, it produces the response $h(t-\tau)u(\tau)d\tau$. The overall response $y(t)$ is obtained by integrating the entire time duration of the input $u(t)$, as

$$y(t) = \int_{0}^{+\infty} h(t-\tau)u(\tau)d\tau \qquad (4.17)$$

Equation (4.15) is known as the convolution integral. Actually it is the forced response under zero initial conditions. In view of equation (4.12), it follows that $h(t-\tau) = 0$ for $\tau > t$. Consequently, the upper limit of integration in equation (4.15) could be made equal to t without affecting the result. The lower limit of integration in equation (4.15) could be made $-\infty$. Furthermore, by introducing the change of variable $\tau \rightarrow t - \tau$, an alternative version of the convolution integral is obtained. Several valid versions of the convolution integral (or response equation) for linear, constant-parameter systems are as follows:

$$y(t) = \int_{0}^{t} h(\tau)u(t-\tau)d\tau \qquad (4.18)$$

In fact, the lower limit of integration in the convolution integral could be any value satisfying $\tau \leq 0$, and the upper limit could be any value satisfying $\tau \geq t$. The use of a particular pair of integration limits depends on whether the functions $h(t)$ and $u(t)$ implicitly satisfy the conditions given by equations (4.11) and (4.12) or these conditions have to be imposed on them by means of the proper integration limits.

It should be emphasized that the response given by the convolution integral takes the zero initial state and is known as the zero-state response, since the impulse response itself assumes a zero initial state. As already mentioned, this is not necessarily the same as a "special solution" in mathematical analysis. If t ($t \rightarrow \infty$), increases, this solution also approaches the steady state response, called y_{ss}, which is usually a definite solution. The impulse response of the system is the inverse Laplace transform of the transfer function.

Total Response (T) $=$ Homogeneous solution (H) $+$ Particular integral (P)

$=$ Free response(X) $+$ Forced response (F)

$$= (\text{Initial - condition response})(X) + (\text{Zero - initial - condition response})(F)$$
$$= (\text{Zero - input response})(X) + (\text{Zero - state response})(F)$$

Note: In general, $H \neq X$ and $P \neq F$
With no input (no forcing excitation), by definition, $H \equiv X$
At steady state, F becomes equal to P.

Convolution Integral: Response

$$y(t) = \int_0^{+\infty} h(t-\tau)u(\tau)d\tau = \int_0^{t} h(\tau)u(t-\tau)d\tau \quad (4.19)$$

where u = excitation (input) and h = impulse response function (response to a unit impulse input).

4.4. Quarter car system simulation with convolutional integral.

A simplified single degree of freedom model of an automobile suspension system is studied. In order to design electro-mechanical, electronic and electrical parts, preliminary simulation of the system is required. The suspension has a constant horizontal speed and it encounters a bump in the road of the shape shown in Fig. 4.10. The velocity of the quarter car suspension system is 20 m/s, m = 500 kg, k = 150,000 N/m, and ζ = 0.20.

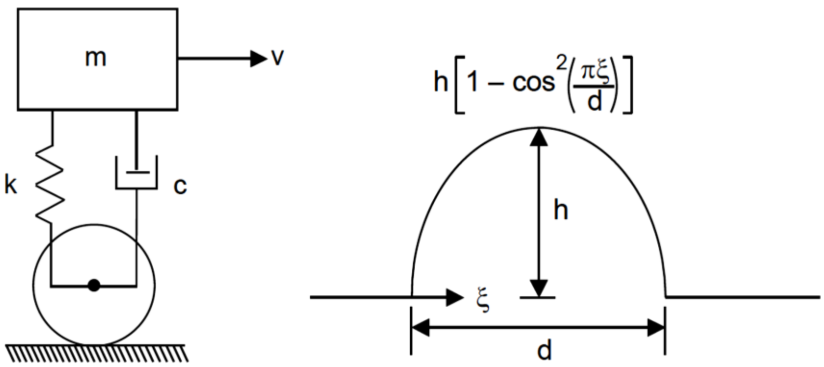

Fig 4.11. The quarter car system hits the bump

```
clear all
close all
clc
syms t tau
% input parameters
digits(10)
format short e
m=500; % sprung mass
k=150000; % stiffness
zeta=0.20; % damping coef
hb=0.1; % bump height meter
d=0.3; % longitudinal distance of the bump
```

```
v=20; % car velocity
% system parameters and constants
omega_n=sqrt(k/m); % Natural frequency
omega_d=omega_n*sqrt(1-zeta^2); % damped natural frequency
c1=pi/d;
% wheel displacement and velocity
% MATLAB 'Heaviside' for the unit step function
y=hb*(1-cos(pi*v*t)^2)*(1-sym('floor(heaviside(t-0.05))'));
ydot=hb*pi*sin(2*pi*v*tau)*(1-sym('floor(heaviside(tau-0.05))'));
%convolution integral evaluation
h=exp(-zeta*omega_n*(t-tau)).*sin(omega_d*(t-tau))/(m*omega_d);
g1=2*zeta*m*omega_n*ydot*h;
g2=k*y*h;
g1a=vpa(g1,5);
g2a=vpa(g2,5);
I1=int(g1a,tau,0,t);
I1a=vpa(I1,5);
I2=int(g2a,tau,0,t);
I2a=vpa(I2,5);
x1=I1a+I2a;
x=vpa(x1,5);
vel=diff(x);
acc=diff(vel);
time=0:0.001:0.05;
for i=1:length(time)
x1=subs(x,t,time(i));
xa(i)=vpa(x1);
end
xp=double(xa);
figure(1)
plot(time,1000*xp,'-');
xlabel('time(sec)')
ylabel('x(t)  [mm]')
legend ('unsprung mass')
grid on;
%% bump shape
timeb=0:0.001:0.05;
for i=1:length(timeb)
    y1=subs(hb*(1-cos(pi*v*t)^2)*(1-floor(sym('heaviside(t-
0.05)'))),t,timeb(i));
    ya(i)=vpa(y1);
end
figure (2)
plot(timeb*v*0.3,1000*ya,'r');
grid on;
xlabel('d[m]')
ylabel('x(t)  [mm]')
legend ('bump shape or wheel trajectory')
```

As I mentioned the bump shape is sine function with height 10 cm and width 30 cm. Our system has an effect of this bump for 0.015 sec. In fig 4.11 shows delayed response for the input force with max peak 12 [mm] that is significantly differs from max peak of the bump, this means the suspension taking a huge energy in order to stabilize the system.

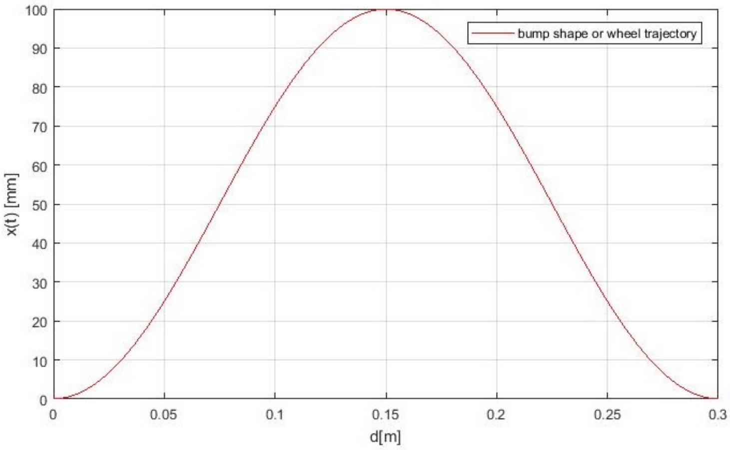

Fig 4.12. The function of the bump in MATLAB

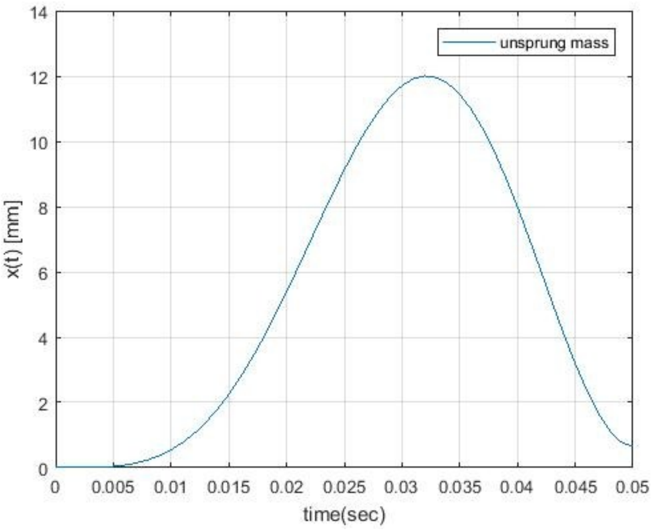

Fig 4.13. The response of the sprung mass.

4.5. A quarter-car model with double degree of freedom

A quarter-car model was used in the study of the passive and semi-active suspension system. Although the model is very simple and is considering only vertical vibration motions of the sprung mass and the unsprung mass.

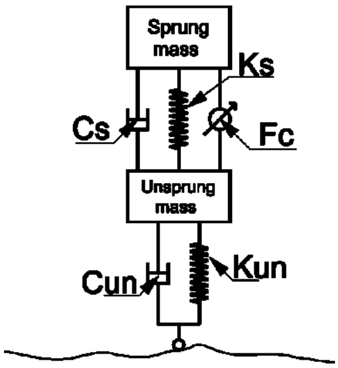

Fig.4.14. Quarter-car model

The suspension system, which will be replaced by the semi-active ER-fluid suspension system, is a Mac-Pherson strut. This suspension strut has a spring stiffness of 30000 N/m as is shown in Table 3, together with other parameters.

Parameter	Value
Unloaded mass	1546 kg
Maximum loaded mass	2065 kg
Unsprung mass	48.3 kg
Spring stiffness	30000 N/m
Tire stiffness min-max	3.1e5-3.7e5 N/m
Maximum compression (bump)	0.06 m
Maximum extension (rebound)	0.08 m

Table 4.1. The suspension system parameters

In order to study mathematical model of the system (Fig. 4.12) we will use Lagrange equations. In our case the system has two degree of freedom.

$$\frac{d}{dt}\left(\frac{\partial \mathcal{L}}{\partial \dot{q}_i}\right) - \frac{\partial \mathcal{L}}{\partial q_i} + \frac{\partial \mathcal{F}}{\partial \dot{q}_i} = \frac{\partial \delta L}{\partial \delta q_i} \quad (4.20)$$

Where:

Kinetic energy $\mathcal{T}$

Potential energy $\mathcal{U}$

Dissipative function $\mathcal{F}$

Virtual work $\partial \mathcal{L}$

The general coordinate system, $q = \begin{Bmatrix} x_s \\ x_{us} \end{Bmatrix}$

The sprung mass is supported with a semi-active suspension system consisting of a spring and a controllable damper. In the figure, m_s and m_{us} denote the sprung mass and the unsprung mass, respectively; k_s and k_{us} denote the stiffness; c_s and c_{us}denote the damping coefficient; and x_s, x_{us} and d denote the sprung-mass displacement, the unsprung-mass displacement, and the road disturbance, respectively. The ideal damping force f_d, is designed for this plant. The motion equations for the quarter-car model are given by

$$\begin{cases} m_s\ddot{x}_s + c_s(\dot{x}_s - \dot{x}_{us}) + k_s(x_s - x_{us}) + f_d = 0 \\ m_{us}\ddot{x}_{us} + c_s(\dot{x}_{us} - \dot{x}_s) + c_{us}(\dot{x}_{us} - \dot{d}) + k_s(x_{us} - x_s) + k_{us}(x_{us} - d) - f_d = 0 \end{cases} \quad (4.21)$$

In order to get basic ideas about the system we will use Simulink to identify passive mode characteristics. The Simulink system has only constant coefficients but further can be used as a plant with feedback controller.

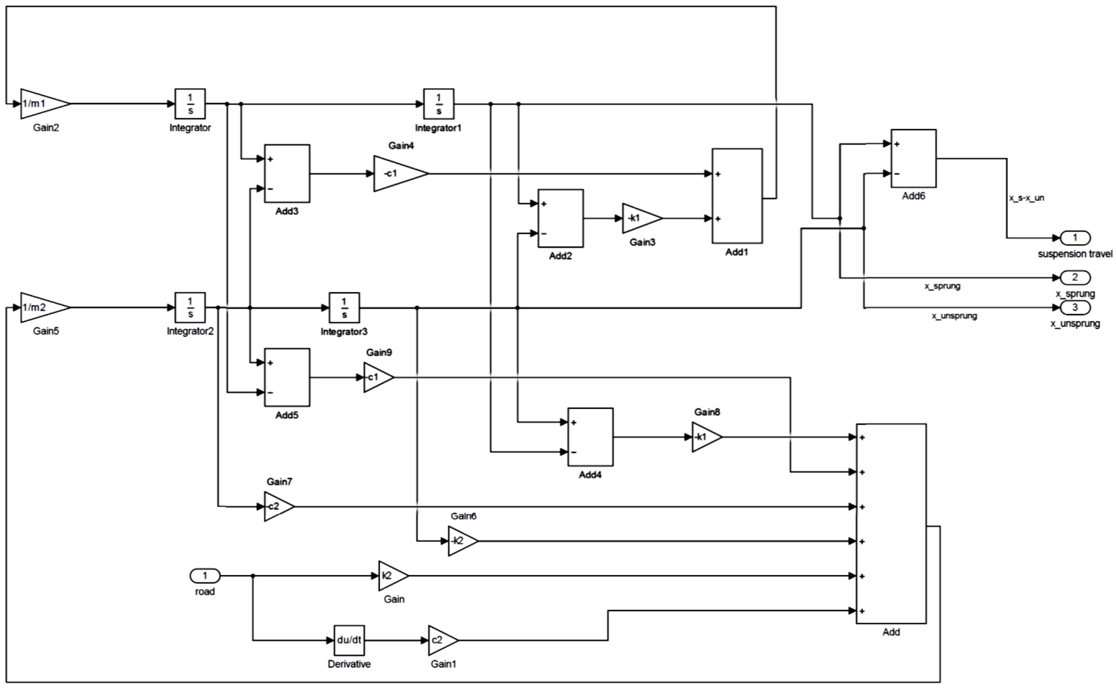

Fig. 4.15. Simulink model of the suspension system passive mode.

5. Active And Semi-active Mechanical System

5.1. Configuration of active suspension system

The development of microprocessor, sensor, and actuator technologies in 1980s yielded to control spring and damping coefficients of the suspension system, which allowed to create new types of suspension systems, or intelligent suspension system. These mechanical systems can be classified into two groups based on ways of generation of the required control forces: active and semi-active ones.

Dynamic suspension, as a rule, requires external force to create control capacity with the help of pneumatic or hydraulic actuators. An active suspension system has better performance than the passive and the semi-active counterparts. Be that as it may, complexity, high energy consumption and high cost of the active suspension system makes very limited for practical use.

At the same time, the semi-dynamic suspension structures, taking into account electrorheological and magnetorheological innovations, were of great importance for effortless, fast reaction and little energy consumption. But the semi-active control devices do not have input force, therefore, they do not have chance of the loss of stability (in the bounded input/bounded output sense). Examples of such devices include air springs and switchable shock absorbers, dampers with controllable fluids (e.g., and magnetorheological fluids), various self-leveling solutions, as well as systems like hydro-pneumatic, hydrolastic, and hydrogas suspensions.

Both of suspension systems has its own advantages and disadvantages. Research and development of automotive active suspension and investigated comparisons between various vehicle suspensions from the aspects of structure, weight, cost, ride comfort, handling performance, reliability, dynamic performance, energy recovery, and commercial maturity. The comparison results are given in Table 5.1. The design of an intelligent suspension is actually a control engineering problem. The success of design of an intelligent suspension for improving the ride comfort and road holding is determined by two steps like other control systems. [9].

Parameters	**Passive suspensions**	**Semi-active suspensions**	**Hydraulic or pneumatic active suspensions**	**Electromagnetic active suspensions**
Structure	Simplest	Complex	Most complex	Simple
Weight or volume	Lowest	Low	High	Highest
Cost	Lowest	Low	Highest	High
Ride comfort	Bad	Medium	Good	Best
Handling performance	Bad	Medium	Good	Best
Reliability	Highest	High	Medium	High
Dynamic performance	Passive	Passive	Medium	Good
Energy regeneration	Highest	No	No	Yes
Commercial maturity	Yes	Yes	Yes	No

Table 5.1 Comparisons between various vehicle suspensions

5.2. Active suspension system with electromagnetic linear actuators

Electromagnetic linear actuators have several potential advantages for creating forces as compared to pneumatic and hydraulic devices. Because it has a very low static friction, and a current control via the power electronics can be achieved quickly and reliably, so that the strength can be controlled.

The peak power consumption of the electromagnetic damper system is 500 watts. Therefore, check whether such devices can work as stand-alone hardware or require additional power supplies.

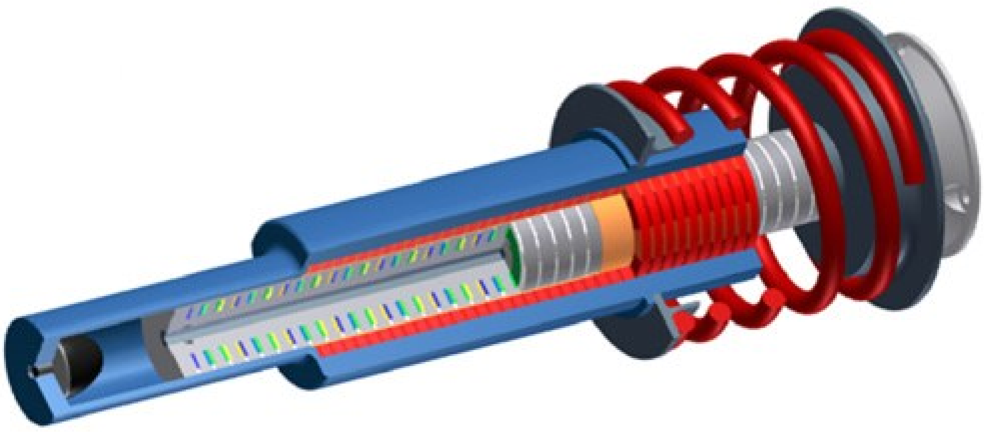

Fig. 5.1. Tubular permanent magnet actuator in parallel with a passive spring

It is shown that a 41% improvement in comfort in the high frequency range of human sensitivity (4-10 Hz) can be achieved, limited by the available motion. Processing can be improved by 31%, which is limited by the available power of the RMS actuator.

5.3. Semi-active suspension system

Over the years, scientists in the world have invented a great deal of new materials, especially in the modern era of nanotechnology. These materials attracts more attention due to their ability to change physical and chemical properties. For engineers it is a big challenge, to introduce these new materials into modern technology. Because today's market wants more energy and resource-efficient and compact technologies.

Smart materials can adaptively change or react to external environmental stimulus. The decisive idea of smart materials can be classified as materials that respond to electric or magnetic field, photon irradiation or ionic strength respectively, in a convenient manner, providing a useful effect. The main parameter, for example, yielding stress, which can be controlled, simply by changing the external condition, can be used to create control forces. Thermally responsive materials have the ability to convert thermal energy into mechanical energy, whereas the remaining ones transform the energy of magnetic stimuli (or other inputs) into mechanical energy.

Magneto or electro sensitive materials include MR fluids or ER fluids that represent smart materials that can change its physical properties between solids and liquids. Electrorheolgical (ER) fluid is one of the smart materials, which changes its flow properties in response to an electric field, while magneto rheological (MR) fluids can be controlled by an external magnetic field. As suspensions of micron-size solid particles in a non-conductive oil, they both undergo a transition from a fluid to a pseudo-solid in the presence of magnetic (MR fluids) or electrical (ER fluids) stimuli.

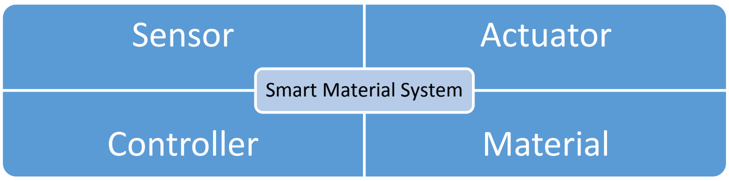

Fig. 5.2 Intelligent (smart) materials

Rabinov (1948) discovered the phenomena of the MR fluids and Winslow (1947) invented ER fluids. Winslow defined the ER phenomenon as changes in the apparent viscosity upon the application of the electric field. Technological hurdles, however, as well as cost prevented the MR materials from commercialization at that time. Apparently, real-time opportunities in vibration damping and isolation were already recognized at that time as the inventors mentioned a method of controlling the damper characteristics through an on-board computer or a microprocessor.

The material that can change its properties in a fraction of a second after changing the operating condition of the system, for a long time attractive to engineers and is of great scientific and technical interest. Short list of other commercial applications includes suspension of racing cars, magnetic valve MR, mountain bike dampers, seismic / bridge dampers, shock absorbers truck seat, optical, absorber washing machines, liquid body armour, prosthetic legs and exoskeletons, haptics, helicopter rotor lag damper, multi-mode motors, cancer therapy, and so on.

In terms of design, the semi-active dampers are based on the concept of either the variable orifice or a smart fluid. The first group is an extension of passive damping systems with continuously variable electromechanical valves, whereas the other varies the damping force output by affecting the apparent viscosity of a smart fluid upon the action of a magnetic (electric) field. MR fluid dampers represent the latter.

Over the years, both materials have received a great deal of attention from the researchers and the industry. From the standpoint of rheology, both MR and ER fluids are equivalent.

5.4. Bingham plastic fluid and Newtonian fluid

The liquid can be divided into two categories: Newtonian and non-Newtonian. Newtonian fluids show a linear dependence with a zero shift between the shear stress and the shear rate. Mineral oil, water and molasses are examples of this category [16].

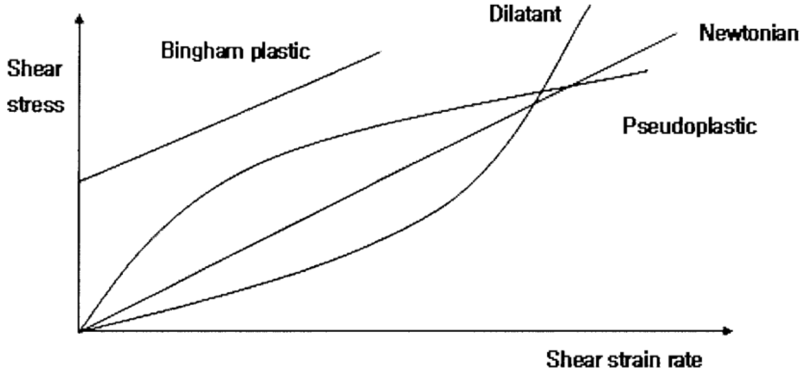

Fig 5.3 The relationship of Newtonian and non-Newtonian fluids between shear stress and shear rate

On the other hand, the non-Newtonian fluid has a different relationship between the shear stress and the strain rate. Pseudo plastic fluids, which are very common, again show a curve starting at the origin and curved up and along, but falling under the straight line of the Newtonian fluid. In other words, the increasing shear rate results in a gradual decrease in the shear stress or dilution viscosity with increasing shear [15].

Based on Bingham plastic fluids, the relationship between shear stress and shear strain rate can be obtained. Under these conditions, the plastic Bingham fluid and the Newtonian fluid can be represented by the following simple power-law formula.

$$\tau = \tau_y + \eta_p(\dot{\gamma})^n \quad (5.1)$$

Shear stress Yield stress + plastic viscosity * (shear strain rate)^n

Where $\tau_y = 0$, n=1: Newtonian Fluid
n≠1: Non-Newtonian Fluid
n > 1: Diltant fluid
n < 1: Pseudo plastic fluid
$\tau_y \neq 0$, n=1: Bingham Fluid ex. Slurry, Wax
n≠1: Non-Bingham Fluid

The homogeneous ER fluids based on an LCP or homogeneous ER medium can not be modeled with a Bingham plastic fluid. Their ER effects are due to a change in their intrinsic viscosity. This allows a so-called differential regulation [10]. The shear stress is nearly proportional to the shear rate, and its slope, viscosity, can be controlled by an electric field. Therefore, it can be easily modeled with a Newtonian fluid, while heterogeneous ER fluids can be described using a Bingham plastic fluid.

6. Magneto rheological fluids

Constructive simplicity and manageability make MR wheels attractive, and they are becoming more popular in industrial applications and in cars. Despite the fact that technological barriers and high costs prevented the development of MR devices, intelligent shock absorbers are located on a number of semi-active suspension systems in passenger cars.

The main advantages of semi-active liquid MR are mechanical simplicity, continuous variation of damping characteristics, high dynamic range (transmission ratio), fast and silent operation, reliability, low power and controllability. Life cycle and temperature requirements for work in cars are similar to conventional shock absorbers. The time of electromechanical valves depends not only on the dynamic properties of the electromagnetic circuit, but also on the magnitude of the force that controls the switching mechanism. In fact, it can be argued that an MR fluid with similar characteristics at medium and high speeds, like other types of controlled equipment, has better dissipation characteristics than all semi-active shock absorbers.

However, the devices remained a problem due to the nonlinearity of the damping force and its dependence on the relative velocities or control inputs. Due to non-linearity, optimal control strategies seem questionable.

Nevertheless, the MR shock absorbers are criticized for their weight and lack of fault tolerance. There are several problems that must constantly take into account the technology, namely: the cost of fluid, precipitation, oxidation of liquid particles, etc. Fault Tolerance is that the damper is capable of providing sufficient forces in the event of a circuit failure. Recently, this requirement has been implemented with several concepts of MR valves. The problem of excess weight can be solved with the help of MR liquids with a lower iron content. Although a lower iron content means lower yield strength (and lower generated forces), it can be compensated for by changes in the geometry of the control valve and the properties of the magnetic circuits.

7. Electro rheological fluids

The mechanism of action of ER liquids cannot be explained by a simple physical theory, since the ER effect occurs for several reasons. The main reason is that the electro rheological (ER) phenomena is caused by the applied electric field. Large changes in viscosity, yield point and short response time lead to various useful technological applications. Unfortunately, the introduction of ER technology is deteriorating due to a lack of understanding of the mechanisms that determine the ER response. However, this cannot fully describe the dominant ER effect of some other materials when organic materials, polymers, carbonaceous materials and fullerenes are suspended. It is believed that other causes, such as water content, diffusion theory and polymer hydrodynamics, also play a role.

.

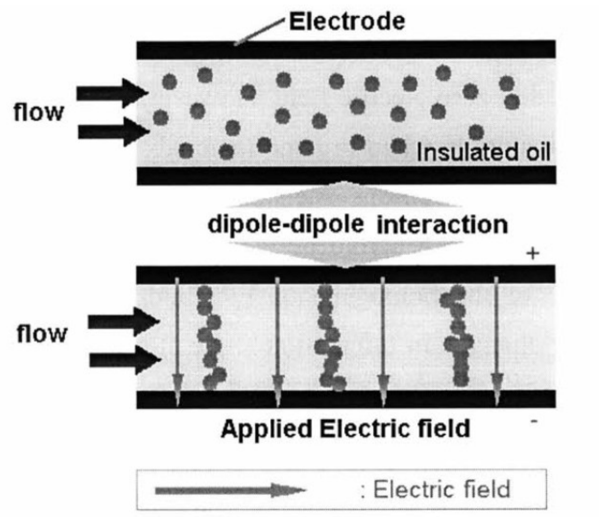

Fig. 7.1 Electro polarization

To describe the hydrodynamic behavior of the ER fluids, an elastic limit and a dimensionless number were introduced. The elastic limit is usually proportional to the square of the strength of the electric field, which is calculated by electrostatic polarization[14]. An independent Mason number was also used to explain the ER fluids. It describes the ratio of viscosity to electrical forces and is given by

$$Mn = \frac{24\pi\varepsilon\mu\dot{\gamma}}{(\beta E)^2} \quad (7.1),$$

Where μ is the viscosity, $\dot{\gamma}$ is the rate of shear deformation, β is the effective polarizability, ε is the permittivity of the solvent [15]. In the case of a Bingham plastic fluid, the shear stress can be expressed by the formula

$$\tau = \tau_0 + \mu\dot{\gamma} = \tau_0(1 + aMn), \qquad (7.2)$$

a is numerical constant ~1 [15].

Homogeneous ER fluids

The homogeneous ER fluid was developed using liquid crystalline polymers (LCP) and has the properties shown in Figure 7.2. Shear force is generated almost in proportion to the cutting speed, the viscosity can be controlled by an electric field. As a result, it is possible to obtain a mechanical control force, which is proportional to the speed in a constant electric field and to perform mechanically, which is equivalent to the so-called differential control. While Bingham fluid can describe heterogeneous ER fluids, a Newtonian fluid can simulate homogeneous ER fluids. Therefore, fluids based on ER particles increase the yield stress with the increase of the electric field.

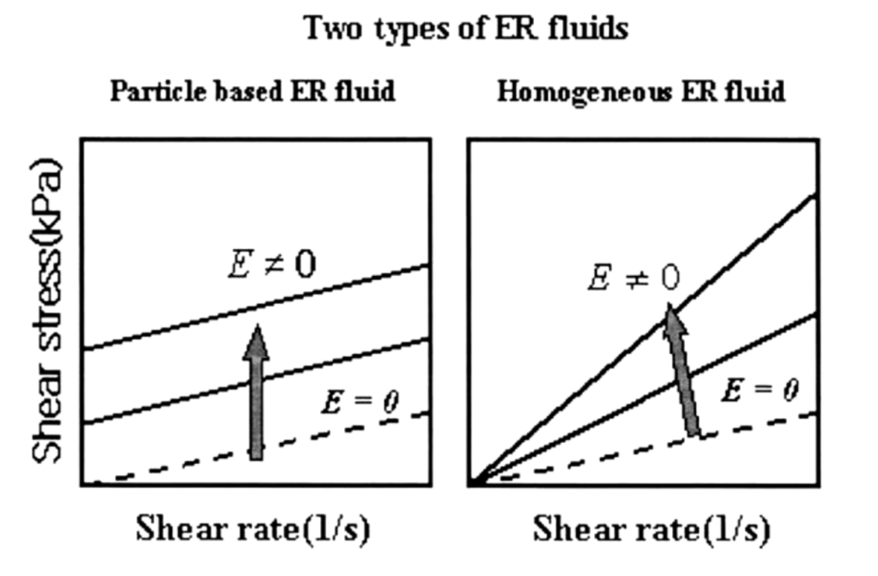

Fig. 7.2 Stress-shear strain rate relationship of two different types

When comparing these two types of ER fluids, homogeneous ER fluids are much better than heterogeneous fluids in terms of shear stress and operating temperature [14]. The following table 7.1 shows the differences between heterogeneous and homogeneous ER fluids. In some cases, shear stress is more than ten times better. [15].

ER fluid type	Heterogeneous	Homogeneous
Rheological behavior	Bingham flow	Newtonian flow
Generated shear stress(Pa) (the shear rate is 300 sec-1 at 2kV/mm)	*600*	*8000*
Viscosity(poise) (Under no electric field)	*1*	*10*
Response(msec)	*<3*	*20-80 (rise)*
Operating Temp. (^{0}C)	*0-60*	*10(or 0)-60*
Current density(μA/cm^2)	*<1*	*1-2*

Table 7.1 ER fluid types

7.1. Three basic motions of ER fluid applications

ER fluids can be used with any of the three main modes or a combination of these: shear or rotation mode, flow or pressure mode, and compression mode. The shear modes may be applied when one plate is fixed and the other plate is moving or rotating, for example a clutch or some smart sandwich spokes, etc. The second mode may describe the movement of the ER flow when the fluid is ER flowing between fixed plates or in a pipe, such as a valve, a motor mount or a shock absorber, are applicable to this movement. The last mode describes the movement of the flow, which is vertical with respect to the movement of the electric field. This mode is useful for explaining the movement of the flow when the flow between the electrical panels is very small [15].

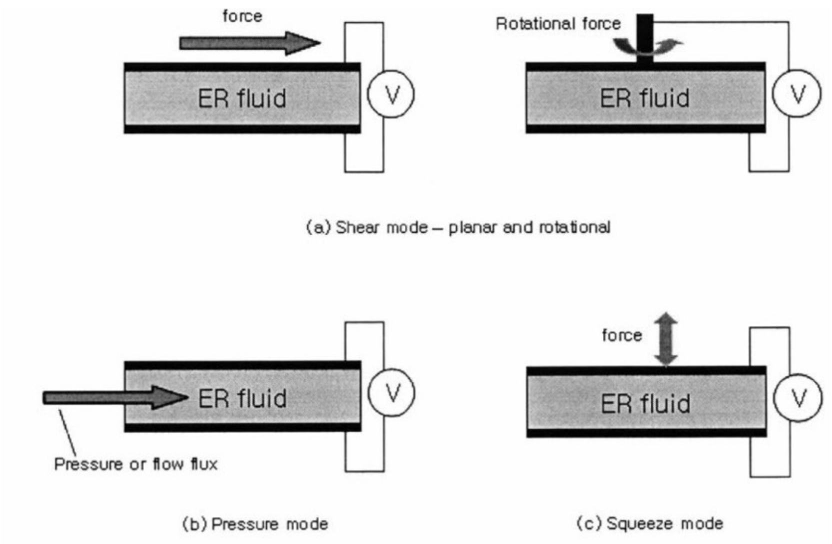

Fig. 7.4 Three basic flow modes

The mathematical modeling of several modes, the following governing equations are needed:
Continuity equation (Mass conservation)

$$\frac{D\rho}{Dt} + \rho\nabla * \vec{V} = 0 \quad (7.4)$$

Navier-Stokes Equation (Momentum conservation)

$$\frac{D\vec{V}}{Dt} = -\frac{1}{\rho}\nabla \mathrm{p} + \vec{g} + \frac{\mu}{\rho}\nabla^2\vec{V} \quad (7.5)$$

The Reynolds number.

$$Re = \frac{\rho U L}{\mu} \qquad (7.6)$$

The effect of gravity is ignored, since the gap between two plates is small enough. If we use these assumptions, we can remove some terms from the N-S equations (see Figure below for coordinates),

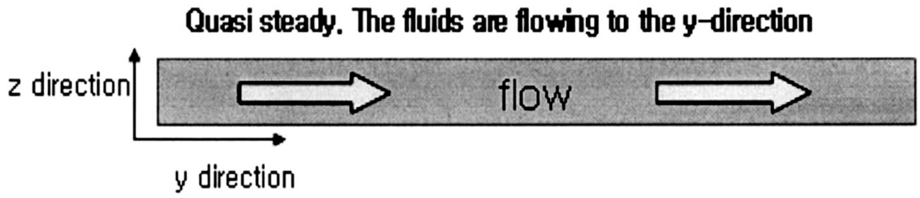

Fig. 7.5 The flow in y-z direction

Therefore, the above equations can be reduced to the followings:

$$0 = -\frac{\partial p}{\partial y} + \mu\frac{\partial^2 v}{\partial y^2};\ 0 = -\frac{\partial p}{\partial z} \qquad (7.7)$$

Simple shear mode

This is the most basic and simplest method among fluid movements of the ER. In the case of a single shear, the pressure drop does not occur, since the force is exerted only in the lateral limits. After considering the relevant restrictions, these can be simplified and the result is:

$$0 = \mu\frac{\partial^2 v}{\partial y^2} \qquad (7.8)$$

with boundary conditions, u(0) = 0 and u(L) = U, and then the velocity profile is

$$u(y) = \frac{U}{L}\,y \qquad (7.9)$$

If this fluid is a Newtonian fluid i.e. in case of the homogeneous ER fluid, the shear stress is

$$u(y) = \mu\frac{U}{L} = const \qquad (7.10)$$

In case of the Bingham plastic fluid, the shear stress will be

$$\tau = \mu\frac{U}{L} + \tau_0 \qquad (7.11)$$

where τ_0 is the yield stress, the velocity profile between the plates should be linear and the shear stress should be constant. If we have also pressure gradient in the shear mode, then the pressure term has to be considered and the results are following:

$$\tau = \mu\frac{U}{L} + \frac{1}{2}\frac{dp}{dx} \qquad (7.12)$$

In case of Bingham fluid, after the whole region was changed to fluid, the yield stress term will be added by τ_0 Therefore, the result is

$$\tau = \mu \frac{U}{L} + \frac{1}{2}\frac{dp}{dx} + \tau_0 \quad (7.13) \quad .$$

Pressure mode

Since the simple cut mode can be easily calculated, the pressure mode analysis can be performed by directly expanding the elementary flow mechanics. Assuming that the flow is a near stable state so that its behavior can be changed so quickly, the behavior of all fluid between two plates can be changed independently of the local area where the flow exists. From (9.17) with the following boundary conditions, u (0) =0 and $\frac{dp}{dx} = 0$, the velocity profile and the shear stress are calculated [15]

$$U(y) = \frac{1}{2\mu}\frac{dp}{dx}(y^2 - Ly) \quad (7.14)$$

$$\tau(y) = \frac{dp}{dx}\left(y - \frac{L}{2}\right) \quad (7.15)$$

The yield stress term will be added by τ_0 and the result is

$$\tau(y) = \frac{dp}{dx}\left(y - \frac{L}{2}\right) + \tau_0 \quad (7.16)$$

8. FEM simulations

In order to study the behavior of ER-fluids in different geometries, finite element simulation is necessary, since experiments with complex geometries cannot be performed. Using FEM software can predict some complex problems. Modeling the behavior of ER, in ADINA, FEM software, used in this work. Most modeling cases were focused on the shear mode of ER-fluids. Although ADINA can solve many complex equations.The following table lists some properties of the two types of fluids used in the experiments [15].

Property	Heterogeneous ER	Homogeneous ER
Components	Carbon-polysilicone Oil	Liquid crystalline polysiloxane diluted in dimethylsilicone
Rheological behavior	Bingham flow	Newtonian flow
Density(kg / m^3)	1100	800
Viscosity(Pa-sec)	0.15	10*
Response time(ms)	<2	20~80
Temperature range(^{0}C)	*-50~150*	0~60
Characteristic stress	Yield stress 4.2kPa at 4kV/mm	Shear stress 8kPa at 2kV/mm with shearrate , 300 (1/sec)

Table 8.1 The characteristic of two types of ER fluids

8.1. FEM modeling

Basically, the size of rectangles is 20µm x 10µm because the thickness of most tested spacer materials are less than 10µm so that 10µm was considered as the average height without any spacer.

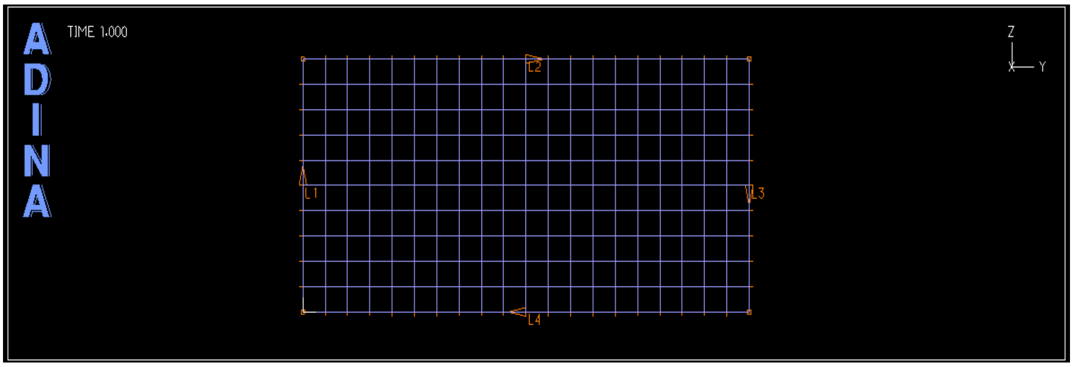

Fig. 8.1 - Dimension of the geometric modeling

As far as the boundary conditions are concerned, all solutions of ordinary or differential partial differential equations depend on their own boundary conditions, so they should be carefully selected. During shear mode simulation, the top plate has only one degree of lateral freedom and the bottom plate is fixed and both sides have the same conditions, as this FEM simulation is considered part of an infinite structure, so that both sides must have the same results. To meet this condition, they may have the same normal tractions (pressure) or pressure gradient, the same velocity profiles or any symmetrical conditions. Under these conditions, the same normal tractions was chosen, since this structure is thin, and the normal force on the upper plate is small, so the pressure gradient is negligible.

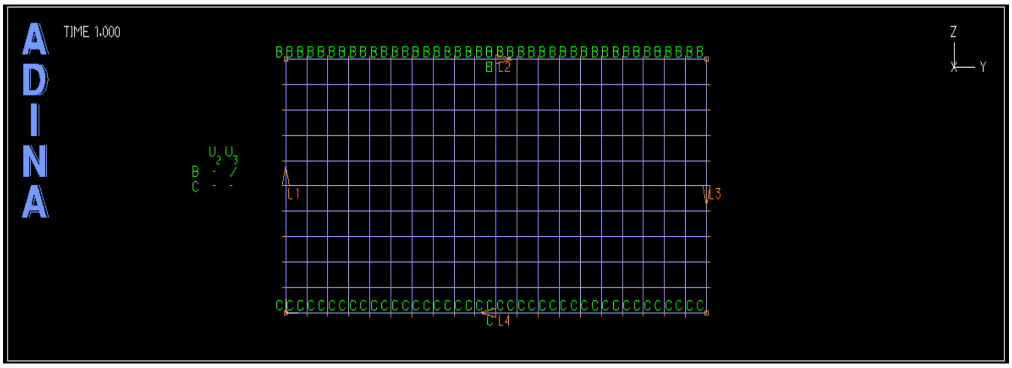

Fig. 8.2 - Illustration of FEM boundary conditions

8.2. Simulation of the Bingham plastic fluid

Most ER fluids can be modeled with a Bingham pseudo plastic fluid. It looks like a rigid body under the yield stress but, it starts to flow like fluid over the yield stress. Unfortunately, the ADINA software distinguishes a solid problem from the fluid problem, and ADINA-F does not have an internal model for it, as are other liquids, such as the Newtonian fluid. ADINA (solid solver module) does not have a model. Although it has a similar model, for example, a viscoelastic model or a geotechnical model (perfectly - plastic model), it cannot show similar results as the expected or unknown properties of ER fluids.

In the case of a viscoelastic model, we do not have information about the constants of the Williams Landel-Ferry equation (WLF), which is used to associate viscosity with temperature. In addition, this module is applicable to our material, whose viscosity is 0.15 Pa-s, ADINA cannot calculate it, and it has some limitations for solving this model. Another very similar model is a geotechnical material based on the Mohr-Column model, which is characterized by a plastic curve with an elastically perfect coating. However, this model simply showed an elastically perfect plastic without any shear rate, and also required other unknown properties. In the case of bilinear plastic modeling, we need a modulus of elasticity and a shear modulus. Our ER material does not have a shear modulus, because it is replaced by a liquid in the yield limit. However, to anticipate this behavior, this model would be useful, since it could show plastic behavior at the yield point, and also show where the shear stress begins to exceed the yield strength.

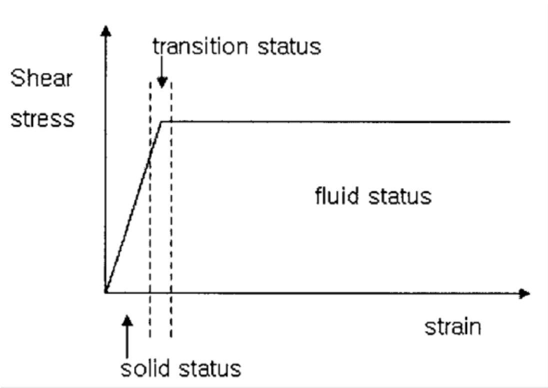

Fig.8.3 - Three different regions of the Bingham material

Figure 8.3 illustrates the mechanical behavior of the Bingham plastic fluid model; there are three different sections. At the yield point, it seems solid, which can be solved by the solid ADINA module. For this, it needs a shear modulus or a modulus of elasticity, and this value can be obtained from an article [15]. This is not the same material we used, but we can use it as rough values. For the sake of simplicity, it was assumed in this work that the material ER is isotropic and elastic in the solid state.

Electric field strength(kV/mm)	1	2	3
Shear yield stress(kPa)	0.3509	0.7214	0.8893
Shear modulus(kPa)	7.5463	16.0744	*18.4305*
Young's modulus(kPa)	20.80	46.34	*55.92*
Poisson ratio	0.378	0.448	*0.517*

Table 8.2 Property parameters of ERM under different electric field intensities [15]

Over the yield stress, the properties of this fluid such as viscosity and shear yield stress can be used. While two regions can be solved by ADINA, the transition region is the mixed state with fluid and solid so that it cannot be explained or simulated. However, because it should satisfy the continuity, we can imagine how fluid starts to develop from solid. In case of shear mode, shear stress is same in the entire region theoretically so that the entire ER material changes its property in millisecond from solid to fluid. Therefore, the transition state is negligible. In case of the pressure mode and squeeze mode both of which have pressure gradient, the shear stress is not uniform so that the transition status should be considered until the whole entire region will be over the shear yield stress [15].

Simple or direct shear mode

In this simulation, the height of the top plate is constant over the areas, while the top plates are not fixed in the experiments. However, with speeds, 8 and 10 mm / s were tested at the electric field 4 (kV / mm).

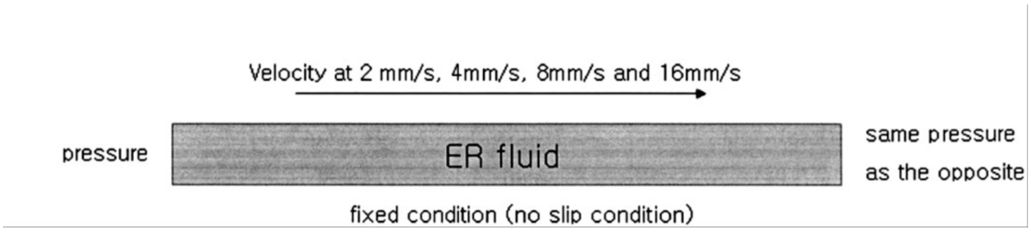

Fig. 8.4 - The boundary conditions of simple shear mode

Simple shear mode with increasing velocity

Two different speeds at 8 and 10 mm / s with an acceleration of 10 mm / s2 were tested at different electric fields (under the same conditions as in the above simulation). To fulfill this condition, a time step was performed in the simulation.

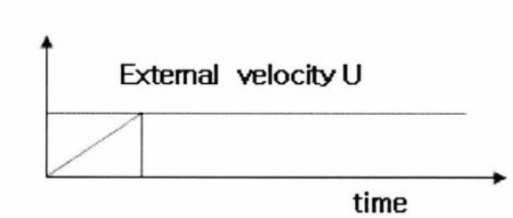

Fig. 8.5 - External velocity profile

Pressure mode between two plates

In order to know where the transitional state begins, the pressure on the left side is increased by 1000 Pa / s. Both plates are fixed and pressure is constant pressure drop plates (-10 (Pa / mm)).

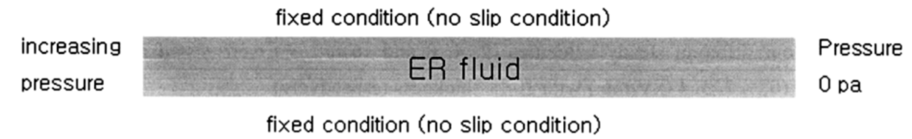

Fig. 8.6 - Boundary conditions in the pressure mode

8.3. Simple or direct shear mode

The simulation shows us the properties of ER liquid at a constant speed (8 mm / s) in an electric field (4 kV / mm). In Figure 8.7, the velocity y is nearly linear and the z-displacement is higher than the ADINA tolerance. The shear stress is not constant and shows in Fig. 8.10 that the maximum shear stress is concentrated in the center of the sample. The pressure differences are insignificant and the values are under the tolerance of ADINA program so that they are negligible.

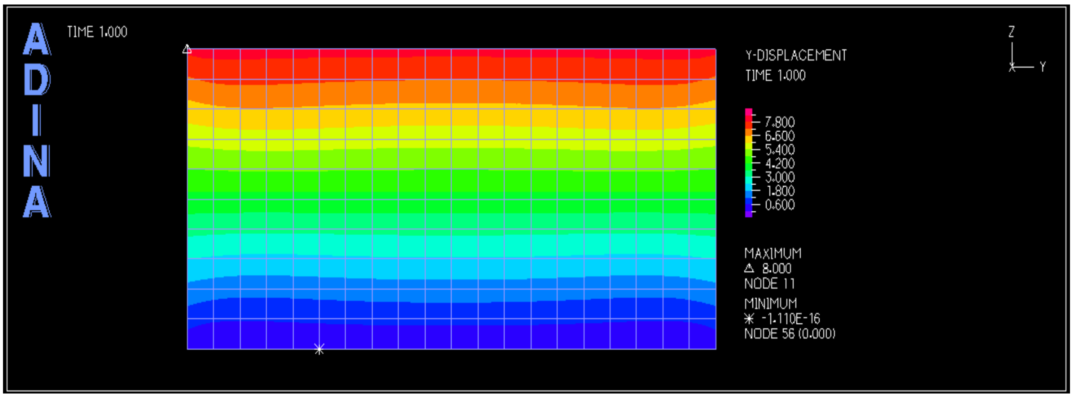

Fig 8.7 **-** y-displacement profile at 8mm/s:

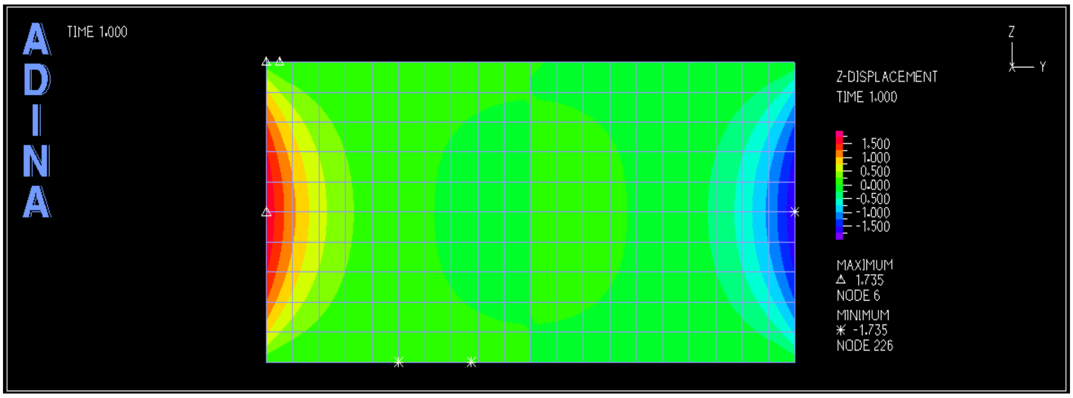

Fig 8.8 **-** z-displacement profile at 8mm/s, z-displacement is over the tolerance of **FEM software.**

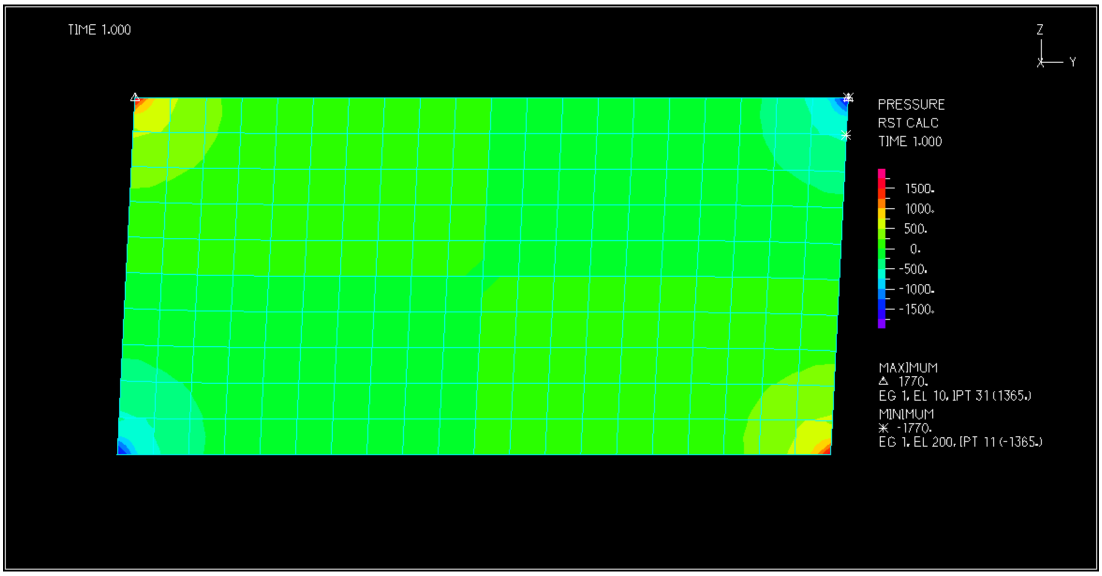

Fig 8.9 **-** The pressure difference is uniform throughout the region

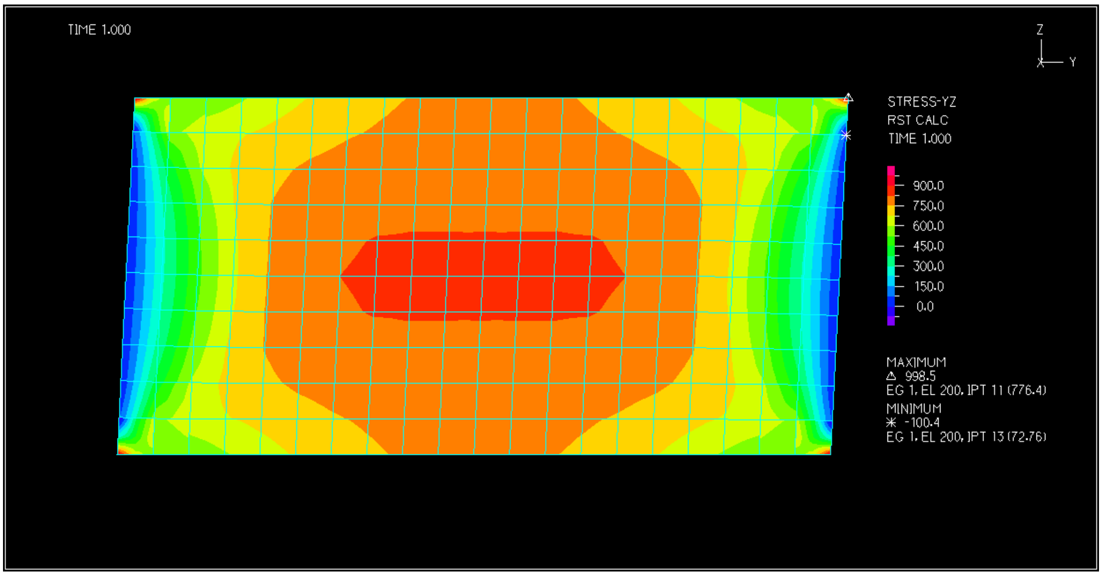

Fig 8.10 - Shear stress gradient

Fig 8.10 shows clearly that the rupture occurs in the middle of nanoparticle's chain. However, further investigation showed that shear stress for long specimens does not have too much gradients and it is uniform throughout the region except endings of the model.

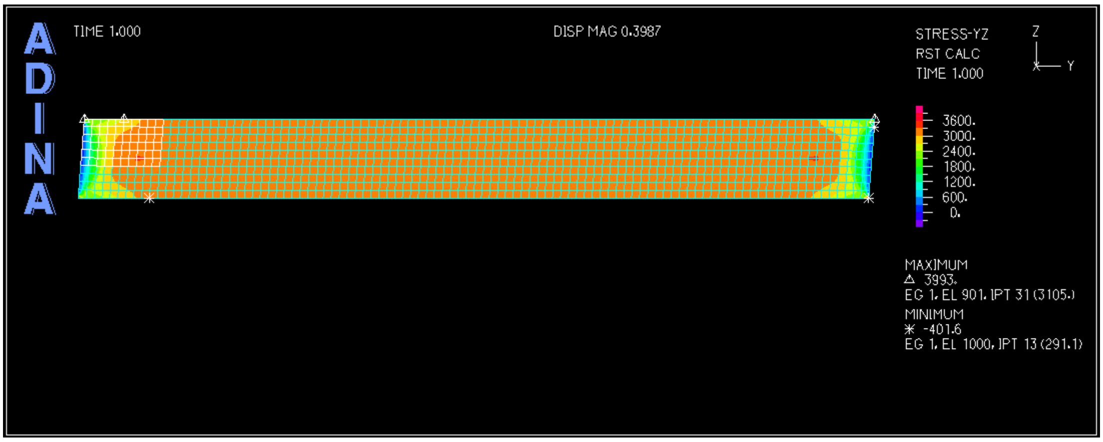

Fig 8.11 - Shear stress gradient for long distance

YY is stress distribution is almost uniform and constant it means that the system under shear force does not have pressure gradient and it is uniform and no pressure fluctuations. However, the reaction forces are different based on location and it is not uniform, so it is clear by designing the surface of the electrodes we can obtain good results of stress and velocity profiles.

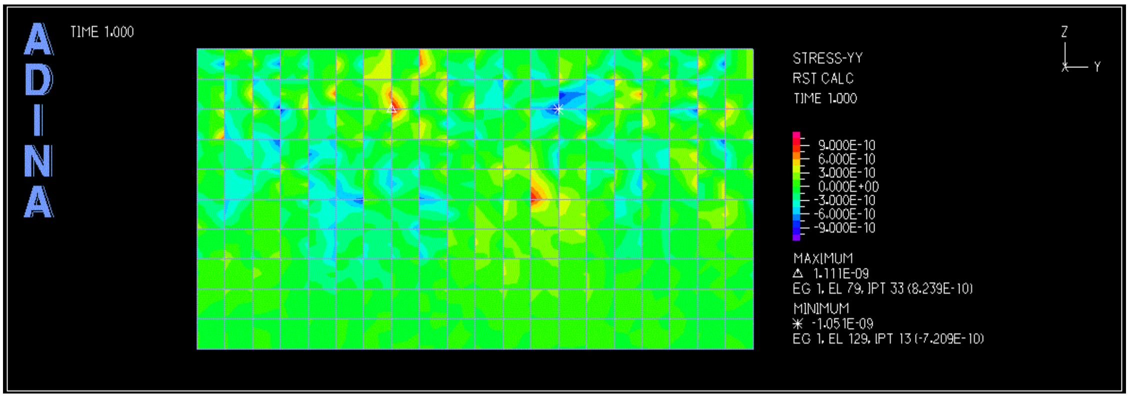

Fig 8.12 - YY stress gradient

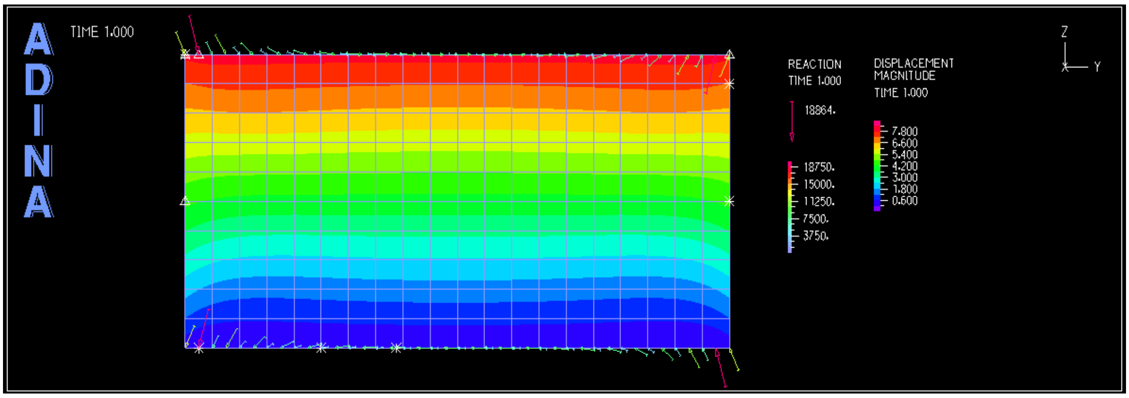

Fig. 8.13 Stress distribution and reaction forces.

Fig. 8.13 gives a quick overview of the system with the reaction forces. The maximum reaction force is about 19kN at the ends of the model and it is almost at the z direction, but in the middle part of the specimen reaction forces are y directional.

8.4. Simple shear mode with increasing velocity

The Y-velocity can be checked if it has grown linearly or not (see Figure 8.14). After that, the speed profiles throughout the region remain almost constant. From the theory of electrostatic polarization, the yield stress is proportional to the square of the electric field strength and because the shear strength is 0 Pa at 0 V and 4.2 kPa at 4 kV,

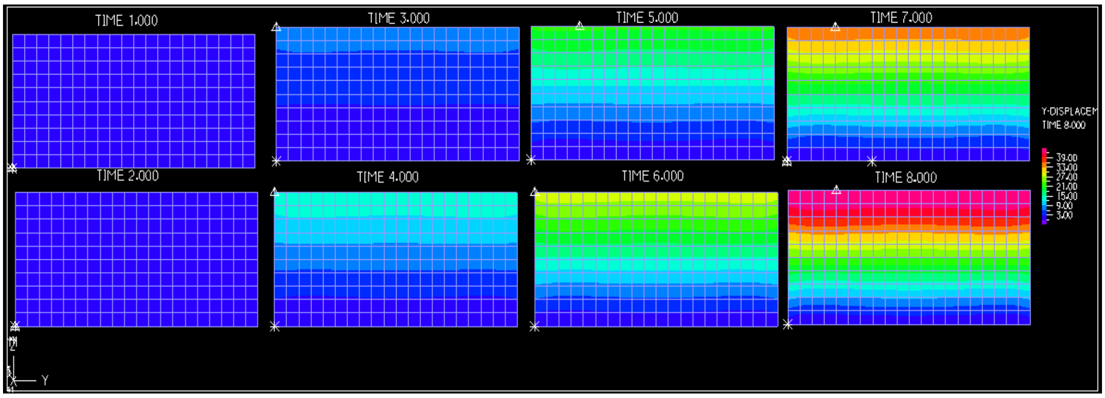

Fig 8.14- y-velocity profile from zero to 8 seconds with the increasing velocity up to 8mm/s.

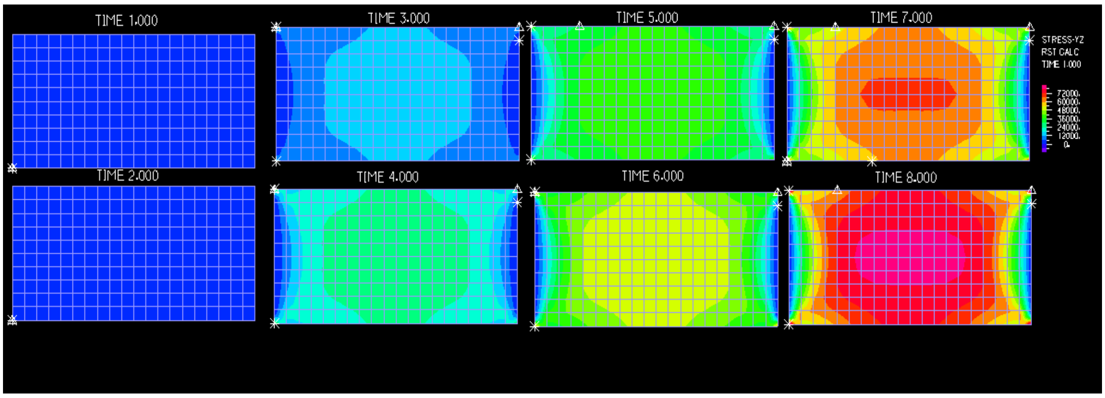

Fig 8.15- Pressure distribution with the increasing velocity

In the case of a solid under the external shear, the shear stress would be uniform and constant over the entire area. Thus, the shear stress in the entire region simultaneously reaches the yield stress point and then it can start to flow. Assuming that the total shear stress is the sum of the yield stress of the solid and the shear stress of the fluid, the Bingham plastic fluid should exhibit this behavior. On the other hand, in the case of a homogeneous ER fluid, the relationship between the shear stress and the shear strain rate should be linear, and the slope should be changed by the external electric field strength. The value of the viscosity of the homogeneous ER liquid was taken from [15], in which the same material was tested. The shear stress stresses of heterogeneous ER fluid were calculated by electrostatic polarization theory, which indicates that the shear strain stress is proportional to the square of the electric field strength.

8.5. Pressure mode between two plates

The shear stress distribution and the velocity profile were tested when the external pressure on the left side was applied to ER fluid between two plates. In this case, there exists a pressure gradient, so that the velocity profile is not linear, it is parabolic and symmetric. Its velocity profile, YZ-stress at 4 kV / mm are shown in Figure 8.16 and Figure 8.17.

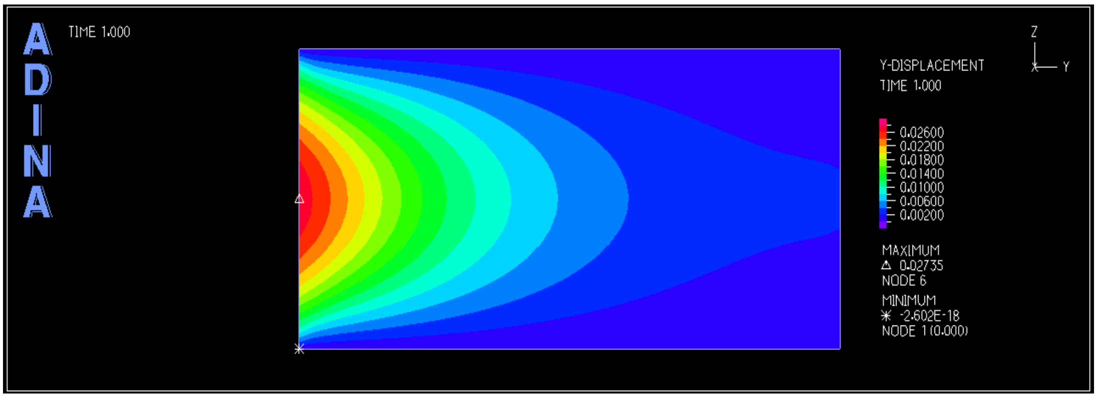

Fig 8.16 - y-velocity profile

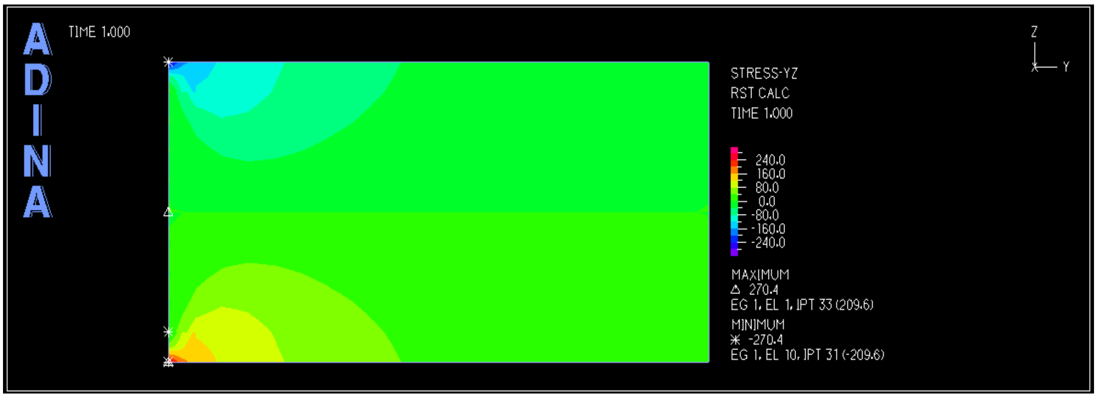

Fig 8.17 - Shear stress

Figure 8.18 explains how the shear stress develops and where the shear stress first reaches the yield point. To simulate this, the external pressure on the left side was increased by 1000 Pa / s. In this simulation, the time interval can indicate where the shear stress increases. Time interval, 1 s. However, he was chosen so that time would not make sense. The maximum shear stress is below the shear stress of the material.

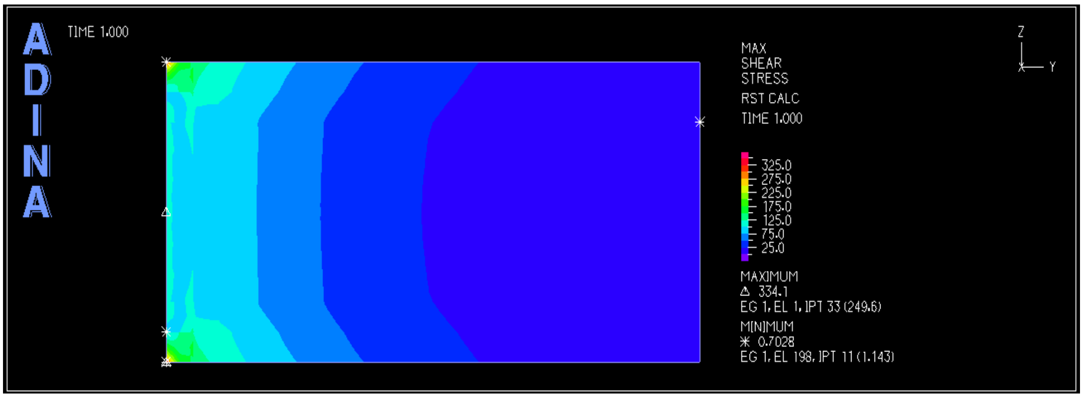

Fig. 8.18 The shear stress distribution

From the figure 8.19, the effect of the external pressure was propagated because the young's modulus is so small that the pressure couldn't affect the whole region in milliseconds. When the fluid changes to liquid form, the properties of ER behavior are same as the Newtonian fluid. The velocity profile is parabolic and the velocity is max at the center. The shear stress, like the solid, at the upper and lower line, had the maximum values.

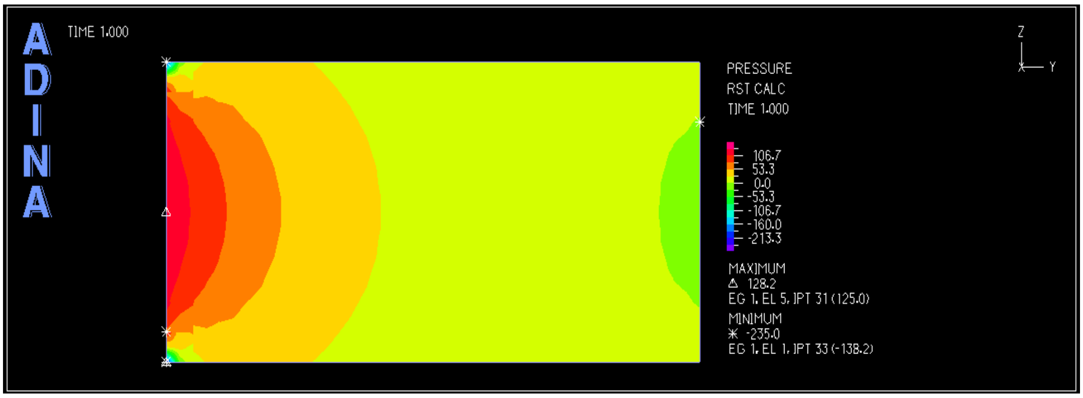

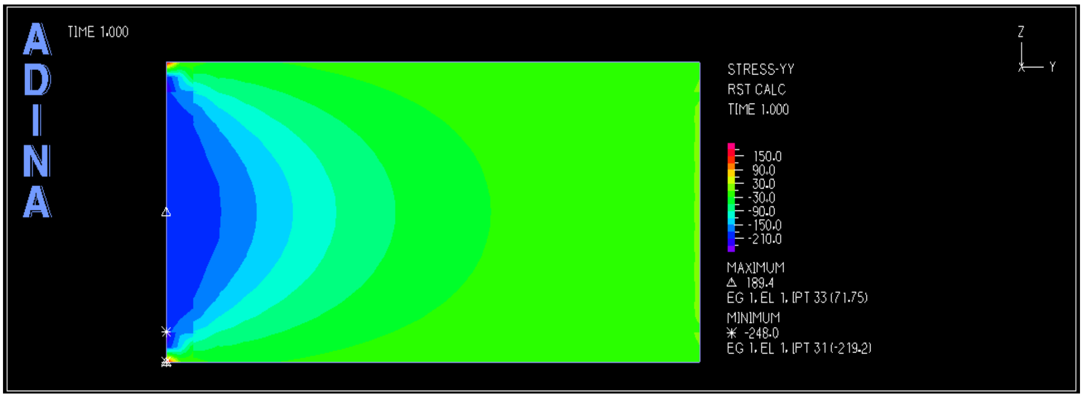

Fig 8.19 - The pressure and YY-stress of the solid region of Bingham plastic fluid

However, the correct design of the surfaces of the electrodes makes it possible to improve the propagation of pressure. Because high shear stresses at the boundaries tells us, the rupture of the ER-fluid will be at the boundaries, so after this situation the slurry mixture of ER-fluid starts to travel. If we improve the design of the ER-fluid valve by changing the electrode shapes, for example wriggle ER-fluid travel line or multi-layer electrodes will gradually increase efficiency.

8.6. Implementation of the results in a new design

Finally, we have results from 2D simulations that can used for preliminary design of the ER-fluid valve. Since the main factor of the damping characteristics of ER valve is surface area. The large surface area has more capability to hold the system with high force. Moreover, ER-fluid under electrostatic field becomes pseudo-plastic form and when this kind of slurry mixture moves through the small cross section, it creates a huge reaction force, if the distance of the displacement increases by reducing flow rate we can achieve very high resultant force.

For example, a segment shown in Fig.8.20 is 3D version of the ER fluid simulation under uniform external pressure. ZZ- stress of the segment almost uniform and the external pressure is acting with magnitude 0.1 (force/area) and if the cross section of the segment is equals 1 mm^2 which gives us 1bar.

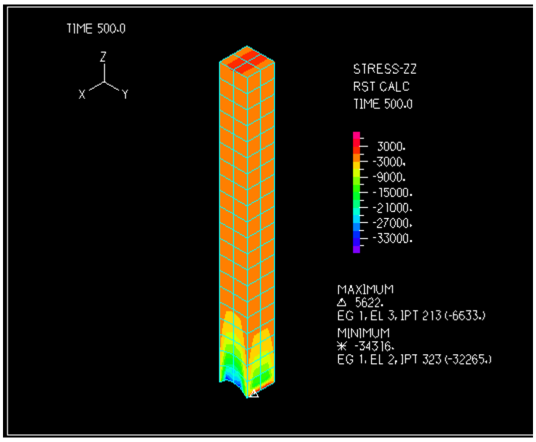

Fig 8.20. 3D simulation of pressure mode.

Furthermore, a multi-duct sigment was created. In this case all ducts are in parallel and flow in each duct is different, since cross sections are different. The total flow rate is the sum of the flow rates along each duct. Fig. 8.20 shows that the total pressure is same in each duct. The total cross section of the ER-valve has much attention, because by increasing the area of the section we can hold more force.

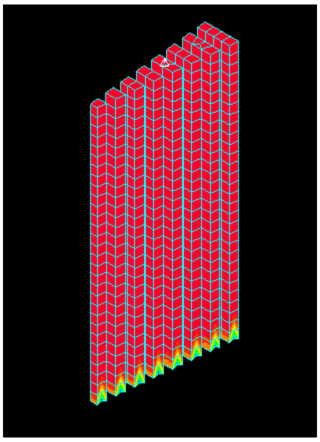

Fig 8.21. Multi-duct

Hypothetically, multi duct ER valve can operate in the range from 2kN to 10kN. All experimental data are evaluated and compared with existing ER-valves. After several simulations, the general characteristics of the multi-duct ER-valve was obtained and it was used to design a new type of shock absorber. The idea is simple and can be implemented in the complex systems by discretizing the volume. Because the pressure is same for every segment and the acting force equals to the sum of the segment forces. Since the pressure is the same for each segment, and the acting force is equal to the sum of the forces of the segment. The controllable mechanical power has dependence to the yield stress of the ER fluid and the total area of the electrodes.

Current Draw	0.13 Amp/m^2
Viscosity	0.035 Pa*sec
Yield stress	5kPa
Dynamic range	10 (at 50cm/sec)
Flow gap	1.6 mm
Electrical	C=0.001-0.050 µF
Field limited by	Dielectric break-down
Response time	0.1-10 ms
Power supply current	0.3 Amp(peak) 0.001-0.250 Amp (continuous)
Power supply voltage	6400 volt

Table 8.3. Electro-mechanical parameters of the ER fluid.

In the table 8.3 was shown a yielding stress of the ER fluid that is 5kPa and in the all simulations the maximum stress was not exceeded materials yielding stress.

In ordinary electrorheological (ER) fluids, the shear stress induced in the field is associated with the interaction of polarized particles aligned in an electric field. The physical mechanism of ER-liquid dielectrics is well established, and the upper limit of the yield point, predicted by the traditional dielectric theory, is approximately 10 kPa. The low creep resistance of conventional conventional ER liquids, usually small kPa, has blocked their use in the past half century. By adding some polar molecules to the particles, in recent years a series of highly effective ER-liquids have been obtained that show the giant effect of ER. In Fig. 8.21 shows the dependence of the elastic limit in an electric field for ER-fluids consisting of TiO2 nanoparticles with molecules (NH2) 2CO and polar groups C = O, OH, as well as Ca-Ti nanoparticles. Or with C = O, O - H, respectively [17].

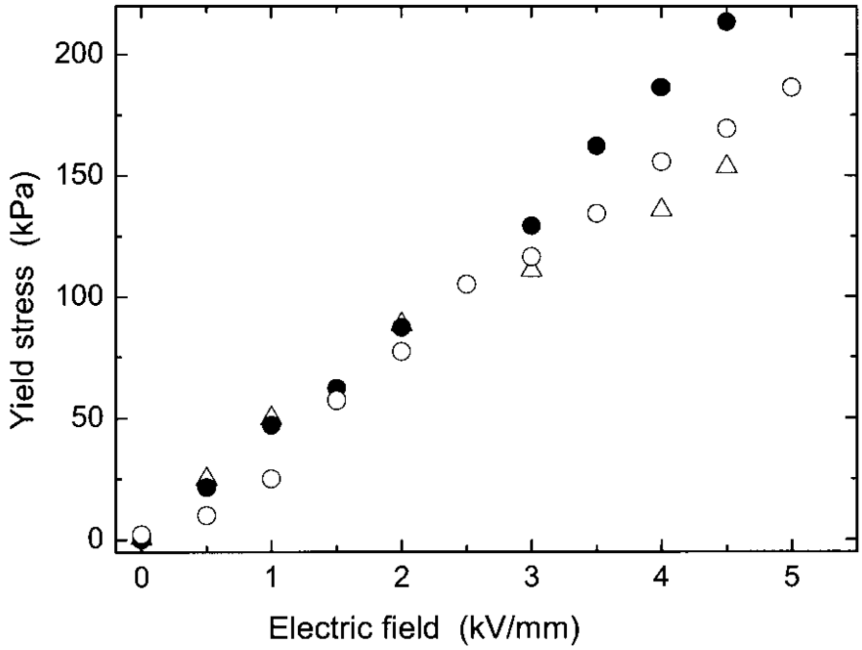

Fig 8.22 Yield stress versus electric field of some ER fluids. Dots: TiO_2 nano-particles with $(NH_2)_2CO$ contained; Circles: Ca-Ti-O nano-particles with C=O, O-H groups contained; Triangles: TiO_2 nano-particles with C=O, O-H groups contained.

All the particles have a sphered shape with diameter of 50-100 nm and were suspended in silicone oil with volume fractions about 35%. The yield stresses of the ER fluids were measured with a special designed flat shearing apparatus. The yield stresses of those new ER fluids can reach up to 200 kPa, much higher than that of foregone ones, and behave a near linear dependence on electric field unlike the quadratic one in ordinary ER fluids. The current densities are less than 20 µA/cm2 for TiO2 nanoparticle ER fluids and even less than 1 µA/cm2 for Ca-Ti-O nano-particle ER fluid at 5 kV/mm [17].

The device has three ER valves, two of them at the top and bottom and one long connecting valve and all of them with multiple ducts. The effect of the multiple ducts improves a performance of the shock absorber and provides an outstanding dynamic range and force level, since the total area of the electrodes is high, which allows to use it with high pressure, simultaneously with high force.

Fig 8.23. – Electro rheological shock absorber with multiple ducts

This preliminary model was created in order to learn basic principles of the multi duct electro rheological suspension system and FEM simulation. In order to reduce the weight of shock absorber aluminum alloyed electrodes were used, and the thickness of the electrodes is about 1.5mm. The gap between two electrodes minimum 50µm maximum 1.6mm. Fig.8.23 shows the distance between electrodes, which is 0.5mm and a bore through electrodes connects the upper valve to the long valve.

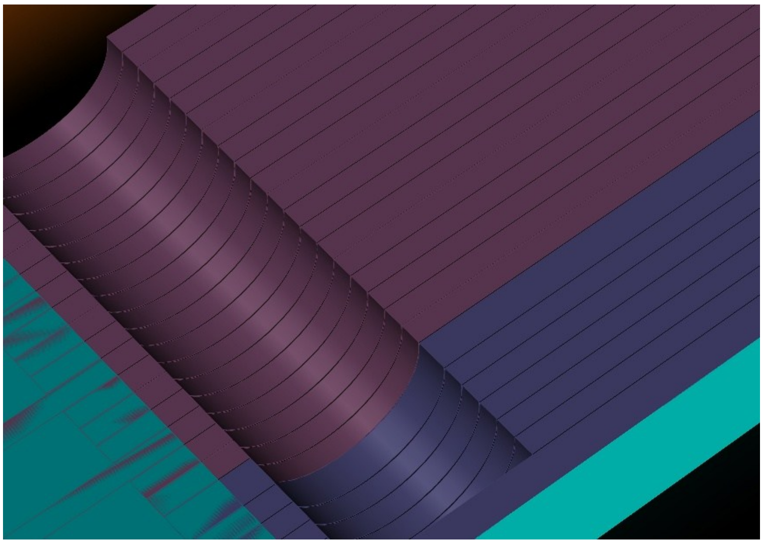

Fig 8.24. The electrodes with 0.5mm distance between electrodes

The main cylinder is made of steel with thickness 2mm because it should be more wear resistive. Meanwhile, the piston is made of insulator type of material to prevent from electrical breakdown and short circuit. Shock absorber travel is 150mm.

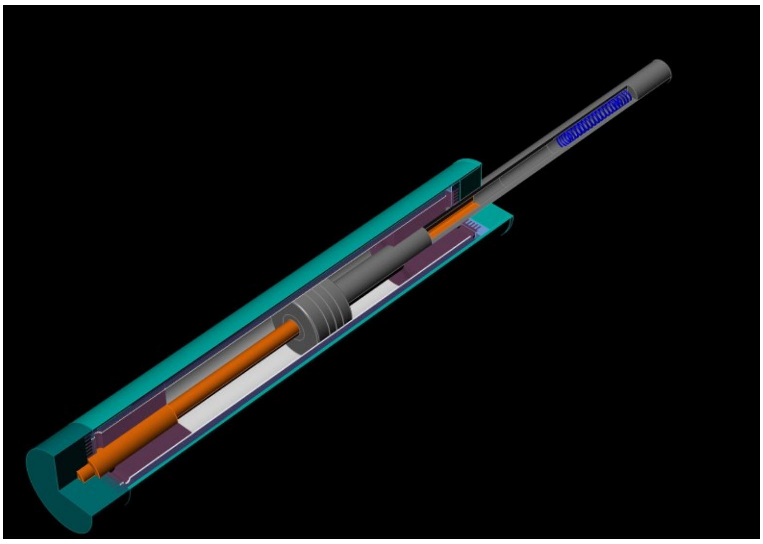

Fig 8.25. Suspension system with section cut

Figures 8.25 and 8.26 show that in this model two steel bars were used the bar with bigger diameter has a bore with same diameter as a second bar, which is entered into the bore, and the main goal is to keep axisymmetric displacement with high precision. The spring inside the bore is used to reduce mechanical shock and to prevent from contact between piston and upper electrodes.

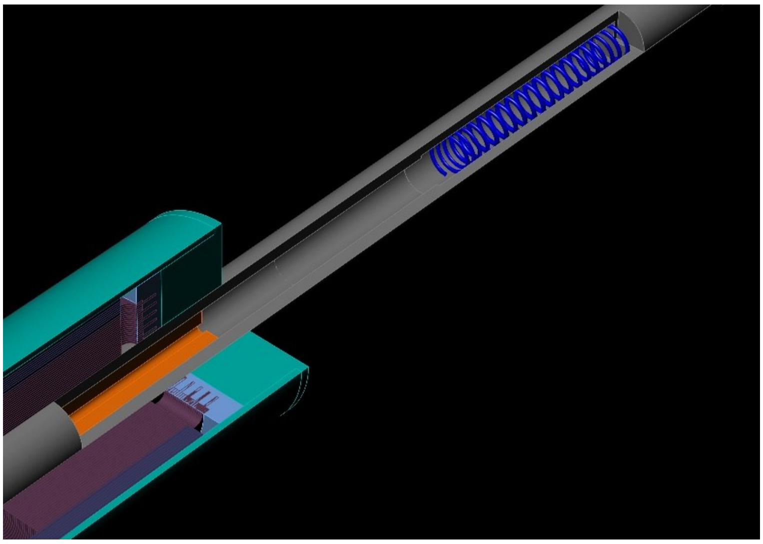

Fig 8.26. The bottom part of the shock absorber

The second bar also has a small bore to permit a fluid inside to move. That allows to avoid the heating of internal parts. However, it will increase internal friction force. Assuming that all the dissipated mechanical energy is transferred to heat and it will increase in temperature per fluid cycle within the ducts can reach 1 to 1.5 degrees Celsius per cycle.

A design method for controllable damping devices with ER fluid was numerically verified with several simulations. In the end, a new shock absorber model with a set of annular ducta was designed, concentric metal tubes that also serve as electrodes, provide both large areas of surface over which the ER fluid flows at low speed and large volumes of ER material exposed high electric field (3 kV / mm).

9. Semi-active control methods

The dynamic model of the car suspension system is complex and not suitable for the formulation of the controller. The model of concentrated mass parameters does not represent sufficiently dynamic behavior of the vehicle. The actual behavior of the suspension system in a vehicle has significant nonlinearity, some uncertainty, a time delay, and even a driving or system failure. Once these complex factors are taken into account, the task of improving ride comfort and getting the road becomes more complex than ever. Therefore, the design studies for control in intelligent suspension systems received much attention.

The non-linearity comes mainly from the suspension system or the drive itself. The cancellation of non-linearity includes non-linear coefficients of spring or damping of the coefficients, non-linear frictional force between the elements, nonlinear geometric constraints. The dynamic behavior of typically non-linear actuators and works in severe conditions for a long time. During operation, some elements such as sensors, settings, and the actuator in the system will not work properly. If errors in these elements are not corrected in time, the system may not deliver the desired performance or even lose stability.

An intellectual structure of the suspension phase, such as skyhook and groundhook control methods, are often regarded as semi-active suspensions for vehicles and are usually intended for two stages of freedom. However we are wil consider a hybrid control method, which seeks to combine the benefits of skyhook ground hook controlling. [12]

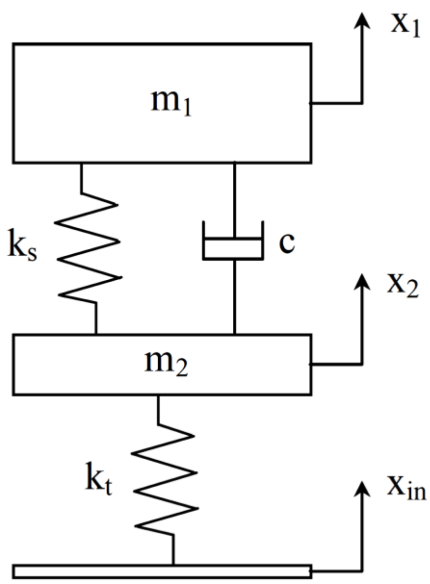

Fig. 9.1 - 2DOF Quarter-Car Model.

The skyhook controls suspended or sprung body, in contrast ground hook control controls the unsprung mass. An alternative semi-active control policy known as hybrid control has been shown to take advantage of the benefits of both skyhook and ground hook control. Since the model represents a single suspension, which is often, referred to as the “quarter-car” model.

m_1	mass of the vehicle body (sprung mass)
m_2	tire/axle assembly (unsprung mass),
x_1	displacement of the sprung mass
x_2,	displacement of the unsprung mass
v_1	velocity of the sprung mass
v_2,	velocity of the unsprung mass
v_{12}	relative velocity
k_s	spring element
c.	damper,
k_t.	tire stiffness

The semi-active damping force of the skyhook control is defined as

$$\begin{cases} v_1 v_{12} \geq 0 & F_{sa} = c_{sky} v_1 \\ v_1 v_{12} < 0 & F_{sa} = 0 \end{cases} \qquad (9.1)$$

where,
v_1 = Absolute velocity of the sprung mass
v_{12} = Relative velocity across the suspension
F_{sa} = Semi-active damping force
c_{sky} = Skyhook damping coefficient (gain)

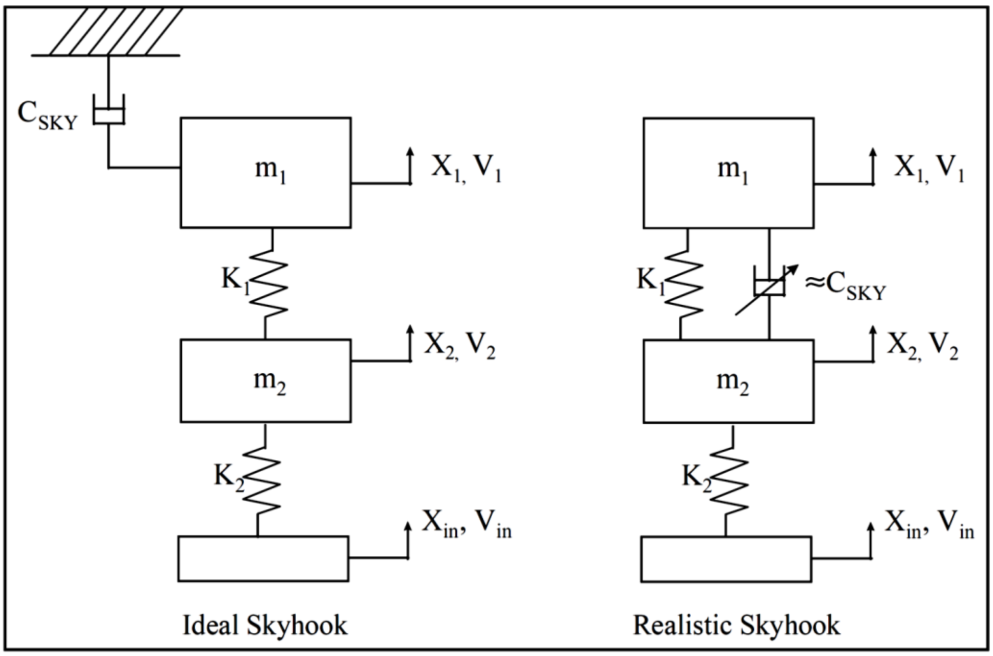

Fig. 9.2 - The skyhook damper model

Disadvantage of the skyhook damper, it removes the energy from m_1, the motion of m_2 becomes excessive because no damping is applied to it. Of course, in the realistic system, the semiactive damper will still remove some of the energy from m2, since the semi active damper is mounted between the two masses. In vehicle suspensions, this problem is known as wheel hop, and can cause excessive axle (mass 2) bounce and loss of contact with the road surface.

Now consider the case where we move the skyhook damper to mass 2, as shown in Fig. 9.2 This is known as the ground hook configuration, since we are attempting to "hook" the second mass to the ground. The equation governing ground hook control can be expressed as

$$\begin{cases} -v_2 v_{12} \geq 0 & F_{sa} = c_{gnd} v_2 \\ -v_2 v_{12} < 0 & F_{sa} = 0 \end{cases} \qquad (9.2)$$

where,
$v_2 =$ Absolute velocity of the unsprung mass
c_{gnd} = Groundhook damping coefficient (gain)

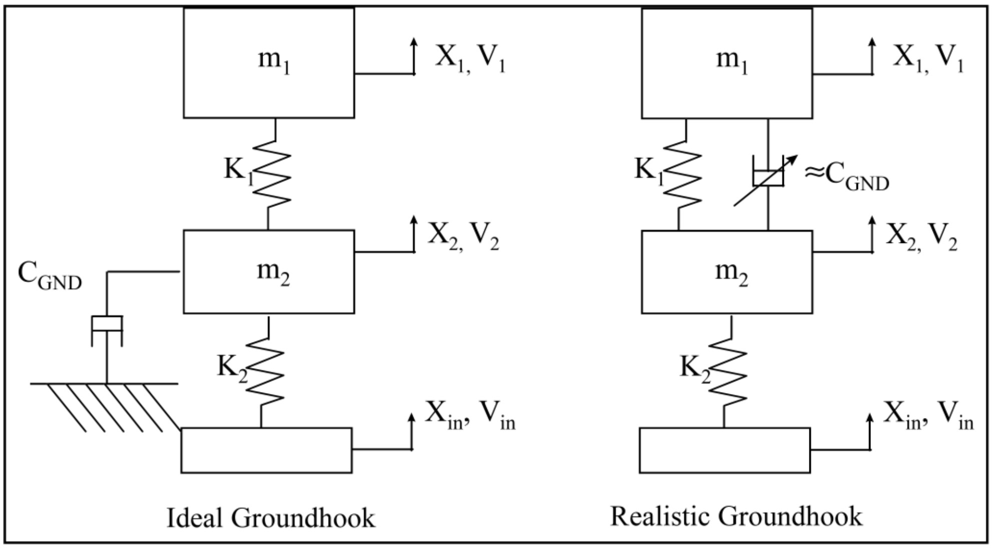

Fig. 9.3 - Ground hook Formulation for the 2DOF System.

The problem with ground hook damping is that the motion of m_1 becomes undamped. However, as in the skyhook case, this will not truly happen since there is some residual damping between m_1 and m_2 due to the off state and location of the damper.

The skyhook control policy minimizes sprung mass motion (or vehicle body motion for a primary suspension) at the cost of wheel motion, whereas ground hook control minimizes wheel motion at the expense of body motion. We would like to take advantage of the desirable aspects of each control policy and choose a more suitable compromise for a given application. This is the fundamental idea of hybrid control, shown in Fig. 9.3.

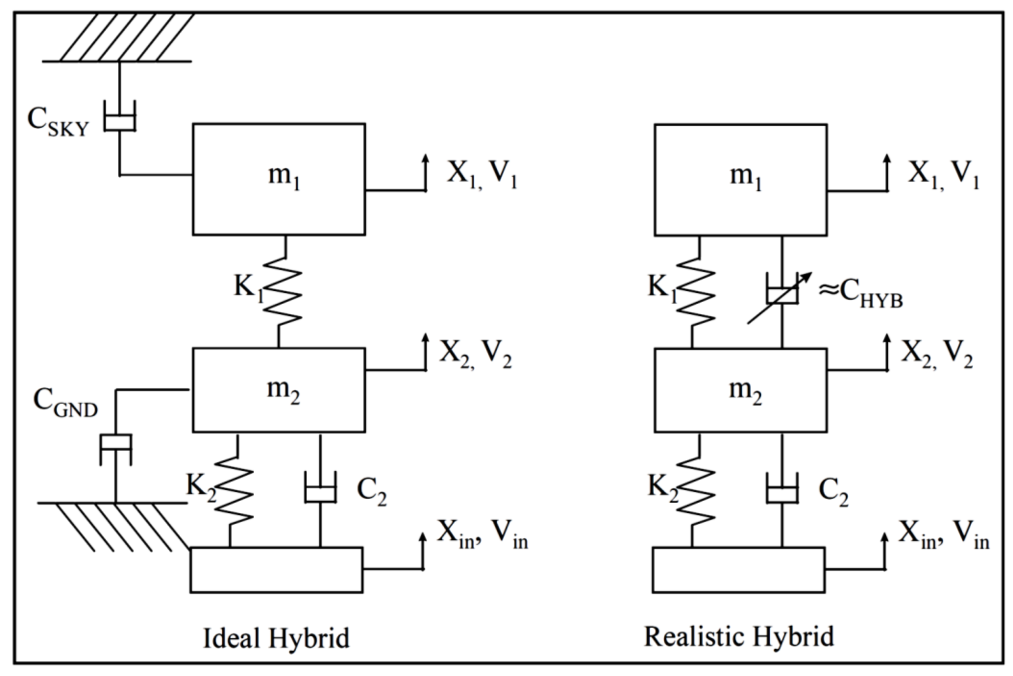

Fig. 9.4. Hybrid Control.

With hybrid control, the user has the ability to specify how closely the controller emulates skyhook or ground hook. In other words, hybrid control can divert the damping energy to the bodies in a manner that eliminates the compromise that is inherent in passive dampers. Combining the equations, we arrive at the semi-active hybrid control policy:

$$\begin{cases} v_1 v_{12} \geq 0 & \sigma_{sky} = v_1 \\ v_1 v_{12} < 0 & F_{sa} = 0 \end{cases}$$
$$F_{sa} = G\left[\alpha\sigma_{sky} + (1-\alpha)\sigma_{gnd}\right] \qquad (9.3)$$
$$\begin{cases} -v_2 v_{12} \geq 0 & \sigma_{gnd} = v_2 \\ -v_2 v_{12} < 0 & F_{sa} = 0 \end{cases}$$

Where σ_{sky} and $\sigma_{gnd}$are the skyhook and groundhook components of the damping force. The variable α is the relative ratio between the skyhook and ground hook control, and G is a constant gain. Consider the case when α is 1; the control policy reduces to pure skyhook. When α is 0, the control is purely ground hook.

To practically implement hybrid control, we need to know v_1,v_2 and the relative velocity v_{12}. For ease of application in a research environment (i.e., proof of concept), we will measure v_1, and $v_2$using an accelerometer and analog integrator exactly as the skyhook controller measures v_1. The relative velocity, v_{12} is then computed using the difference between $v_1$and v_2. Figure 9.4 shows a block diagram representation of the hybrid controller, while Fig. 9.5 shows the SIMULINK code for the hybrid controller.

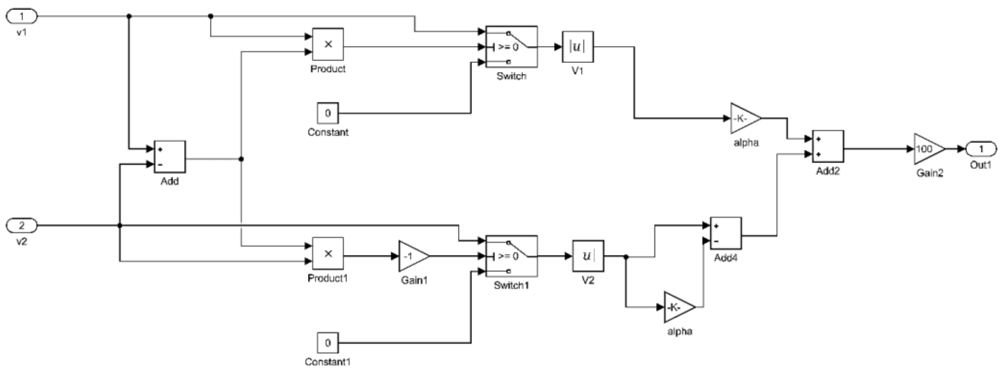

Fig. 9.5 SIMULINK Code for the Hybrid Controller.

The hybrid control showed advantages for both bodies. The trade-off between a clean Skyhook and a clean ground hook can be introduced by a hybrid control. The steady state results show that hybrid control can be used to reduce the shifts and accelerations of both bodies from peak to peak. Even with and α of 0.5, reduces both responses of sprung and unsprung masses to a passive response. This means that profits can be achieved by using equal contributions from skyhook and groundhook. Evaluation of the transient process shows that hybrid control can be effective in reducing the peak-peak offset in the adjacent direction. However, hybrid control does not greatly affect the acceleration of the peak to the peak. In many cases, the acceleration of the hybrid accelerated mass peak is greater than that of the passive one. However, accelerated mass acceleration can be reduced by hybrid control. Continuous acceleration from peak to peak is less than in passive hybrid control.

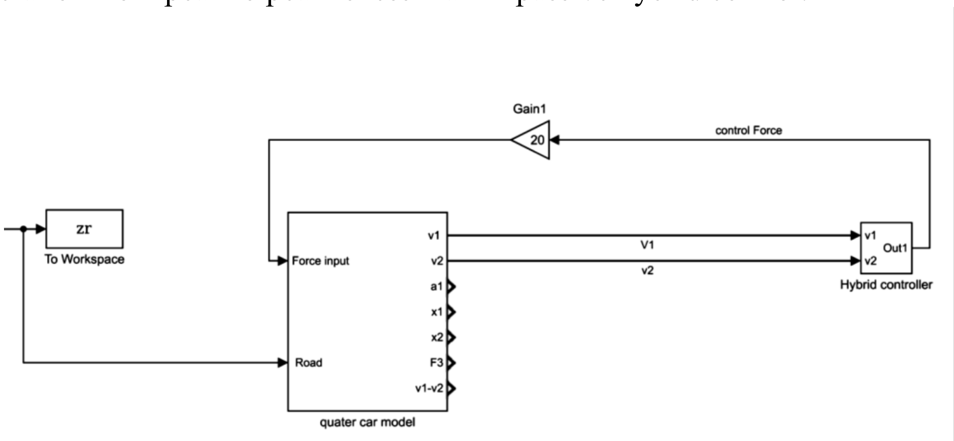

Fig. 9.6 - SIMULINK Code for the quarter car model with hybrid controller.

The automobile is traveling over a rough road at a constant horizontal speed when it encounters a bump in the road of the shape shown in Fig. 9.7 in green line, a brown line represents suspension travel meanwhile a blue line shows how suspended mass response for the bump.

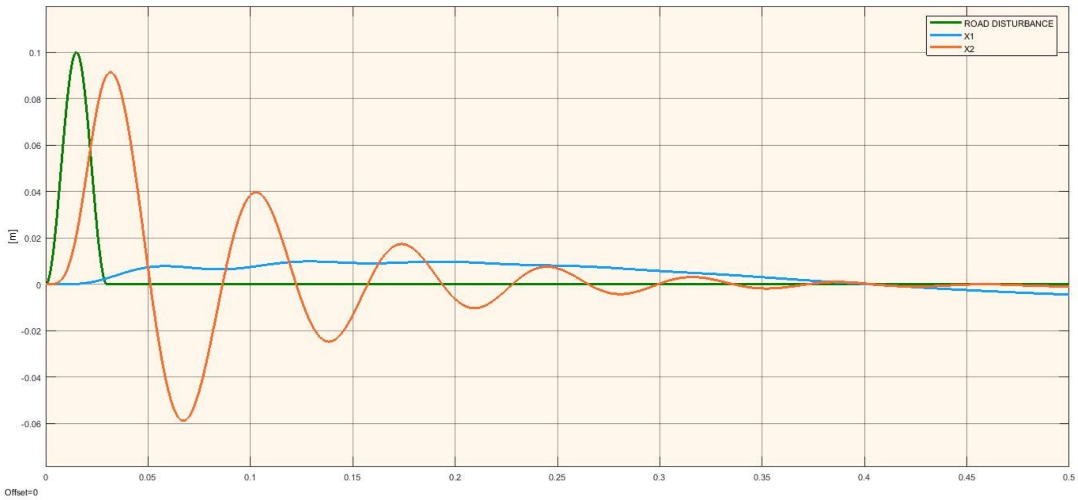

Fig. 9.7 The suspension system under control of hybrid controller.

The figure below shows a difference between suspension with the hybrid controller and without. It is easy to differ by counting amount of peaks.

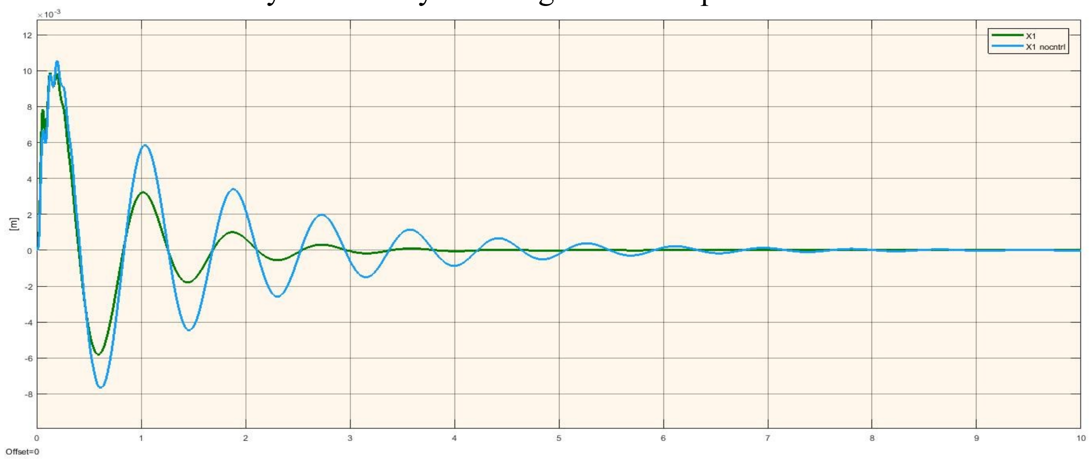

Fig. 9.8. The suspension system with and without the controller

In order to check the response for the random road excitation, I used road simulator in SIMULINK, and the result is given Fig. 9.9.

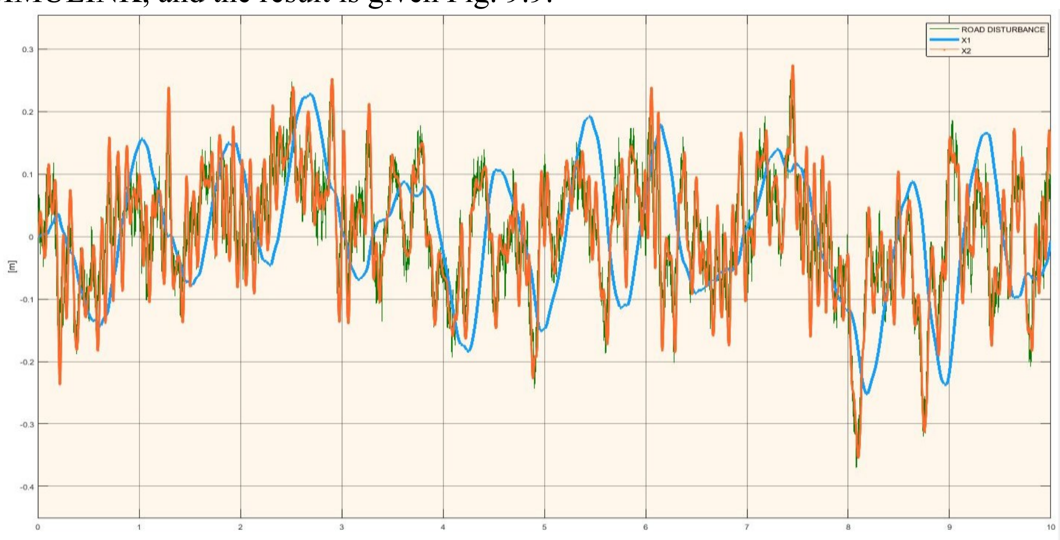

Fig. 9.9 The response of the suspended mass to the random road excitation

The other necessary information about the suspension model with controller can be found below in Fig. 9.10, the velocities of suspended and non-suspended masses together with suspension travel velocity and control force.

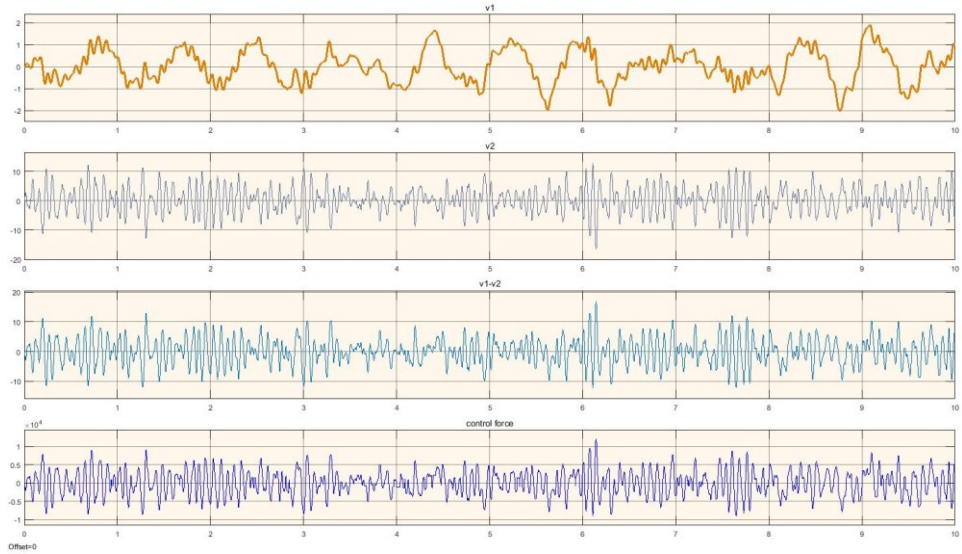

Fig. 9.10 - Velocities of suspended, non-suspended masses and control force.

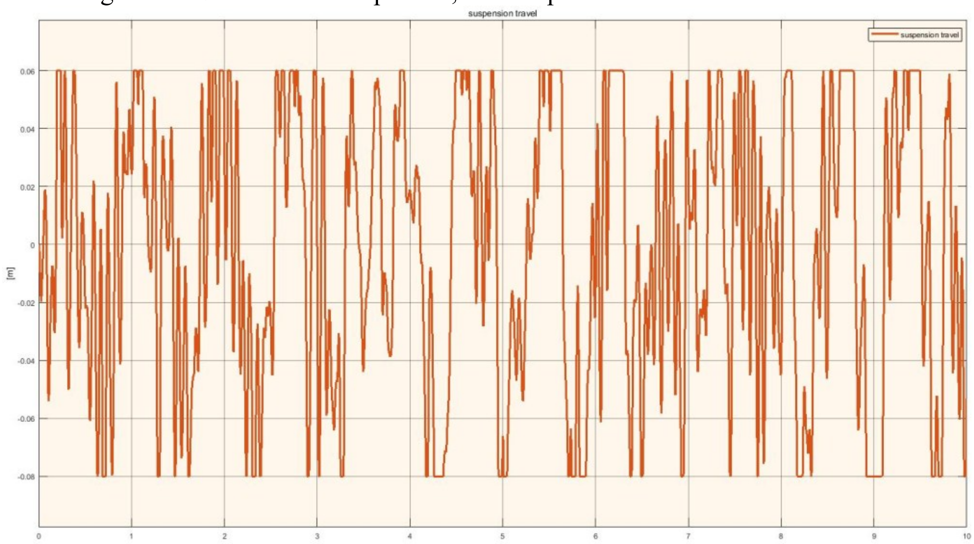

Fig 9.11 - Suspension travel

In the Fig 9.11 is given suspension travel, which is required for the real simulation of the electro-mechanical parts in order to investigate power generator's characteristics.

These control strategies achieve better control performance in the improvement of ride comfort and road holding. However, there are few references to review the state-of-the-art in the modeling and control of intelligent suspension to account for nonlinearity, uncertainties, time delay, and actuator or system fault. Therefore, the thrust of this study is to provide a comprehensive overview of modeling and control from the aspects of nonlinearity, uncertainties, time delay, and actuator or system fault.

10. Electro-mechanical system

10.1. GEARBOX

In order to transform linear wheel movements into rotary we need a power transmission mechanism. In our design the regenerative system works as a lever arm rotary damper, since the wishbone in Macpherson strut can be used as a lever connected to the planetary gear. Planetary gears are always used to reduce or increase rotation speed; it is helpful for boosting motor efficiency and active force. For example, in order to improve the regenerative efficiency, the regenerative component needs more rotations and high rotation speed.

Some companies conducted studies based on electromechanical rotational damping for passenger car and tracked combat vehicle. The passenger vehicle's shock absorber converts the kinetic energy into electrical energy, by using a 48-volt generator. An average recovered power of 100 to 150 watts. 3 watts on the freeway and up to 613 watts on the rough road. This is not enough for AC power, but it can use other accessories and slightly reduce fuel consumption.

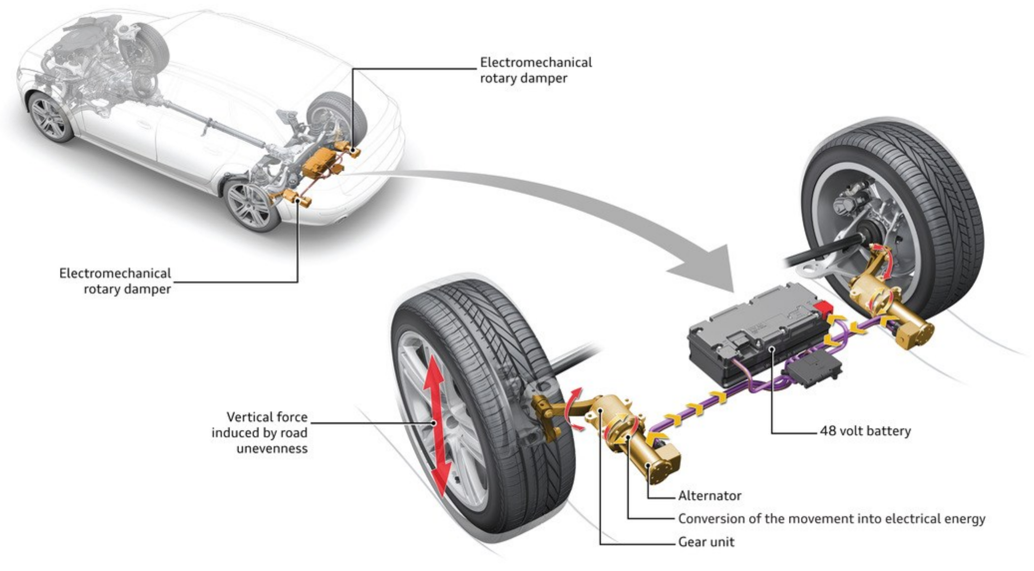

Fig. 10.1 - Electromechanical rotary shock absorber

Meanwhile, the military one gives more perspective because of it's a sufficient active force, compact structure and good safety property that the combat vehicles require. All the elements including motor, planetary gear set, sensors, are integrated in road arm, shown as Fig. 10.2.

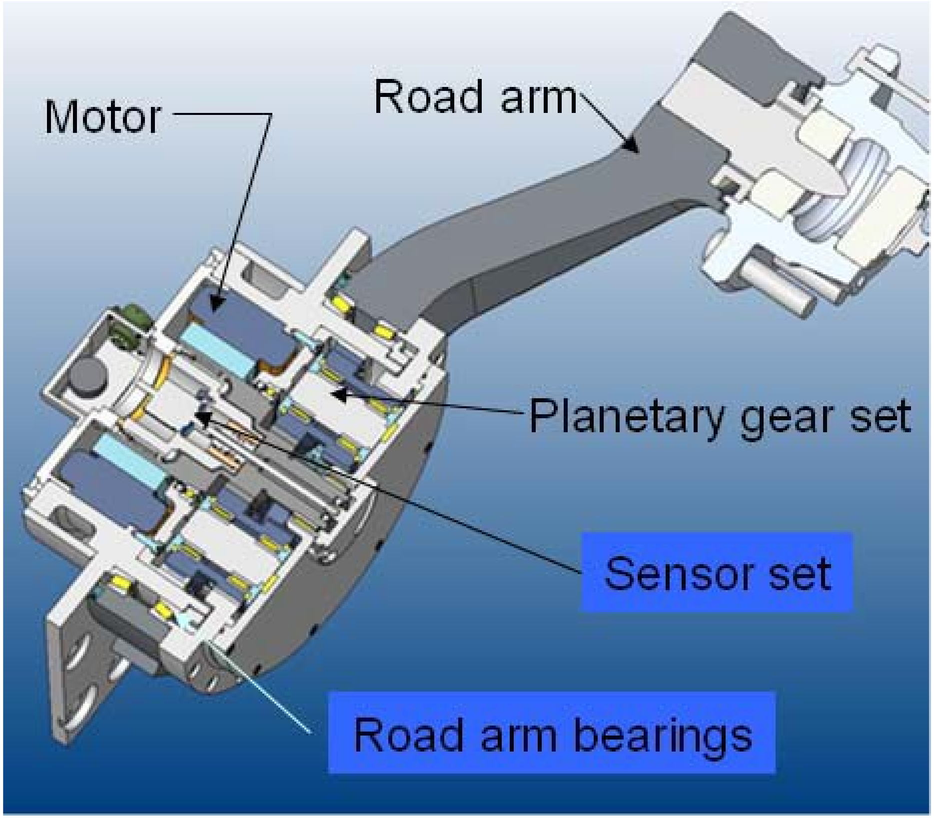

Fig.10.3 - Actuator for combat vehicle suspension ECASS

One of the main objectives of this project is to develop a preliminary prototype of the regenerative suspension system, which can be used to design electrical circuits for regenerative component by using supercaps.

The most important specifications for designing the prototype are the maximum force of 8000 N and the maximum axial speed of 3 m/s. From these specifications, we are able to choose a gearbox for the motor.

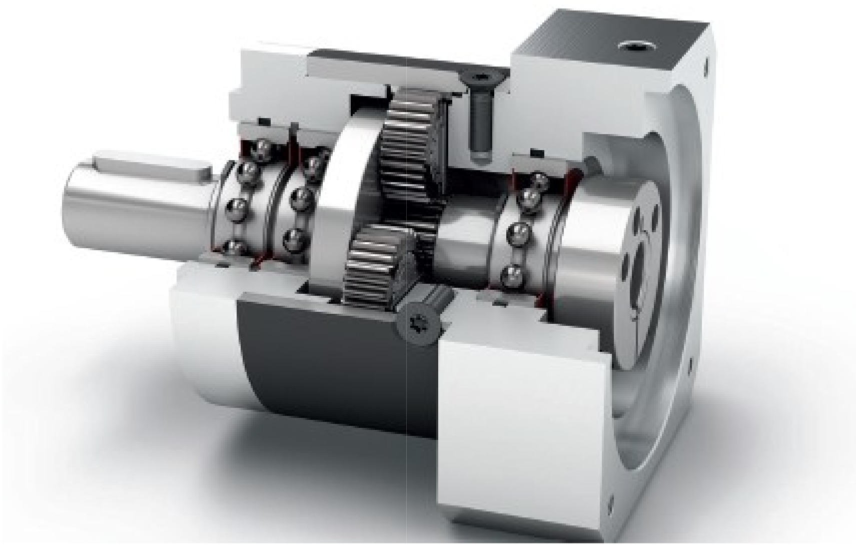

Fig.10.4 - Gearbox

Number of stages	z		3
Reduction ratio	i		256
Efficiency at full load	η	%	92
Min T	T_{min}	^0C	-25
Max T	T_{max}	^0C	90
Standard backlash	j_t	arcmin	<11
Mass moment of inertia	J	$kgcm^2$	1.413 - 2.196
Nominal output torque	T_{2N}	Nm	260
Max. output torque	T_{2max}	Nm	416
Emergency stop torque	T_{2Stop}	Nm	520
Average thermal input speed atT_{2N}	n_{1N}	rpm	3500
Max. mechanical input speed	n_{1Limit}	rpm	6500

Table 10.1 - Technical data of the gearbox

The selected gearbox has almost all parameters that meet our requirements. However, it is not intended for a rotary shock absorber, which prompted me to develop a new type of gearbox integrated with DC motor, since it is not the main objective of the thesis, so the model was educed only with this gearbox.

10.2. Electric motor

The main part of the regenerative suspension system is PM electric motor, which a transducer, motor and power generator, which absorbs portion of energy from road excitation and transforms into electrical energy that can be used later. For this activity, we can use special electric circuit, which represented in the electric part. The relative motion between the magnet and the copper coil produces an eddy current that produces electric energy and results in deceleration. If we connect both electrodes we create a reverse magnetic field, an eddy-current braking system transforms the kinetic energy of the moving body into heat energy that is dissipated through the eddy current in the conductor. However, relative velocities between the magnet and the conductor are required to activate an eddy-current damping system.

Fig.10.5 - PM electric motor

According to Ohm's law and the Lorentz force law, the induced eddy current density on the conducting plate is

$$\vec{J} = \sigma\left(\vec{E} + \vec{v} \times \vec{B}\right) \quad (10.1)$$

J – The current density
σ – The conductivity of the conductor
E – An electric field
v – The velocity of the conducting plate relative to the moving magnet
B – The magnetic field

The drag force produced by electromagnetic interaction can be calculated as

$$\vec{F}_d = \int_V \vec{J} + \vec{B} dV \quad (10.2)$$

The magnitude [13] of the drag force is $\vec{F}_d = \alpha(\sigma\delta B_z^2 lw)v$, where δ is thickness of the conductor, Bz is the flux density in the magnetic pole projection area on the conducting plate, l and w represent the length and width of the pole projection area created by the rectangular permanent magnet and α is constant based on the assumption of an infinite conducting plate.

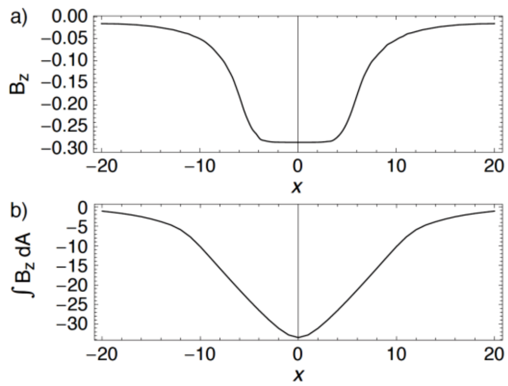

Fig. 10.6: (a) Field strength as a function of distance x through the center of the pole pieces. b) Magnetic flux through a square plate as a function of the position of the plate x.

Notice that the flux depends linearly on some portion of the distance, suggesting that the drag force $\overrightarrow{F_d} = \alpha(\sigma\delta B_z^2 lw)v$, [13] is likely to be valid for moderate amplitudes; however around x = 0 the flux depends quadratically on x, suggesting that is likely to be inaccurate for small amplitudes also the damping effect will be very low. It is very easy to identify damping coefficient as:

$$C_s = \alpha(\sigma\delta B_z^2 lw) \quad (10.3)$$

From this assumption, we can define two major factors of damping effect of the magnetic field; the first is a velocity and second is a distance.

However, we want to use electric motor. There is no single 'breakpoint' below, which PM brushless motors outperform induction motors, but it is in the 1-10 kW range. Above this size, the induction motor improves rapidly, while the cost of magnets works against the PM motor. Below it, the PM motor has better efficiency, torque per ampere, and effective power factor.

Torque/speed characteristic: performance and efficiency

The torque/speed curve of the ideal brushless motor can be derived from the foregoing equations. The combined e.m.f. of two phases in series, the e.m.f. and torque equations can be written in the form

$$E = k\Phi\omega \text{ and } T = k\Phi I \quad (10.4)$$

where

$$k = 4N \text{ and } \Phi = Br\pi l \quad (10.5)$$

k is the 'armature constant' and Φ is the flux.

If the commutation is perfect, and if the converter is supplied from an ideal direct voltage source V, then at any instant the following equation can be written for the d.c. terminal voltage:

$$V = E + RI \quad (10.6)$$

Where R is the sum of two-phase resistances in series and £is the sum of two-phase e.m.f.s in series. Using this equation together with the e.m.f. and torque equations, the torque/speed characteristic can be derived as:

$$\omega = \omega_0\left(1 - \frac{T}{T_0}\right) \quad (10.7)$$

Where the no-load speed is

$$\omega_0 = \frac{V}{k\Phi}\left[\frac{rad}{sec}\right] \quad (10.8)$$

The stall torque is given by

$$T_0 = k\Phi I_0 \quad (10.9)$$

This is torque with the motor stalled at zero speed. The stall current is given by

$$I_0 = \frac{V}{R} \quad (10.10)$$

The relationship between angular speed ω and a constant torque T and constant voltage is linear. By the increasing, the input voltage V increases the offset line. If the phase resistance is small, as it should be in an efficient design, then the characteristic is similar to that of a shunt d.c. motor.

$$\omega = \frac{V}{k\Phi}\left(1 - \frac{T}{R}V\right) \quad (10.11)$$

The speed is essentially controlled by the voltage V, and may be varied by varying the supply voltage. The motor then draws just enough current to drive the torque at this speed. As the load torque is increased, the speed drops, and the drop is directly proportional to the phase resistance and the torque.

The Permanent Magnet DC Generator can be considered as a separately excited DC brushed motor with a constant magnetic flux. In fact, nearly all permanent magnet direct current (PMDC) brushed motors can be used as a permanent magnet PMDC generator, but as they are not really designed to be generators.

These DC machines consist of a stator having rare earth permanent magnets such as Neodymium or Samarium Cobalt to produce a very strong stator field flux instead of wound coils and a commutator connected through brushes to a wound armature as before. When used as permanent magnet DC generators, PMDC motors generally have to be driven a lot faster than their rated motor speed to produce anything near to their rated motor voltage so high voltage, low rpm DC machines make better DC generators. The main advantage over other types of DC generator is that the permanent magnet DC generator responds to changes very quickly because their strong stator field is always there and constant it can be used as a sensor.

The overall efficiency of small permanent magnet DC generators is determined by several independent factors, efficiencies range from 75% to 95%, with a mean of about 85%. There are can be found many DC motors that are suitable for our rotary shock absorber. For example, a motor below has very good characteristics for the application.

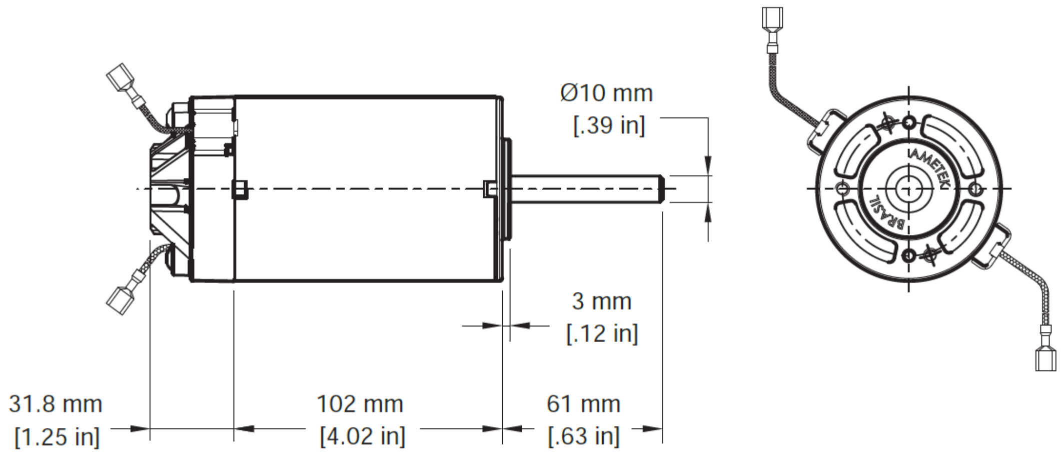

Fig.10.7 – Geometric parameters of the PM electric motor

Description	
Length	70 mm
Voltage	12-36 VDC
Type	PM, 2-poles
Speed	500-6200 rpm
Power	600W (0.8 hp)

Table 10.2 - Technical data of the electric motor

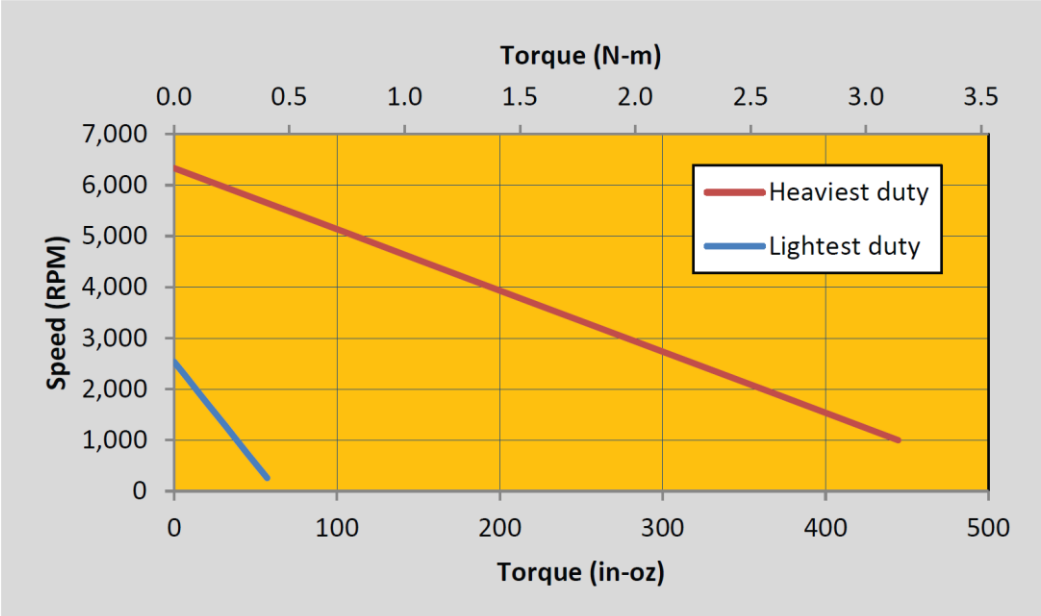

Fig.10.8 – PM electric motor capabilities by speed and torque

The figure 10.4 gives us information about trade-offs between speed and torque. For example, for the speed 3000 rpm the electric motor works with torque 1.8Nm. The output torque after gearbox is equal to 460 Nm and transversal force is higher that is 1500N. Maximum limit is about 1000Nm, which is extremely high and we should prevent gearbox from mechanical breakdown, for this, the electric current must be limited.

11. A test bench and the output voltage of the PM electric motor

The test was done in order to study DC generator's power characteristics especially, output voltage of the PM electric motor. The main aim of the simulation is to build electric circuit, which can absorb the energy from the random road excitation. Two-coupled motor were used and mat lab code with sinusoidal approximation of the random road and which was connected to Arduino Uno by using audio output, and whole system is based on open loop (can be closed loop by using audio in).

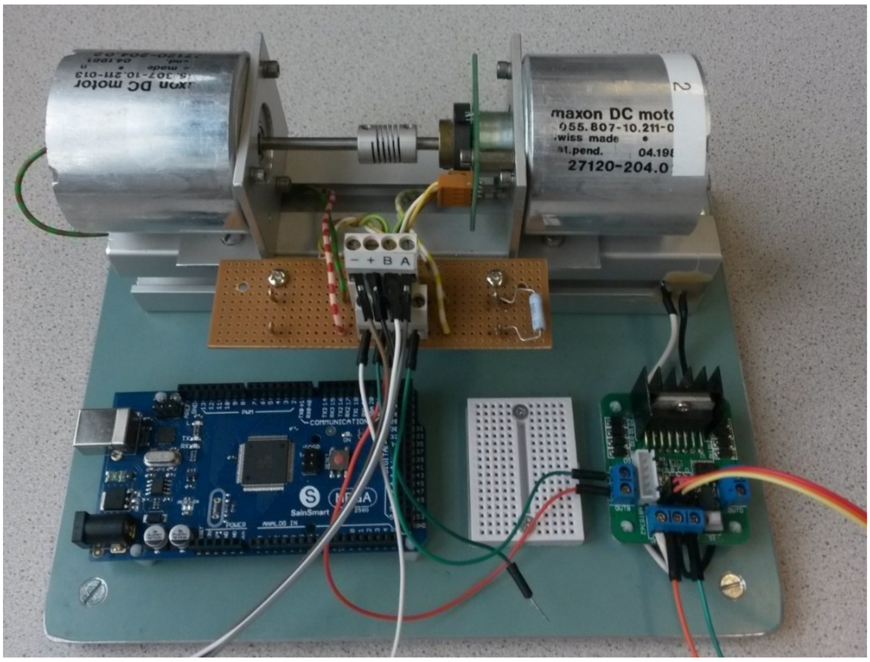

Fig. 11.1. DC electric motors (left generator, right motor)

Matlab code consists two parts – a signal generator, which is random road excitation and a signal transfer, which is input for the Arduino.

```
% Sinusoidal Approximation
clear all
close all
clc
%% Constants
class=[1 4 16 64 256 512 1024]*1e-6; % degree of roughness of road
profiles m^2/rad/m
om0=1; % ref wave number rad/m
k=2; % waveness
i=2; % road classification
%% Approximated constants
V=17; % velocity m/s
L=170; % wavelength V/f
N=300;
%%
asf=.05; % angular spantial frequincy 2*pi/L rad/m
% w=asf*V;
%% PSD ISO 8608
om=logspace(-1,2,N)';
PSD=class(i)*(om/om0).^-k;
%asf=om(2)-om(1);
w=asf*V;
phi=2*pi.*rand(N,1); % random variable N>100000000
time=linspace(0,L/V,N);
step=time(2)-time(1);
% figure(1);
% loglog(om,PSD);
m=1;
zr=zeros(size(time));
for tj=time
    Zk=0;
    for n=1:N;
        A=sqrt(PSD(n)*asf/pi);
        Z=A*sin(n*w*tj-phi(n));
```

```
        Zk=Zk+Z;
    end
    zr(m)=Zk;
    m=m+1;
end
figure(2);
plot(10*time,zr)
xlabel('time');
ylabel('s[m]');
for i=1:299
        vr(i)=zr(i+1)-zr(i)/.03;

        vr(i)=2000*vr(i)+2000;
end
plot(vr*.2)
 % signal transferring
for i=1:length(vr)
tic
Fs = 44100;
t = [0:1/Fs:0.3-1/Fs]; %1 second, length 44100
freq1 =vr(i);
vel1=freq1*0.3% Hz
f1 = sin(2*pi*freq1*t);
sound(f1,Fs)
toc;
pause(1-toc)
toc
 end
```

Signal transferring was released by using the functions below:

*f1 = sin(2*pi*freq1*t);*

sound(f1,Fs);

Output signal from a computer is generated by sound card and it has specific amount of peaks equals to the given value of the 0.3*freq1.

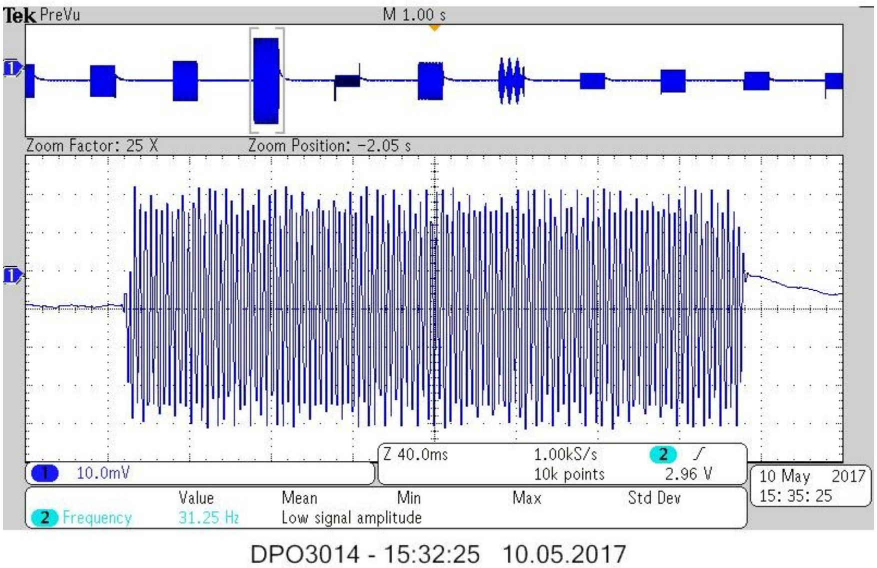

Fig. 11.2. Output signal from the sound card.

Every signal has unique frequencies, it can transfer desired information in 40 msec, amount of peaks are input velocity and direction. Maximum value is 800.

```
unsigned long times=0;
unsigned long t=0;
int k=0;
int i=1;
int key=1;

int enA = 9;
int in1 = 8;
int in2 = 7;
int audi = A3;
int MotorSpeed1 = 0;
int refcor = 400;
void setup()
{
  Serial.begin(9600);
 // motor pins
  pinMode(enA, OUTPUT);
  pinMode(in1, OUTPUT);
  pinMode(in2, OUTPUT);
  // intializing
  digitalWrite(enA, LOW);
  digitalWrite(in1, HIGH);
  digitalWrite(in2, LOW);
}
void loop() {
  times=millis();
k=0;
t=0;
for (unsigned long t=0; t<times+500;){
  refcor = analogRead(audi);
  if (refcor>10&&i==1)
  {
    k++;
    i=0;
  }
    if (refcor==0)
  {
    i=1;
  }
    t=millis();
}
  Serial.println("vel");
  Serial.println(k);
 refcor=k;

  if (refcor < 400 )
  {
    // This is CW
```

```
   // Set Motor A up
  digitalWrite(in1, LOW);
  digitalWrite(in2, HIGH);
   refcor = 400-refcor; // This produces a negative number
   MotorSpeed1 = map(refcor, 0, 400, 0, 255);
}
else if (refcor > 400)
{ // CCW
     // Set Motor A down
  digitalWrite(in1, HIGH);
  digitalWrite(in2, LOW);
  //Determine Motor Speeds
   MotorSpeed1 = map(refcor, 400, 800, 0, 255);
}
else
{
  // This is Stopped
   MotorSpeed1 = 0;
}
if (MotorSpeed1 < 8)MotorSpeed1 = 0;
   analogWrite(enA, MotorSpeed1);
}
```

Then by using oscilloscope, we can read output voltage from DC generator. From the result, we are able to have an idea how the voltage changes due to random excitation. The result is not exact output, which can be expected from random road excitation. On the other hand, we are able to observe voltage change for different speeds and also voltage saturation level and time, which corresponds to angular velocity of the rotor.

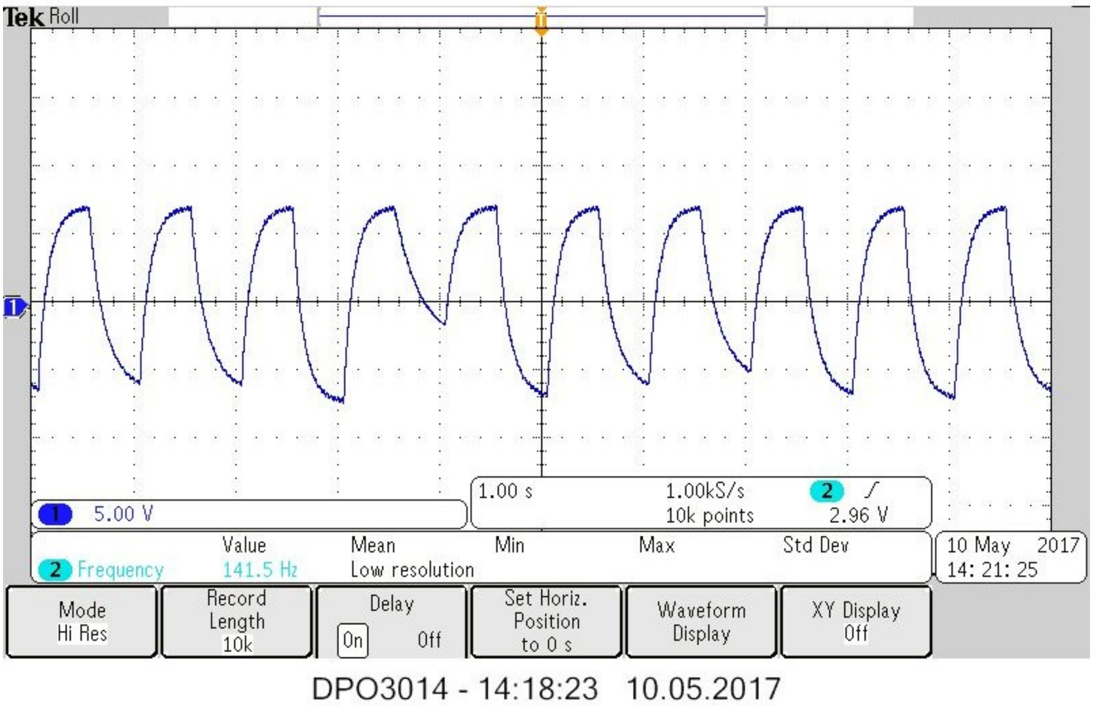

Fig. 11.3. Output voltage from the generator.

The voltage output has almost same behavior as a vibration of the system. From the simulation, we have low power but it can be solved by using gear set. The gear set increases ratio, which is proportional to the velocity.

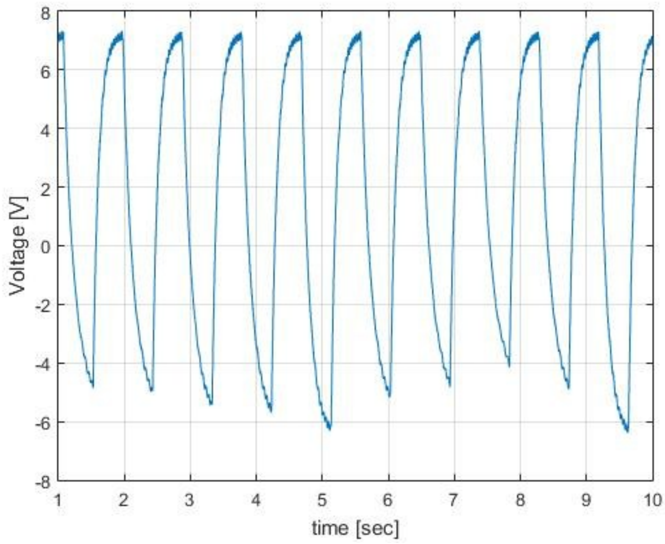

Fig. 11.4. Output voltage from the generator collected in the Matlab code.

Theoretically, it is possible and it will work. However, in order to achieve a good result we need very high ratio gear set with high torque and fatigue limit and it will cost a lot. Alternatively, we can use high torque motor but it will be heavy and expensive, from the other side the voltage output from the DC generator can be used as transducer signal.

12. Electric circuit

The electric circuit consists four parts a rectifier, mosfets (N and P type), one buffer capacitor and a set of capacitors as a power bank. The rectifier converts an alternating current into a direct one by allowing a current to flow through it in one direction only. It is mandatory for our capacitors. The buffer capacitor absorbs instant power from the rectifier when the voltage of the capacitor reaches required level of the threshold voltage of the mosfets, which connects buffer capacitor to other capacitors then the set of capacitors takes the energy from the buffer capacitor. From the simulation it obvious to find the drawback of the circuit, which is high power consumption of mosfets.

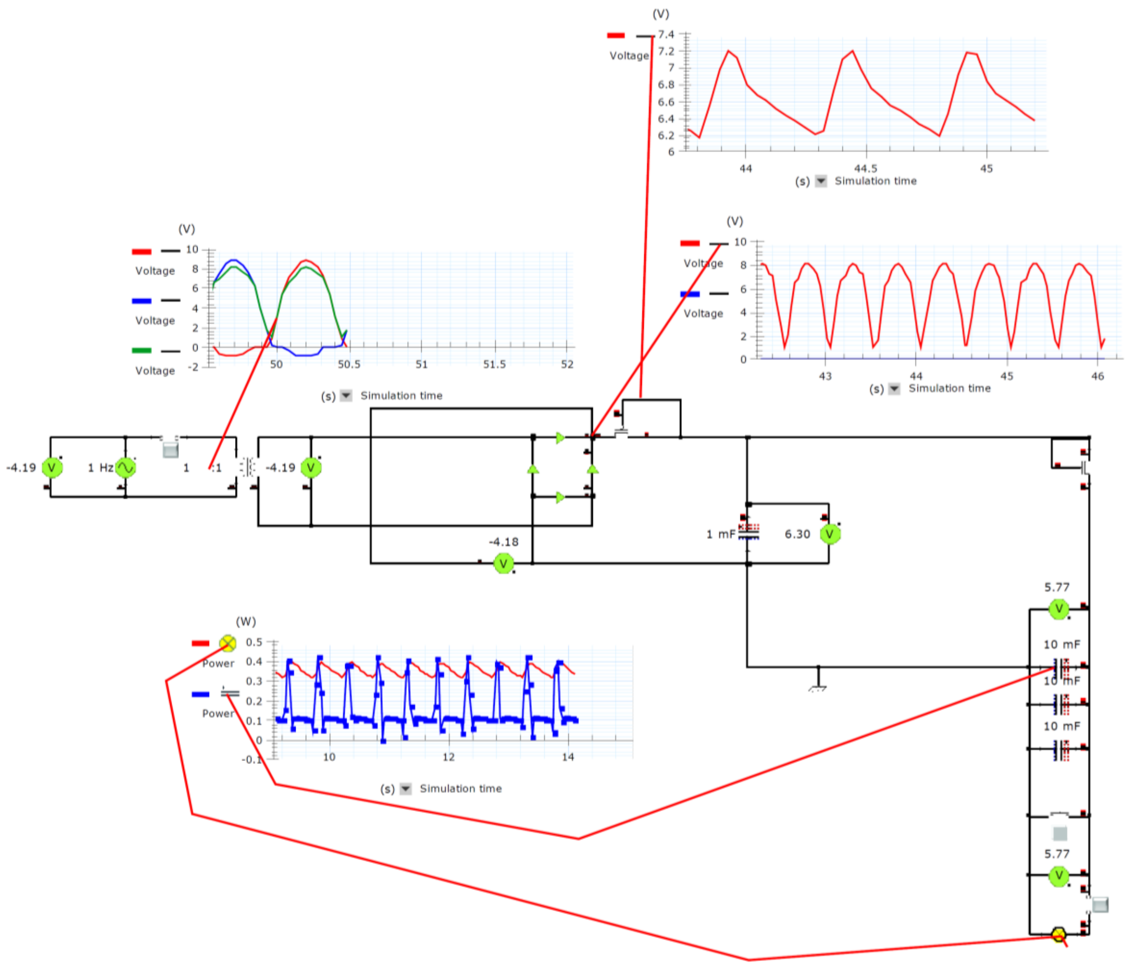

Fig. 12.1 Simulation of the electric circuit

The research showed that theoretically, we are able to collect some energy from the road excitation but the power from the energy generating system is very low. In order to improve output power we must use a gear set with high ratio and high fatigue and toque limit in order to handle more torque and to increase velocity, or high torque generator would be suitable but price of those elements are high and the weight of the system will be very heavy. Even if we want to use the power from road excitation, the electric system, which will use electricity to collect the power by using capacitors, has one drawback. The circuit self-controlled by using (N and P type) Mosfets. Mosfets have high response on the contrary; they need some power to control the circuit. It has good voltage stability, but it is quite low about 6 Volts. However, it allows using supercapacitors that has even lower input voltage limit.

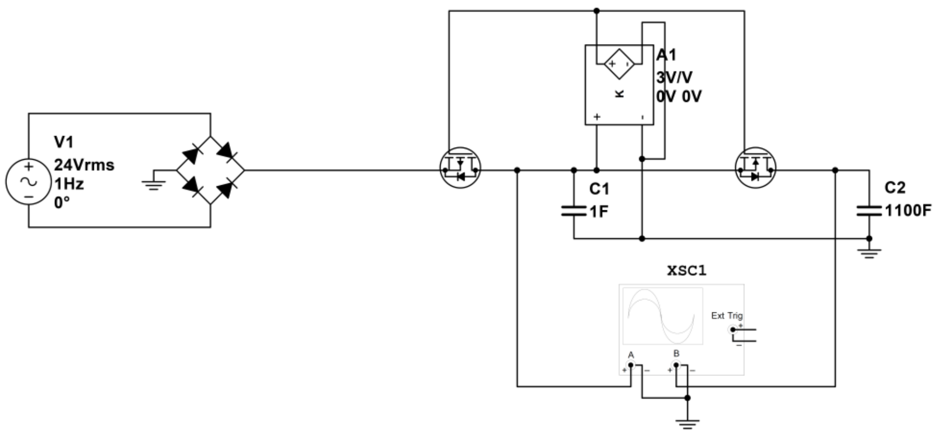

Fig. 12.2 Electric circuit with voltage gain.

Figure 12.2 gives us a circuit that is more realistic or non-ideal circuit, in this circuit the voltage gain block was used in order to amplify threshold voltage of mosfets. From working point, it is same like previous circuit and it has same drawbacks. For example during switching on process of mosfets, buffer capacitor is not able to absorb regenerative voltage and we should choose a capacitor with higher capacitance, which absorbs more energy for longer period. However, it changes circuit characteristics. That is why; it can be used only cyclic voltage input with short period.

The performance of the circuit has been improved with the help of the controller. Before using the controller input signal from the generator, it is necessary to study to create a code that is capable of handling issues related to voltage control. The idea is simple; when the regenerative input voltage reaches a peak and then goes down, the mosfets, regardless of the buffer capacitor voltage, will turn on and release all the power from the buffer capacitor to the power bank.

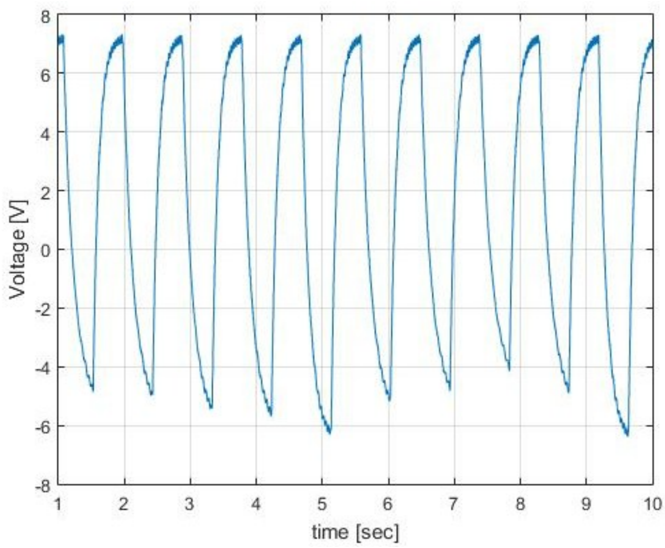

Fig. 12.3. Output voltage from the generator collected in the Matlab code.

` The circuit with a controller has own benefits. Because we can monitor any, part of the circuit and use input signal for the code. This allows us to manipulate mechanical and electrical systems with an intelligent control strategy.

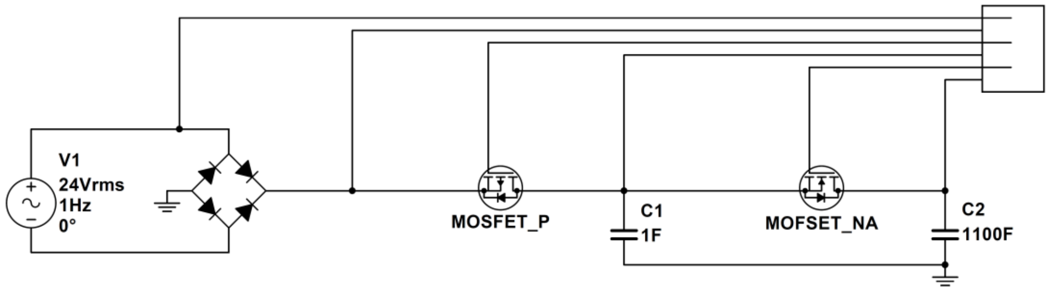

Fig. 12.4 Circuit with controller

However, the vehicle shock absorber with semi active or especially active systems does not always absorb the energy with same quality. During compression, the damper should not receive a lot of energy, but in period of extension, it has to receive more the potential energy from suspension spring.

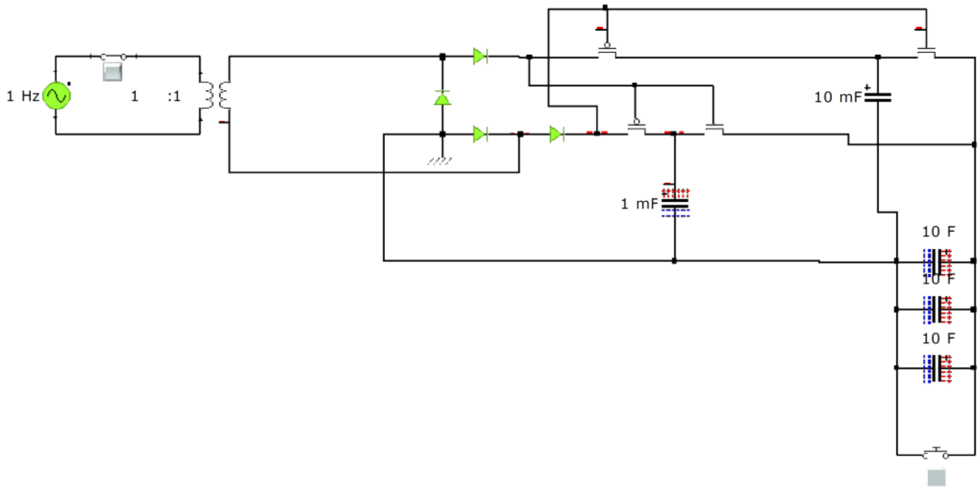

Fig. 12.5 Circuit with two buffer capacitors

Not all circuits above have a good performance for this activity. Because the voltage of the buffer capacitor must be different for compression and extension. The voltage can be controlled by changing capacitance of the buffer capacitor or increasing threshold voltage of the mosfets. In Fig.12.5, one can find two different capacitors. A capacitor with higher capacitance can be used during extension another one during compression. Fortunately, we do not need extra sensors in order to identify directions of the wheel travel, because PM electric motor itself can be used as a transducer.

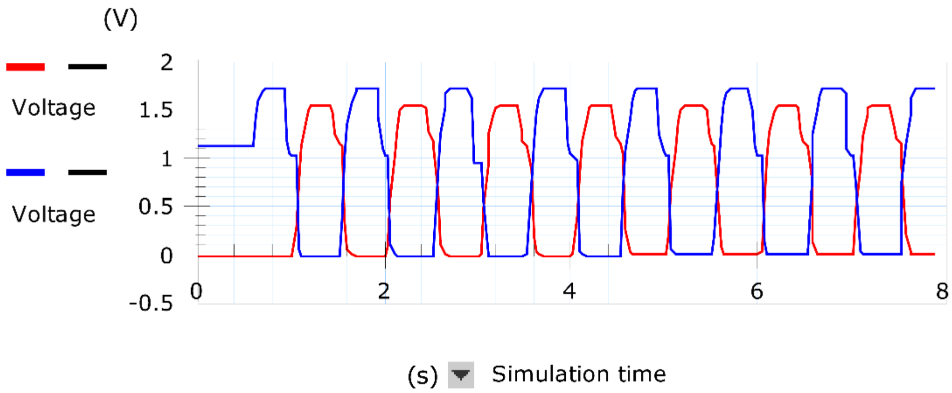

Fig. 12.6 Voltages of the buffer capacitors

As I mentioned, the voltage of the capacitors is different, and different voltages allow controlling the mechanical system better than electric circuit with one buffer capacitor. The graph in fig 12.6 shows us two different voltages, one with a higher peak is a capacitor with a higher capacitance. The way of changing voltages shows how the electric circuit works. Since control logic of the circuit based on mosfets when one of the capacitors starts to absorb the second, begins to release energy by isolating the buffer capacitor from the rectifier.

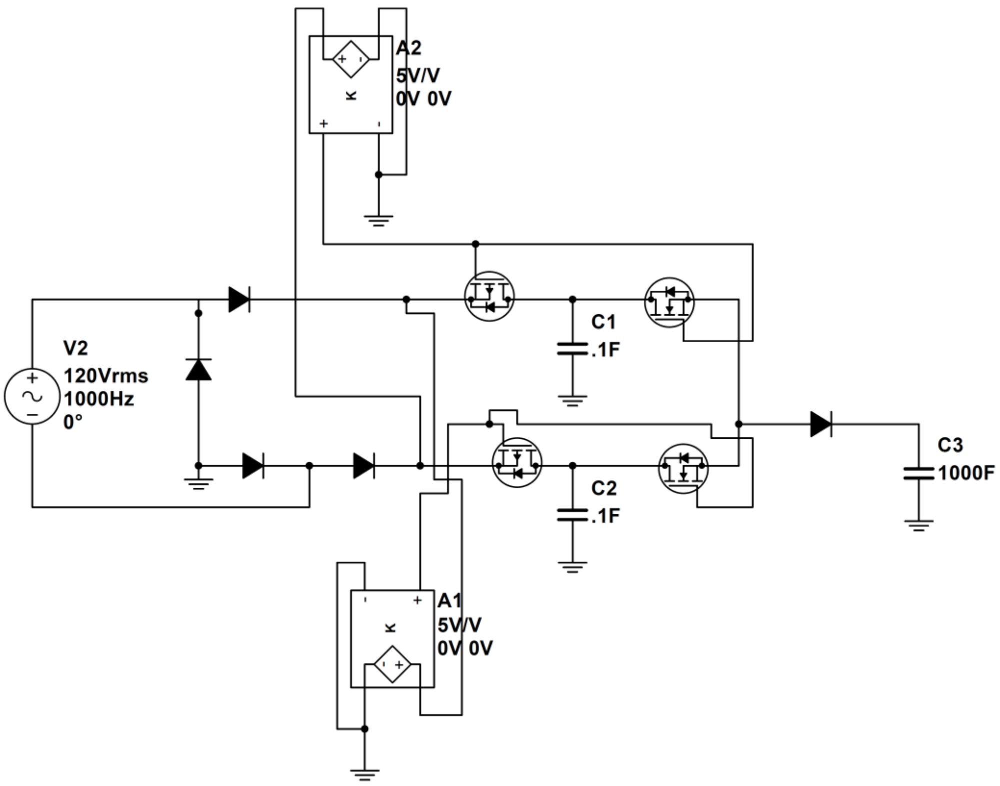

Fig. 12.7-Advanced circuit with two capacitors

Fig. 12.7 shows a circuit similar to that in fig 12.5, but more advanced. In general, the circuit with capacitor is very useful for regenerative systems such as regenerative suspension, regenerative braking, etc. It is safer and it has low power losses with good performance characteristics, which opens up great roads with many opportunities.

13. Alternative energy harvesting system

In this section of thesis, an alternative regenerative system was studied. The basic idea of this system is to use rectangular type strip springs and new emerging ferroelectric ceramics. In general, it can be considered as a composite material.

For the strip spring a steel 50CrV4 (EN 10277) was chosen, this steel has a very high ultimate tensile stress and yielding stress. However, before designing the torsion bar, it is necessary to calculate some parameters. The length of the torsion bar is 1.2 m and the moment acting to the spring is 3200 Nm with angle of twist, which is 12 degrees or the angle of twist per unit length is 0.20944 rad/m. G – shear modulus of elasticity is 80 GPa and tensile modulus of elasticity E is 210 GPa.

Tensile Yield Stress

$$\sigma_Y = 0.85\ \sigma_U = 1105MPa \qquad (13.1)$$

Torsional Yield Stress

$$\tau_Y = 0.6\sigma_Y = 0.6 * 1105MPa = 663MPa \qquad (13.2)$$

Tensile Working Stress

$$\sigma_W = \sigma_B = \frac{\sigma_Y}{S.F.} = \frac{1105MPa}{1.2} = 921MPa \qquad (13.3)$$

Maximum Combined Shearing Stress

$$\tau_M = \frac{\tau_Y}{S.F.} = 368MPa \qquad (13.4)$$

Compressive stress at mid-point of width "b",

$$\sigma_A = -\frac{\sigma_B}{2} = -460MPa \qquad (13.5)$$

Maximum shearing stress at mid-point of width "b",

$$\tau_A{}^2 = \tau_M{}^2 - \left(\frac{\sigma_A}{2}\right)^2 = 8.27E16 \qquad (13.6)$$

$$\tau_A = 288MPa \qquad (13.7)$$

Thickness of rectangular strip

$$c = \frac{\tau_A}{G\theta} = 0.017m \qquad (13.8)$$

Total Twisting Torque per Strip Spring

$$T_n = \frac{1}{3} bc^3 G\theta + \frac{1}{360} Ecb^5\theta^3 = 1129\ [Nm] \qquad (13.9)$$

The total torque is the sum of all single strip springs. Neglecting inter-spring friction between strip springs of equal width and thickness [18].

Number of Strip Springs Required Per Pack

$$n = \frac{T}{T_n} = 3 \qquad (13.10)$$

Total Height of Laminated Spring Pack

$$H = nc = 0.051 \qquad (13.11)$$

Maximum principal tensile stress,

$$\sigma_1 = \frac{\sigma_A}{2} + \sqrt{\left(\frac{\sigma_A}{2}\right)^2 + \tau_A^2} = 138MPa \qquad (13.12)$$

Maximum principal compressive stress

$$\sigma_2 = \frac{\sigma_A}{2} - \sqrt{\left(\frac{\sigma_A}{2}\right)^2 + \tau_A^2} = -599MPa \qquad (13.13)$$

Maximum combined shearing stress

$$\tau_M = \sqrt{\left(\frac{\sigma_A}{2}\right)^2 + \tau_A^2} = 368MPa \qquad (13.14)$$

At point "B", the longitudinal stress "a" is maximum tensile.

and the shearing stress "T " is zero,

Maximum principal tensile stress,

$$\sigma_1 = \sigma_B = 921MPa \qquad (13.15)$$

Maximum principal compressive stress

$$\sigma_2 = 0 \qquad (13.16)$$

Maximum combined shearing stress

$$\tau_M = \frac{\sigma_B}{2} \qquad (13.17)$$

Safety factor

$$S.F. = \frac{\tau_Y}{\tau_M} = 1.25 \qquad (13.18)$$

The safety factor is higher than one, which allows to use size parameters for the next studies. The thickness of the strip spring is bigger than expected value; anyway, sizes will be changed after the FEM simulation.

When the parallel torsional springs are twisted, the distance between them decreases and creates a huge perpendicular stress on the axis of rotation. If another hard material has been installed between, the strip springs. This will increase the spring stiffness, since there will be reaction forces between the strip springs. When the torque reaches 3200 Nm, the average compressive stress between the plates is 205MPa. Moreover, there will be only compressive stresses that means no fatigue analysis related to the material between the plates is required and it allows to use ceramic materials such as piezoelectric, ferroelectric crystals. These materials have poor mechanical characteristics, but their piezoelectric properties capable of producing hundreds of kilovolts and gigawatt-peak power microwave radiation. The levels of voltage and energy are sufficient to provide energy to the electrorheological shock absorber.

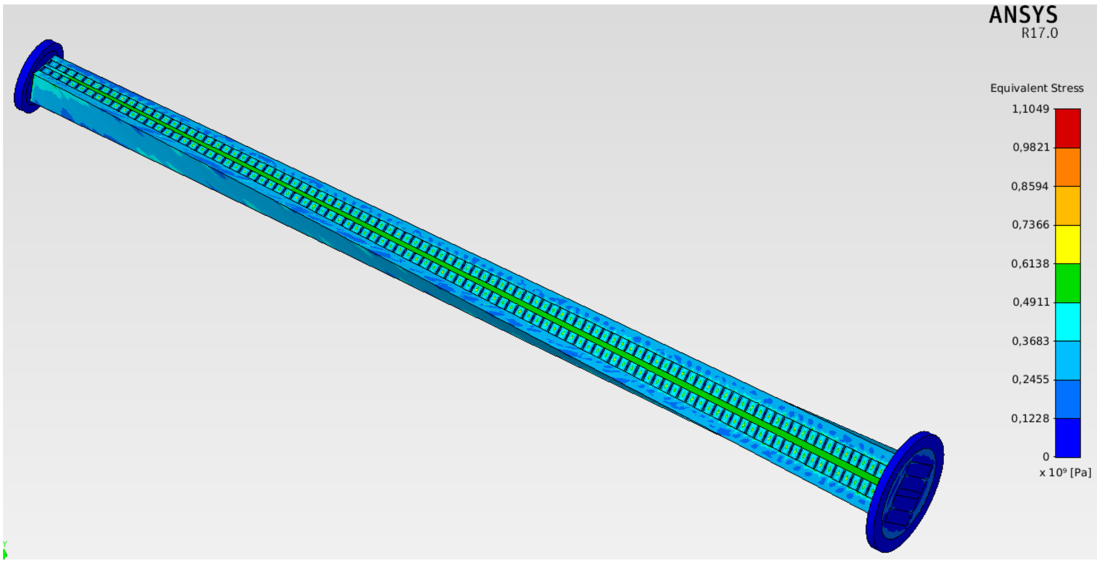

Fig. 13.1. Stress analysis of the torsion bar.

Figure 13.1 illustrates the stress distribution along the bar. The maximum stress is about 600 MPa and it is a local stress not general, because with proper design of the contact surfaces, maximum local stress can be reduced. However, stress distribution is not same for everywhere at the boundaries it is lower than the middle part and the difference is about 10MPa.

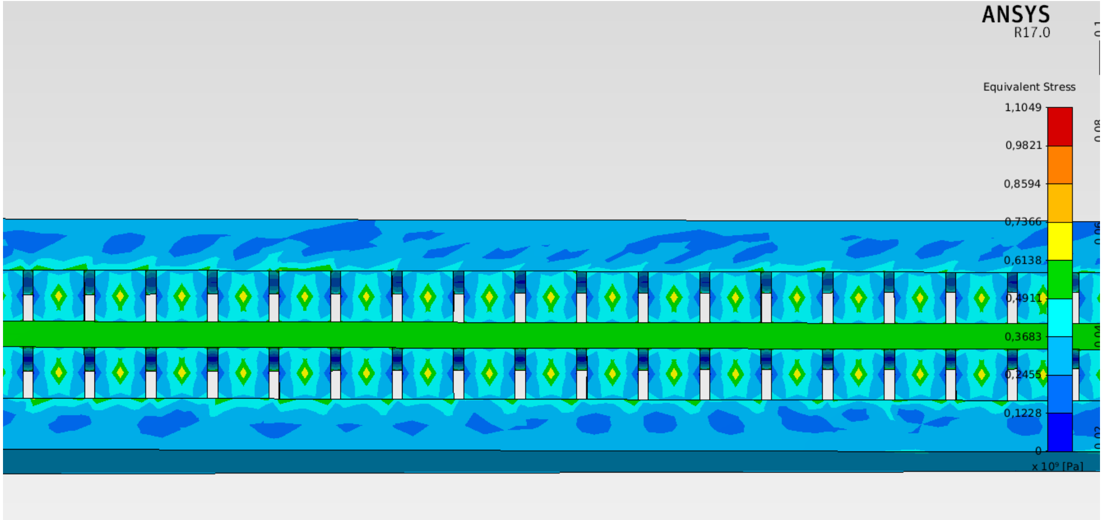

Fig. 13.2. Stress distribution in PIN-PMN-PT ferroelectric ceramics.

Afterwards, the piezoelectric material with size 10mm x 10mm x 40mm was studied by the finite element method and the material was treated with pressure that was obtained from previous simulation. It is about 2.05e8 Pa or 205 MPa. The electro-mechanical properties of the ferroelectric material PIN-PMN-PT that was used in the simulation can be found in table 13.1.

Property (manufacturer data*)	PIN-PMN-PT	PZT 52/48	PZT 95/5
Density (103 kg/m3)	8.1	7.5	7.9
Curie point (°C)	167	320	230
Dielectric constant at 1 kHz (poled)	1180	1300	295
Dielectric constant at 1 kHz (depoled)	940	1140	250
Piezoelectric constant d33 (10−12 m/V)	1800	295	68
Elastic constant s11E (10−12 m2/N)	16.4	12.8	7.7
Remnant polarization (C/m2)	0.48	0.29	0.32
Experimental result			
Stress-induced charge density, ω (C/m2)	0.48 ± 0.02	0.15 ± 0.02	0.32 ± 0.02
Stress-induced voltage (kV)	40.4 ± 0.18	17.8 ± 0.16	40.1 ± 0.19
Stress-induced electric field (MV/m)	8.08 ± 0.36	3.56 ± 0.32	8.02 ± 0.38
Energy density in the high voltage mode, W (MJ/m3)	0.305 ± 0.034	0.076 ± 0.006	0.068 ± 0.004

Table. 13.1. Physical properties of the ferroelectric materials.

Some researchers showed that an increase of the stress up to a few tens of megapascals resulted in harvesting of 0.75 kJ/m3 energy density from PIN-PMN-PT crystals. For example the voltage and energy produced by PIN-PMN-PT: a single crystal with thickness 6 cm and total volume 70 cm3 is capable of producing a 400 kV microsecond pulse with total energy 15 joules.

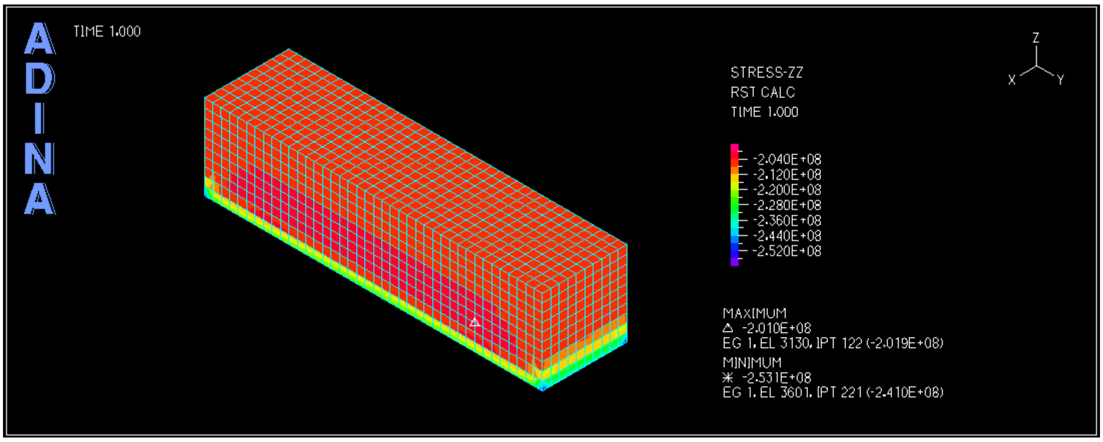

Fig. 13.3. Stress analysis of the ferroelectric ceramic PIN-PMN-PT.

The voltage distribution along the Y-axis has a linear character and voltage difference between two sides is about 26 Kilovolts. However, the electric field along the Y-axis shows a non-linear character accept at the ends of the Y-axis.

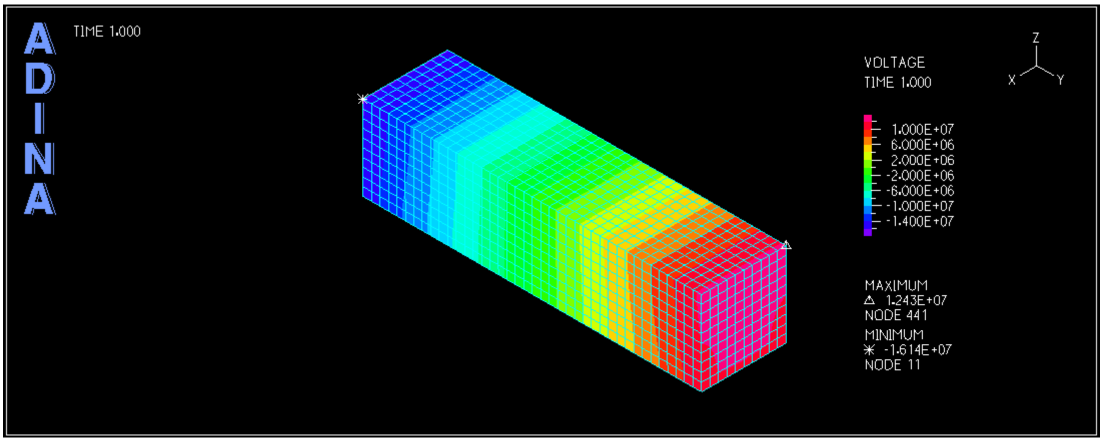

Fig. 13.4. Voltage analysis of the ferroelectric ceramic.

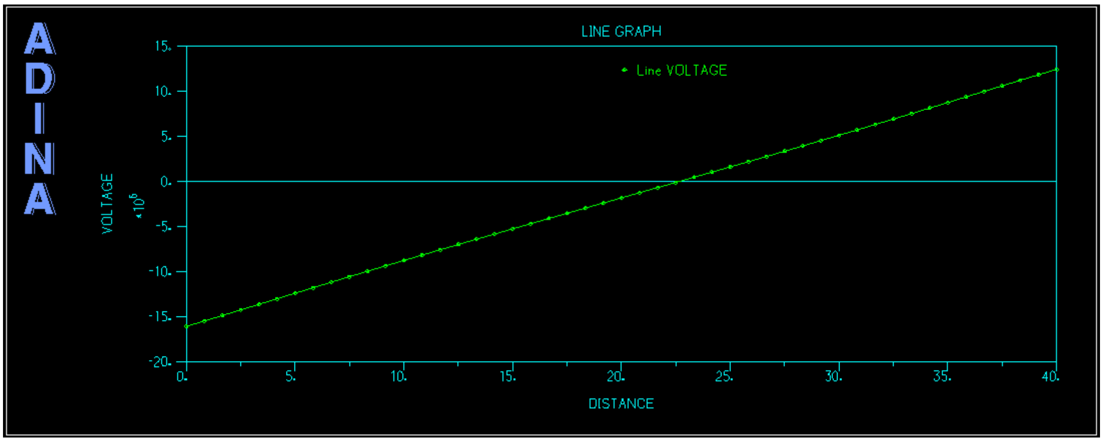

Fig. 13.5. Voltage distribution along the y-axis is linear.

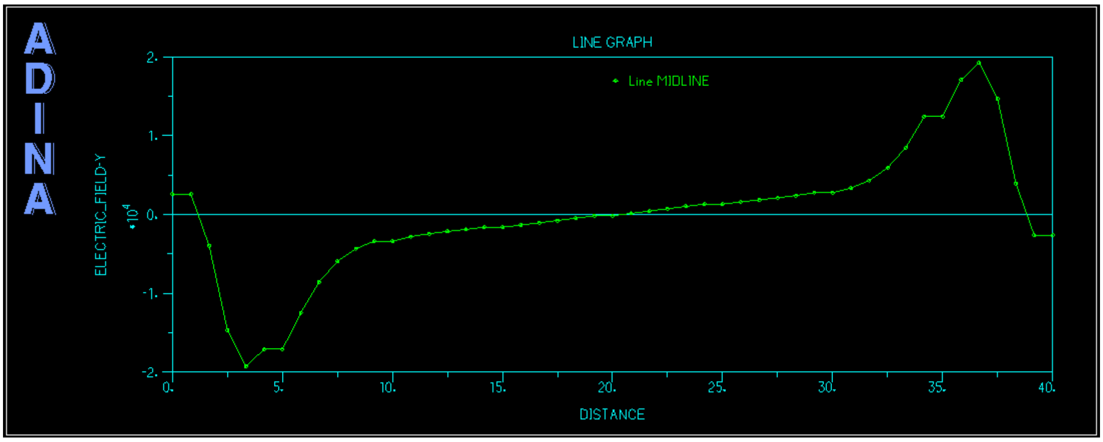

Fig. 13.6. The electric field of the ferroelectric ceramic along the y-axis.

The estimated energy that can be harvested from the microsecond pulse is about 200 Joules. The most interesting part is the stiffness of the torsional spring, which can be tuned during vibration. It demonstrates that new materials can improve old conventional mechanisms . Proper design, nanotechnology and with innovative ideas can provide alternative suspension systems, where the material itself can work as a spring and a shock absorber.

14. Conclusion

If we use every emerging technology and new materials in our life, it will change the world. However, each innovation has its time, place and cost. When these three factors coincide and customers demand the new technology. Manufactures start to produce. Otherwise, despite the attractiveness of innovations, they will remain on paper. Nevertheless, from the manager to the chief engineer, one must beware of ignoring new technologies that initially do not meet the needs of their main customers.

In this thesis a new disruptive innovation has been introduced, which will subsequently be changed to sustainable production, if new materials are available to create high performance mechanisms.

From the technological point of view the electrorheological shock absorber is able to control vibration with high performance, but its power consumption and some technical issues related to the material properties such as dielectric break-down, water or air inside of the fluid and the cost of the ER-fluid, will challenge the improvement electrorheological materials. However, the proper design of the shock absorber can effectively improve control force, in our case the control force of the damper is 10kN or it can be even higher, since it was calculated by the finite element method.

The regenerative part of the suspension system was designed to check electromechanical parameters of the system, and the simulation results allow the creation of power circuits. These circuits illustrate the basic principles of the energy regeneration and control process. In addition, circuits with two buffer capacitors showed high performance.

In the mechanism above, one can find a lot of details and complexity suspension system is higher than conventional shock absorber. Anyway the performance, comfort and stability make the semi-active damper more attractive.

In the last part of the research a new alternative energy regenerative system was designed. The main advantage is the size of the torsion bar, adjustable stiffness and produced voltages that are enough high to apply to the ER shock absorber.

The tendency of the scientific researches shows that in the future it will be possible to create composite materials with a special nano-structure that the material itself can work as a spring and a shock absorber one structure.

References

[1] Zhang Jin-qiu, Peng Zhi-zhao*, Zhang Lei, Zhang Yu, "A Review on Energy-Regenerative Suspension Systems for Vehicles", Proceedings of the World Congress on Engineering 2013 Vol III, WCE 2013, July 3 - 5, 2013, London, U.K.
[2] Claudiu Valentin Suciu, Tsubasa Tobiishi, and Ryouta Mouri, "Modeling and Simulation of a Vehicle Suspension with Variable Damping versus the Excitation Frequency", Fukuoka Institute of Technology, Fukuoka, Japan.
[3] ISO 2631-1, "Mechanical vibration and shock – evaluation of human exposure to whole-body vibration" 1997-06-01.
[4] Feng Tyan, Yu-Fen Hong, Shun-Hsu Tu, Wes S. Jeng, Generation of Random Road Profiles", Taiwan

[5] A. Hac,"SUSPENSION OPTIMIZATION OF A 2-DOF VEHICLE MODEL USING A STOCHASTIC OPTIMAL CONTROL TECHNIQUE", Institute of Mechanical Engineering, Technical University of Warsaw, ul. Narbutta 84, 02-524 Warszawa, Poland (1985).
[6] A.A. Silaev, " Spectral theory of the car suspension systems", Mashinostroenie, Moskow, 1972.
[7] M. Agostinacchio & D. Ciampa & S. Olita, "The vibrations induced by surface irregularities in road pavements – a Matlab® approach", SpringerLink.com
[8] L. Meirovitch, "Fundamentals of vibrations", Virginia Polytechnic Institute and State University. 2001
[9] Honghai Liu, Huijun Gao and Ping Li, "Handbook of Vehicle Suspension Control Systems", The Institution of Engineering and Technology, London, UK 2014.
[10] T.P.J. van der Sande, B.L.J. Gysen, I.J.M. Besselink, J.J.H. Paulides, E.A. Lomonova, H. Nijmeijer, "Robust control of an electromagnetic active suspension system: Simulations and measurements", ELSEVIER. 2013
[11] Fernando D. Goncalves and Mehdi Ahmadian, "A hybrid control policy for semi-active vehicle suspensions" Advanced Vehicle Dynamics Laboratory, Department of Mechanical Engineering, Virginia Tech, Blacksburg, VA 24061, USA
[12] Der-Ming Ma, Jaw-Kuen Shiau, "THE DESIGN OF EDDY-CURRENT MAGNET BRAKES", Transactions of the Canadian Society for Mechanical Engineering, Vol. 35, No. 1, 2011
[13] Catherine Weigel, Jeremy Wachter, Paul Wagoner, and Timothy J. Atherton, "Predicting the Influence of Plate Geometry on the Eddy Current Pendulum", Tufts University, Medford, USA
[14] "Electrorheological (ER) Fluids", U.S. Departament of Energy, Office of Energy Research, Office of Program Analysis, Washington, May 1993.
[15] F. Gordaninejad O.A. Graeve, A. Fuchs, D. York, "Electrorheological Fluids and Magnetorheological Suspensions", University of Nevada, Reno 2007.
[16] K. J. BATHE, "NONLINEAR FINITE ELEMENT ANALYSIS AND ADINA", Department of Mechanical Engineering, Massachusetts Institute of Technology, Cambridge, MA 02139, U.S.A. 1983
[17] Faramarz Gordaninejad, Olivia A. Graeve, Alan Fuchs, David York, "Electrorheological Fluids and Magnetorheological Suspensions" University of Nevada, USA
[18] Joseph A. Gentiluomo "DESIGN OF LAMINATED TORSION BAR SPRINGS" Procurement Directorate Watervliet Arsenal Watervliet, N.Y. 1980